QUANTUM DOT MULTI-SECTION LIGHT EMITTERS

BY

YONGCHUN XIN

B.S., Physics, Peking University, 1996
M.S., Physics, Peking University, 1996
M.S., Electrical Engineering, The University of New Mexico, 2002

DISSERTATION

Submitted in Partial Fulfillment of the
Requirements for the Degree of

Doctor of Philosophy
Optical Science and Engineering

The University of New Mexico
Albuquerque, New Mexico

December 2006

To my parents and my family

ACKNOWLEDGMENTS

I would like to extend my deepest thanks to my advisors, Dr. Luke F. Lester and Dr. Diana Huffaker, for their encouragement, guidance, insight and support throughout the duration of my Ph.D.

I also thank my committee members, Dr. Jean-Claude Diels, Dr. Ralph Dawson and Dr. Thomas Sigmon, for their valuable recommendations pertaining to this study and reading and commenting on this manuscript.

I am very grateful to Dr. Martinez, Dr. L. Zhang, Dr. A. Gray, Dr. H. Li, and Dr. Andreas Stintz for their cooperation and valuable insights during this work

Thanks to Aaron Moscho, Yan Li, Therese Saiz, etc in L. Lester group for help in experiments, and to Ping-show Wong, Li Wang, Ganesh Balakrishnan, Dong Li, Deying Xia, Shuang Zhang, Ying Luo, Wenjun Fan, Jing Chen, Noppadon Nuntawong for their help and friendship. I have also benefited from help and friendship with Chris Hains, Douglas Wozniak, Joe Sadler, Maria Otero, Maria Otero, and Monica Fishel; their willingness to help will be remembered fondly.

Beth Fuchs, Dr. Guangtian Liu and Dr. Xiao Dong Huang and other guys, who trained me in the cleaning room, deserve unforgettable thanks.

And finally, I heartily acknowledge the persistent support and encouragement of my family. Nothing can be done without their support. To my son, Alex, you are the greatest gift I have.

QUANTUM DOT MULTI-SECTION LIGHT EMITTERS

BY

YONGCHUN XIN

ABSTRACT OF DISSERTATION

Submitted in Partial Fulfillment of the
Requirements for the Degree of

Doctor of Philosophy
Optical Science and Engineering

The University of New Mexico
Albuquerque, New Mexico

December 2006

QUANTUM DOT MULTI-SECTION LIGHT EMITTERS

By

Yongchun Xin

B.S., Physics, Peking University, 1996

M.S., Physics, Peking University, 1996

M.S., Electrical Engineering, The University of New Mexico, 2002

Ph.D, Optical Science, The University of New Mexico, 2006

ABSTRACT

$In_xGa_{1-x}As$ quantum dot (QD) lasers grown on a GaAs substrate with 1.3-μm emission are currently a subject of strong interest, and the work presented here extends this research to the field of multi-section light emitters. Multi-section QD devices are useful for materials characterization and their flexibility in layout makes multi-functional in their device performance. This dissertation discusses the use of multi-section light emitters to produce new methods in the optical characterization of materials, QD mode-locked lasers (MLLs) and QD super-luminescent light emitting diodes (SLEDs).

An improved, alternate approach to the "multi-section method" for the measurement of optical gain and absorption is presented, and for the first time, low noise, accurate gain and absorption spectra under real CW working conditions are obtained. With the improved multi-section method and MLL characteristic testing, the relationship between

quantum dot MLL performance and quantum dot parameters is studied. With the highly flexible, reconfigurable multi-section approach, we demonstrate novel designs of QD MLLs and SLEDs. The multi-section MLL significantly increases the peak pulsed power (> 45%) and improves the pulse width (>35%) of the device. With the ability to change absorber position in the optical cavity at will, harmonic mode-locking from 7.2 GHz to 51 GHz is achieved. The ridge-waveguide multi-section QD SLED allows independent adjustment of the power and the spectral bandwidth relative to the ground state (GS) and the excited state (ES) of the QD and demonstrates simultaneous ultra-wide 3-dB bandwidth (> 150 nm) and an output power greater than 1 mW with a uniform multi-stack QD structure.

TABLE OF CONTENTS

LIST OF FIGURES

LIST OF TABLES

Chapter 1 Introduction to Quantum Dot Lasers

1.1 A Brief History of Quantum Dot Semiconductor Lasers

Semiconductor laser technology has been greatly improved since the first semiconductor laser was demonstrated in 1962 [1]. The improvement includes both laser waveguide structures and semiconductor materials. The ridge laser, for instance, is used to improve the current confinement and provide weak index guiding. The distributed Bragg reflector laser (DBR) and distributed-feedback laser (DFB) were invented for better wavelength selection [2, 3]. For decreased threshold, many research groups have worked on vertical cavity surface emitting laser, microdisk lasers, and so on [4, 5].

Alferov, Hayashi and Panish dramatically reduced the threshold current density with the double heterostructure (DH) laser in the late sixties and hence room temperature continuous wave operation was achieved [6, 7]. Dingle and Henry demonstrated quantum the well (QW) laser in 1975 [8, 9] in which the QW confined the carriers within quantized energy levels and reduced the physical space volume [10,11, 12, 13]. The QW lasers further reduced the threshold and allowed some control over the wavelength by changing the QW thickness. After people realized that the application of size quantization effects would be very beneficial for semiconductor lasers, the theory describing the quantum dot (QD) was first proposed by Arakawa *et al* in 1982 as an extension of the QW and was called the "multidimensional quantum well" [14]. However, these theories were based on lattice-matched heterostructures. Many scientists believed these models were too ideal and strongly doubted that real QD lasers would demonstrate the predicted advantages. At the beginning of the 1990s, it was realized that self-assembly on surfaces due to the strain caused by the lattice mismatch can be used to form high density QD

layers [15, 16, 17]. In 1994, the first QD lasers based on self-assembled growth, with fully quantized energy levels in both bands and a strongly inhomogeneous broadened gain spectrum, were reported [18]. Since then, QD devices based on self-assembly have been remarkably improved and are used in a broad array of applications such as lasers, super-luminescent light emitting diodes, detectors, amplifiers, and solar cells [19, 20].

1.2 Formation of Self- Assembled Quantum Dots

From Figure 1-1, we can see that for different materials, their lattice constants are different. When one material is grown on top of another, if this material lattice constant is bigger than the underlying material, then there will be mismatch between those materials, specifically compressive strain. When a very thin layer of compressively mismatched material is deposited on the substrate, there is a growth regime where it is energetically favorable to increase surface area by islanding as opposed to relaxing the strain through dislocation generation. [21]

While there are several different ways to form quantum dots, self-assembled quantum dots grown by molecular beam epitaxy (MBE) is the most frequently used and has produced most of the devices with superior lasing characteristics. There are two common used growth modes–the Stranski-Krastanow (S-K) mode and the Atomic Layer Epitaxy (ALE) mode. In the case of InAs quantum dots grown on a GaAs substrate, Figure 1-2 illustrates the 2-D wetting layer and 3-D island formation in S-K mode that is responsible for forming the quantum dot.

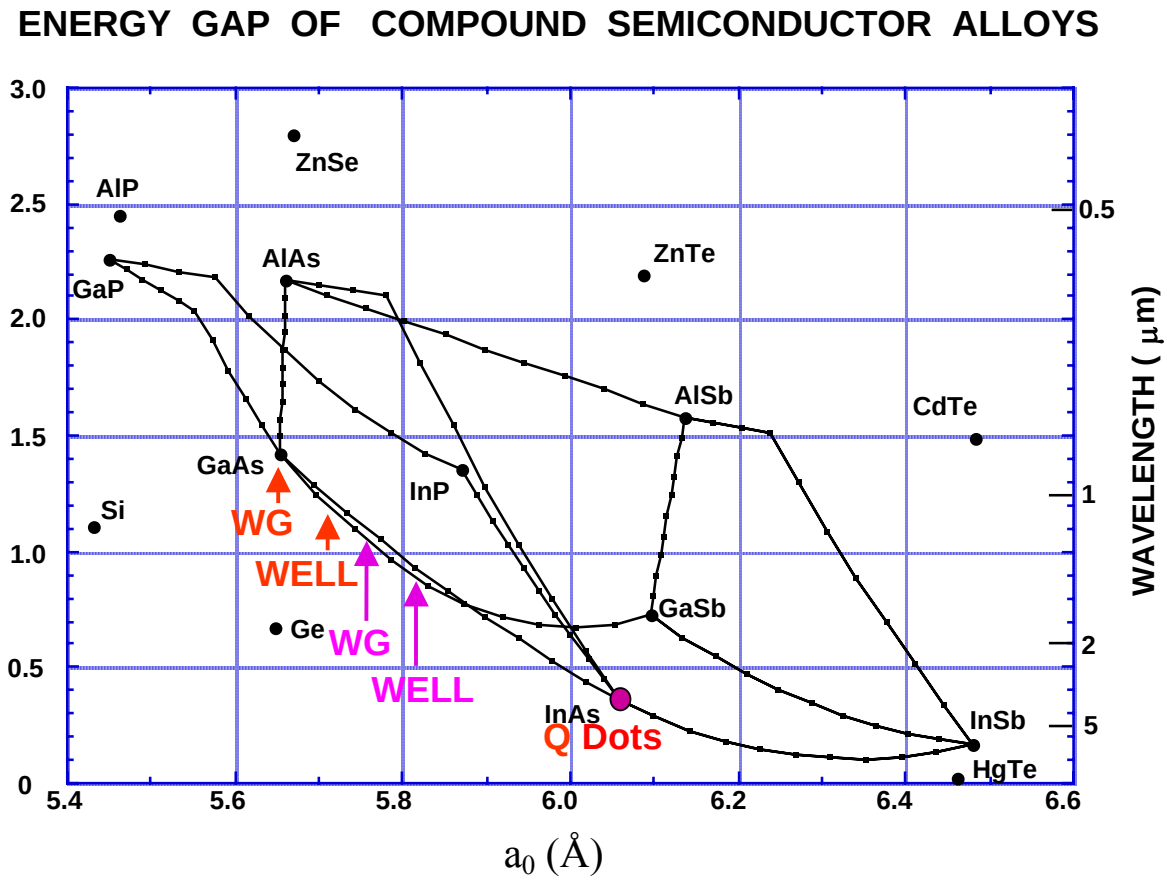

Figure 1-1 Energy gap vs. lattice constant. The red arrows show the wave-guide and quantum well lattice constant positions in a usual DWELL laser structure and the pink arrows show those positions in a DWELL laser structure with metamorphic buffer.

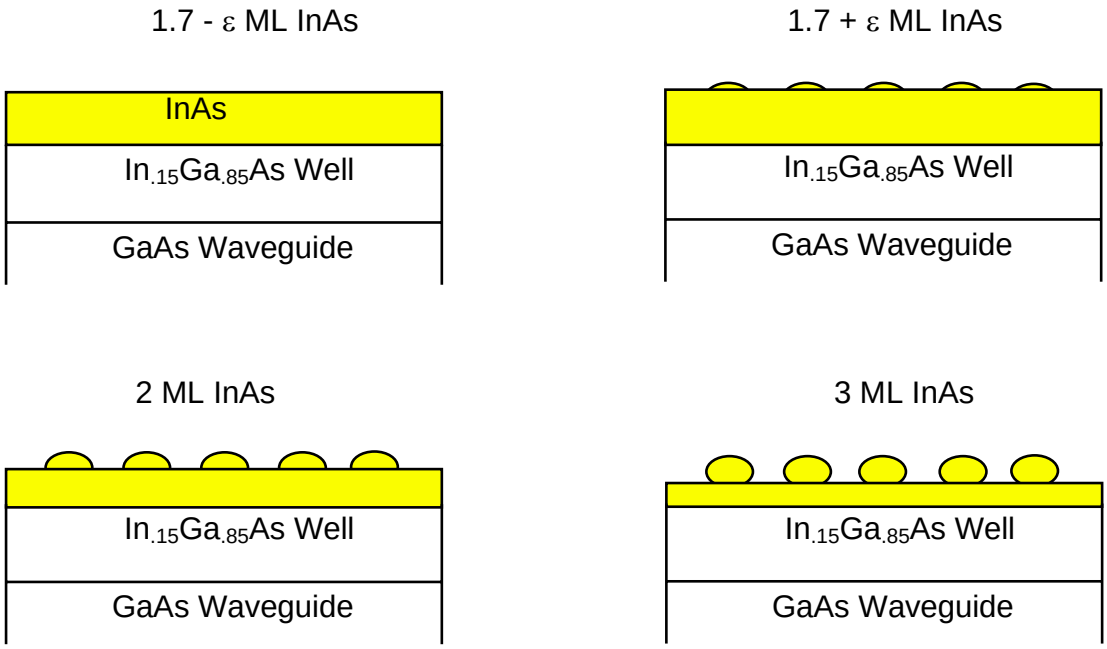

Figure 1-2 Self-assembly growth technique for InAs quantum dots by S-K mode

1.3 Why Quantum Dots for Lasers?

With quantum confinement in all 3 spatial directions, QDs has introduced new optical properties. We can understand this change by comparing the state density change for bulk (0-dimension), quantum well (1-dimension of confinement), quantum wire (2-dimensions) and quantum dot (3-dimensions). As illustrated in Figure 1-3, the state density in bulk materials is continuous and proportional to the square root of the energy. For QWs, the state density decreases compared to the bulk and looks like a step function. For the quantum wire, the state density further decreases compared to the QWs. For QDs, the state density is a δ-function in energy. For the real QDs materials, the density of states has a line broadening caused by fluctuations in the quantum dot sizes. Nonetheless, the density of state still decreases compared to the quantum wire.

Besides the size quantization effects, the realistic physical models of self-assembled QDs that are relevant to laser diodes are based on [9]

- Strained heterostructures
- Finite barriers
- Many electron and hole levels
- Monomolecular (excitonic) recombination
- Non-equilibrium carrier distribution.

With the self-assembled QDs models, some predictions of uniquely appealing features of quantum dot lasers compared to QW and DH lasers have attracted considerable attention and have been demonstrated on actual devices including:

Ultra low threshold current density. The much reduced density of states and smaller physical volume of the active material means there are fewer carriers necessary to invert

the carrier population in the QDs, which results in extremely low threshold current densities. In 1999, Liu, et al, decreased the threshold current density down to 26 A/cm^2 [22, 23, 24]. The threshold current density kept decreasing in the following years. Figure 1-4 shows the historical change in the threshold current density of quantum dot lasers (QD) [22 ,25, 26, 27, 28,], and compares it with DH lasers [29, 30] and QW lasers [10, 11, 12, 13]. The lowest recorded threshold of a quantum dot laser of 10 A/cm^2 has been achieved by Rabbit (1160nm) [9] and the UNM group (1270nm). With such low current density, there is a clearly heated competition between strained quantum dot lasers and quantum well lasers for the best 1.3-μm emission wavelength devices.

High T_0 value, temperature-insensitive threshold current. The T_0 value describes the threshold current dependence of the temperature. Since the threshold current has the empirical relation with the temperature as $I_{th}=I_0 \exp (T/T_0)$, high T_0 values means little variation of threshold current with temperature change. A high characteristic temperature of T_0 = 210 K was achieved in an un-doped self-assembled 1.3-μm InGaAs-GaAs quantum dot laser in 2004 [31]. Temperature invariant output slope efficiency and threshold current (T_0=infinity) in the temperature range of 5-75 °C have been measured for 1.3-μm p-doped self-organized quantum dot lasers [32].

Improved high-speed modulation. As described before, the quantum dot has a δ-function-like density of states, which results in both high material gain and high differential gain. Both of these factors contribute to a high modulation bandwidth [33]. In a theoretical study of the optical signal amplification and processing by quantum-dot semiconductor optical amplifiers (SOA's), Sugawara reported that QD devices should realize high-speed (40 to 160 Gb/s) pattern-effect-free wavelength conversion by cross-

gain modulation, low frequency chirping and symmetric, highly-efficient 1 to 2 THz wavelength conversion by the non-degenerate four-wave mixing [34, 35]. In 2003, an ultrawide-band high-power QD amplifier in the 1.5μm wavelength region on an InP substrate, which enabled signal regeneration at 40 Gb s^{-1}, was reported [36]. High-frequency modulation characteristics of 1.3-μm InGaAs quantum dot lasers were reported with small-signal modulation bandwidth of f_{3dB} = 12 GHz to 22GHz [31, 37, 36].

Decreased linewidth enhancement factor. The linewidth enhancement factor (α-parameter) is defined as the ratio of the change in the real part of the index of refraction with carrier density to the differential gain of the material. The strong symmetry of the δ-function-like density of states in dots is responsible through the Kramers-Kronig relation that links index and gain for very low α. Linewidth enhancement factors from 0.4 to 0.1 have been measured [38, 39].

Ultra-broad bandwidth, easily saturated gain and absorption. Due to the reduced δ-shape density of states of ideal QDs, the bandwidth of QD materials depends mostly on the inhomogeneous broadening that is caused by the QD's Gaussian-broadened size distribution. Therefore, the QDs materials can have much wider bandwidth compared with QW. Because of the finite density of states, it is also very easy to saturate the gain and absorption of QDs. These characteristics result in QDs being an ideal material system for mode-locked lasers (MLL) and super-luminescent light emitting diodes (SLEDs). The first QD MLL was reported in 2001 [40]. After that, all the characteristics of QD MLL have steadily improved. The reported repetition rate is up to 50 GHz [41] and the lowest jitter is down to 300 femtosecond [42]. For the SLEDs, the UNM group has reported SLEDs with record wide bandwidth up to 220 nm. We have also demonstrated

simultaneous ultra-wide 3-dB emission bandwidth (> 150 nm) and an output power greater than 1 mW with a uniform multi-stack QD structure.

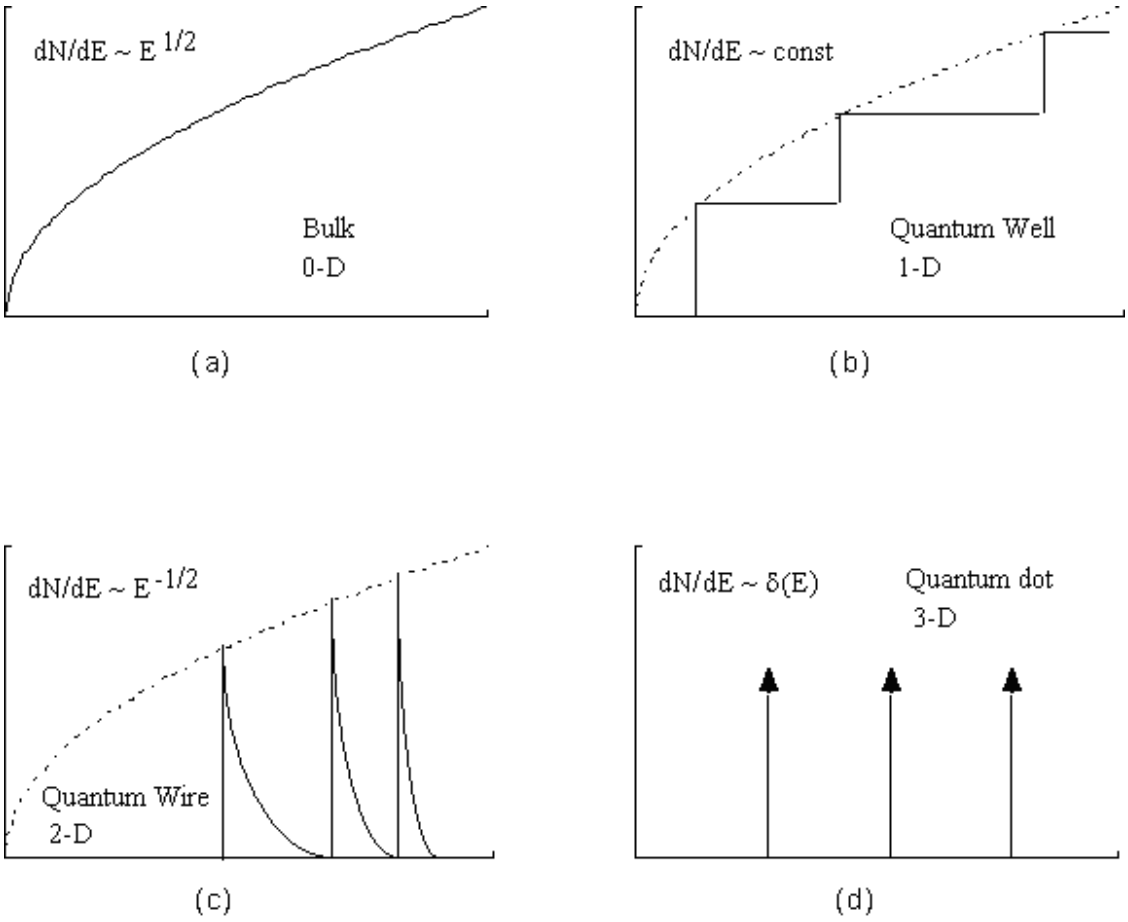

Figure 1-3 States Density Function for (a) Bulk, (b) Quantum Well, (c) Quantum wire, and (d) Quantum dot

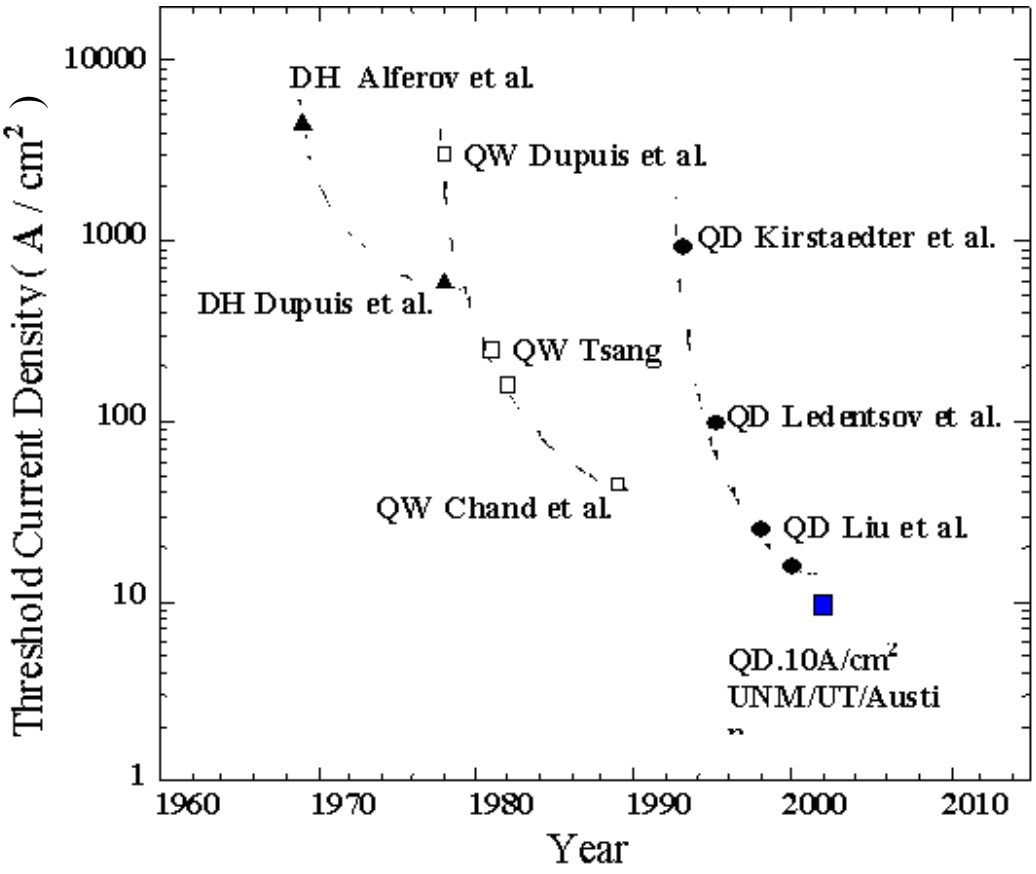

Figure 1-4 Room temperature electrically pumped semiconductor laser threshold current density reduction over last thirty years for Double Heterostructure (DH), Quantum Well (QW), and Quantum Dot (QD).

1.4 Dissertation Objectives

This dissertation includes four detailed discussions of InAs quantum dot multi-section emitters:

- Novel technique for obtaining gain and absorption under pulsed or CW conditions.
- Characterization of QD mode locked laser (MLL) with multi-section devices.
- Novel multi-section QD MLLs
- Novel multi-section SLED

$In_xGa_{1-x}As$ quantum dot lasers grown on a GaAs substrate with 1.3-μm emission are currently a subject of strong interest, which includes both device physics analysis and design. However, most of the previous research did not use CW operation and are therefore not entirely appropriate for robust device design. This dissertation treats mostly the CW behavior of the examined devices.

Fortunately, quantum dot lasers have extra low threshold current density because of the reduced density of states and this fact helps enormously in realizing CW operation in a variety of different applications. But in the mean time, the reduced density of states is accompanied by a much smaller modal gain in the quantum dot. For some applications such as DFB laser and VCSEL quantum dot laser, it is important to measure the gain spectrum of quantum dots under real working conditions. In chapter 2, an improved, alternate approach to the "multi-section method" [reference here] for the measurement of optical gain and absorption is presented, and for the first time, we obtain low noise, accurate gain and absorption spectra under CW conditions.

With the improved multi-section method and MLL characteristic testing, we study the relationship between quantum dot MLL performance and quantum dot parameters in the chapter 3. For the first time, all the important parameters governing pulse width in the Haus Master Equation and are measured in a single device, not from just test structures. With the multi-section, reconfigurable MLL approach, we demonstrate novel designs that significantly increase the peak pulsed power (> 45%) and improve the pulse width (>35%) of the devices. With the ability to change absorber position in the optical cavity at will, harmonic mode-locking from 7.2GHz to 51GHz is achieved.

In chapter 4, a ridge-waveguide QD SLED that emits near 1.3μm is introduced. The new SLED structure allows a high flexibility in the design and can be reconfigured to adjust independently the power and the spectral bandwidth relative to the ground state (GS) and the excited state (ES) of the QD. The multi-section device configuration enables the realization of an ultra-wide 3-dB bandwidth (> 150 nm) and an output power greater than 1 mW with a uniform multi-stack QD structure.

1.5 References For Chapter 1

1 R.N.Hall, G.E.Fenner, et al, “Coherent Light Emission From GaAs Junctions” Phys. Rev. Letter. 9,366, 1962

2 Okuda M, Onaka K, “Analysis Of Distributed Bragg-Reflector Laser-Amplifiers”, Japanese Journal Of Applied Physics, v. 16(#1) pp. 125-130, 1977

3 Evans G, Wilcox T, “Mode-Coupling And Distributed Feedback Lasers In Periodic Fiber Waveguides”, IEEE Journal Of Quantum Electronics, v. 13(#4) pp. 145-152, 1977

4 Sakaguchi T, Koyama F, Iga K, “Vertical Cavity Surface-Emitting Laser With An Aigaas/Aias Bragg Reflector”, Electronics Letters, v. 24(#15) pp. 928-929, 1988

5 Koch Sw, Jahnke F, Chow Ww, “Physics Of Semiconductor Microcavity Lasers”, Semiconductor Science And Technology, v. 10(#6) pp. 739-751, JUN 1995

6 Z. I. Alferov, V. M. Andreev, V. I. Korol’kov, E. L. Portnoi, and D.N. Tret’yakov, "Injection properties of n-Al Ga As-p-GaAs hetero-junctions", Fiz. Tekh. Poluprovodn., vol. 2, pp. 1016 1017, 1968. Sov.Phys.-Semicond., vol. 2, p. 843-844, 1969.

7 I. Hayashi, M. B. Panish, P. W. Foy, and S. Sumski, "Junction lasers which operate continuously at room temperature" Appl. Phys. Lett., vol.17, pp. 109-111, 1970.

8 Tsang Wt, Weisbuch C, Miller Rc, Dingle R, “Current Injection Gaas-Alxga1-Xas Multi-Quantum-Well Heterostructure Lasers Prepared By Molecular-Beam Epitaxy” Applied Physics Letters , v. 35(#9) pp. 673-675, 1979

9 Bimberg, D., "Quantum dots for lasers, amplifiers and computing," Journal of Physics D-Applied Physics, vol. 38, no. 13, pp. 2055-2058, 2005.

10 R. D. Dupuis, P. D. Dapkus, N. Holonyak Jr., E. A. Rezek, R. Chin, "Room Temperature operation of quantum-well Ga1-xAlxAs-GaAs laser diodes grown by metalorganic chemical vapor deposition", Appl. Phys. Lett. 32, 295-297, 1978

11 W. T. Tsang, "Extremely low threshold (AlGa)As modified multiquantum well heterostructure lasers grown by molecular-beam epitaxy", Appl. Phys. Lett. 39, 786-788, 1981

12 W. T. Tsang, "Extremely low threshold (AlGa)As graded-index waveguide separate-confinement heterostructure lasers grown by molecular-beam epitaxy", Appl. Phys. Lett. 40, 217-219, 1982

13 N. Chand, E. E. Becker, J. P. Van der Zeil, S. N. G. Chu, and N. K. Dutta, "Excellent uniformity and very low (less-than-50A/cm2) threshold current density strained InGaAs quantum-well diode-lasers on GaAs substrate "Appl. Phys. Lett. 58, 1704-1706, 1991

14 Y. Arakawa, and H. Sakaki, "Multidimensional quantum well laser and temperature dependence of its threshold current", Appl. Phys Lett., 40 (11), 939-941, 1982

15 Leonard, D., Fafard, S., Pond, K., Zhang, Y. H., Merz, J. L., And Petroff, P. M., "Structural And Optical-Properties Of Self-Assembled Ingaas Quantum Dots," *Journal Of Vacuum Science & Technology B*, Vol. 12, No. 4, Pp. 2516-2520, 1994.

16 Bimberg, D., Grundmann, M., Ledentsov, N. N., Ruvimov, S. S., Werner, P., Richter, U., Heydenreich, J., Ustinov, V. M., Kopev, P. S., and Alferov, Z. I., "Self-organization processes in MBE-grown quantum dot structures," Thin Solid Films, vol. 267, no. 1-2, pp. 32-36, 1995.

17 Petroff, P. M. And Denbaars, S. P., "Mbe And Mocvd Growth And Properties Of Self-Assembling Quantum-Dot Arrays In Iii-V Semiconductor Structures," Superlattices And Microstructures, Vol. 15, No. 1, Pp. 15-21, 1994.

18 Kirstaedter, N., Ledentsov, N. N., Grundmann, M., Bimberg, D., Ustinov, V. M., Ruvimov, S. S., Maximov, M. V., Kopev, P. S., Alferov, Z. I., Richter, U., Werner, P., Gosele, U., And Heydenreich, J., "Low-Threshold, Large T-O Injection-Laser Emission From (Inga)As Quantum Dots," Electronics Letters, Vol. 30, No. 17, Pp. 1416-1417, 1994.

19 A. Stintz, G. T. Liu, H. Li, L. F. Lester, and K. J. Malloy, "Low Threshold Current Density 1.3μm InAs quantum dot lasers with the Dots-in-a-Well (DWELL) structure", IEEE Photon. Technol. Lett. 13, 2000

20 Ustinov VM, Maleev NA, Kopev PS, et al, "InAs/InGaAs quantum dot structures on GaAs substrates emitting at 1.3 μm", Appl. Phys. Lett. 74, (19), pp. 2815, 1999

21 L. Goldstein, F. Glas, J. Y. Marzin, M. N. Charasse, G. Leroux, " Growth by molecular beam epitaxy and characterization of InAs/GaAs strained-layer superlattices", Appl. Phys. Lett. **47** (10), 1099-1101, 1985

22 G. T. Liu, A. Stintz, H. Li, K. J. Malloy, and L. F. Lester, " Extremely Low Room-Temperature Threshold Current Density Diode Lasers Using InAs Dots in an $In_{.15}Ga_{.85}As$ Quantum Well", Electron. Lett., 35, 1163-1165, 1999

23 G. Park, O. B. Shchekin, D. L. Huffaker, D. G. Deppe: "Low-Threshold Oxide-confined 1.3μm Quantum-Dot Laser ", IEEE Photon. Technol. Lett. 13, 230-232, 2000

24 A. Stintz, G. T. Liu, H. Li, L. F. Lester, and K. J. Malloy, "Low Threshold Current Density 1.3μm InAs quantum dot lasers with the Dots-in-a-Well (DWELL) structure", IEEE Photon. Technol. Lett. 13, 2000

25 N. Kirstaedter, N. N. Ledentsov, J. Heydenreich, et al, "Low-threshold, large T_0 injection-laser emission from (InGa)As quantum dots, Electron. Lett. 30 (17), 1416-1417, 1994

26 D.L. Huffaker, G. Park, Z. Zou, O.B. Shchekin,, and D. G. Deppe, "1.3 μm room-temperature GaAs-based quantum-dot Laser," Appl. Phys. Lett., **73** (18), 2564-2566, 1998

27 N. N. Ledentsov, V. A. Shchukin, M. Grundmann, N. Kirstaedter, J. Böhrer, O. Schmidt, D. Bimberg, V. M. Ustinov, A. Yu. Egorov, A. E. Zhukov, P. S. Kop'ev, S. V. Zaitsev, N. Yu. Gordeev, Zh. I. Alferov, A. I. Borovkov, A. O. Kosogov, S. S. Ruvimov, P. Werner, U. Gösele, and J. Heydenreich, " Direct formation of vertically coupled quantum dots in Stranski-Krastanow growth", Phys. Rev. B **54**, 8743-8750 (1996)

28 G. T. Liu, A. Stintz, H. Li, T.C, Newell, L. F. Lester and K.J. Malloy" Very Low Room Temperature Threshold Current density Dots-in-a-Well Lasers" 1999 IEEE LEOS annual meeting, San Francisco.

29 Zh. I. Alferov, V. M. Andreev, E. L. Portnoi, M. K. Trukan, "AlAs-GaAs heterojunction injection lasers with a low room-temperature threshold", Sov. Phys. Semicond. 3, 1107-1110, 1970

30 R. D. Dupuis, and P. D. Dapkus, "Very low threshold Ga1-xAlxAs-GaAs double-heterostructure lasers grown by metalorganic chemical vapor deposition", Appl. Phys. Lett. 32, 473-475, 1978

31 Kim, S. M., Wang, Y., Keever, M., and Harris, J. S., "High-frequency modulation characteristics of 1.3-mu m InGaAs quantum dot lasers," *IEEE Photonics Technology Letters*, vol. 16, no. 2, pp. 377-379, 2004.

32 Fathpour, S., Mi, Z., Bhattacharya, P., Kovsh, A. R., Mikhrin, S. S., Krestnikov, I. L., Kozhukhov, A. V., and Ledentsov, N. N., "The role of Auger recombination in the temperature-dependent output characteristics (T-0 = infinity) of p-doped 1.3 mu m quantum dot lasers," *Applied Physics Letters*, vol. 85, no. 22, pp. 5164-5166, 2004.

33 K. Y Lau and A. Yariv, “Ultrahigh Speed Semiconductor Lasers,” IEEE J. Quantum Electron., 21, pp. 121-138, 1985

34 Sugawara, M., Akiyama, T., Hatori, N., Nakata, Y., Ebe, H., and Ishikawa, H., "Quantum-dot semiconductor optical amplifiers for high-bit-rate signal processing up to 160 Gb s(-1) and a new scheme of 3R regenerators," *Measurement Science & Technology*, vol. 13, no. 11, pp. 1683-1691, 2002.

35 Sugawara, M., Ebe, H., Hatori, N., Ishida, M., Arakawa, Y., Akiyama, T., Otsubo, K., and Nakata, Y., "Theory of optical signal amplification and processing by quantum-dot semiconductor optical amplifiers," *Physical Review B*, vol. 69, no. 23, pp. 235332, 2004.

36 Sugawara, M., Hatori, N., Ishida, M., Ebe, H., Arakawa, Y., Akiyama, T., Otsubo, K., Yamamoto, T., and Nakata, Y., "Recent progress in self-assembled quantum-dot optical

devices for optical telecommunication: temperature-insensitive 10 Gbs(-1) directly modulated lasers and 40Gbs(-1) signal-regenerative amplifiers," *Journal of Physics D-Applied Physics*, vol. 38, no. 13, pp. 2126-2134, 2005.

37 Fathpour, S., Mi, Z., and Bhattacharya, P., "High-speed quantum dot lasers," *Journal of Physics D-Applied Physics*, vol. 38, no. 13, pp. 2103-2111, 2005.

38 T. C. Newell, D. Bossert, A. Stintz, B. Fuchs, K. J. Malloy, and L. F. Lester, "Gain And Linewidth Enhancement Factor In InAs Quantum Dot Laser Diodes," IEEE Photon. Technol. Lett. 11, 1527, 1999

39 Schneider, S., Borri, P., Langbein, W., Woggon, U., Sellin, R. L., Ouyang, D., and Bimberg, D., "Linewidth enhancement factor in InGaAs quantum-dot amplifiers," *IEEE Journal of Quantum Electronics*, vol. 40, no. 10, pp. 1423-1429, 2004.

40 Huang, X. D., Stintz, A., Li, H., Lester, L. F., Cheng, J., and Malloy, K. J., "Passive mode-locking in 1.3 mu m two-section InAs quantum dot lasers," *Applied Physics Letters*, vol. 78, no. 19, pp. 2825-2827, 2001.

41 Kuntz, M., Fiol, G., Lammlin, M., Bimberg, D., Thompson, M. G., Tan, K. T., Marinelli, C., Wonfor, A., Sellin, R., Penty, R. V., White, I. H., Ustinov, V. M., Zhukov, A. E., Shernyakov, Y. M., Kovsh, A. R., Ledentsov, N. N., Schubert, C., and Marembert, V., "Direct modulation and mode locking of 1.3 mm quantum dot lasers," *New Journal of Physics*, vol. 6 pp. 181, 2004.

42 Lei Zhang, et al, “5 GHz Optical Pulses From a Monolithic Two-Section Passively Mode-locked 1250/1310 nm Quantum Dot Laser for High Speed Optical Interconnects”, OFC 2005.

Chapter 2 Determination of Optical Gain and Absorption of Quantum Dots with The Improved Segmented Contact Method

2.1 Introduction

Because of the delta-function density of states and low active volume, quantum dot lasers have some uniquely appealing features including an ultra-low threshold current density and a small temperature dependence of the threshold current. However, the reduced density of states that facilitates the low transparency current and the resulting low threshold current density is accompanied by small modal gain, which is much smaller than the modal gain of conventional quantum well lasers.

For understanding the fundamental processes in QDs and optimizing the design of QD optical devices, such as DFB lasers and VCSELs that have generally larger loss than Fabry-Perot devices and therefore require larger modal gain and detailed design of the cavity structure, it is essential to obtain accurate gain and absorption spectra. There are various groups that have studied the optical modal gain of quantum dots in both theory and experiment [1, 2, 3, 4, 5]. The conventional method of determining the modal gain is from measurements of mirror loss, internal loss, and threshold current density, which can only give the peak gain vs. injected current density and the corresponding wavelength at this peak gain. Because of this restriction, it is difficult to get the modal gain spectrum over the whole emission region, especially under CW conditions. This chapter will introduce the measurement and characterization of the modal gain of multi-stack quantum dot lasers by an improved segmented contact method.

How the modal gain is measured is important. The conventional method of determining the optical mode loss, α_i, from measurements of the external differential efficiency of devices with different lengths relies on the assumption that the quasi-Fermi levels are pinned above threshold. This method is appropriate for QD lasers by restricting operation to the low-pump limit. The reason being that pumping of the excited states may occur above threshold in devices due to inhomogeneous broadening or lack of Fermi-level pinning. In multiple layer quantum well devices, for example, it has been observed that carrier transport effects can lead to unequal populations in different wells and poor quasi-Fermi level pinning [6, 7, 8]. Another problem of this method is it can only get individual points but not the spectra of gain and absorption. Another conventional method is the Hakki–Paoli technique. The Hakki–Paoli technique calculates the gain spectrum by analyzing the longitudinal modes in the stimulated emission [9]. For this technique, a high spectral resolution is required and this technique is limited to current densities below the threshold of the device. The Henry technique [ref] is an indirect method to obtain the gain spectra by calculating the Fermi-level energy separation. It does not directly give gain in absolute units and, similar to the Hakki–Paoli technique, limits the current density to below the threshold value of the device.

In the past, the segmented contact method was successfully used to measure the gain and absorption of quantum well materials by analyzing the edge-emitted amplified spontaneous emission spectra (ASE) [10, 11, 12]. In the standard data reduction of results from the segmented-contact method, unguided spontaneous emission due to leakage currents is not treated, which introduces error into the calculated gain and absorption. Such error cannot be ignored in quantum dot devices due to its smaller modal gain (10-

20/cm) and loss values. Other researchers have proposed ways of eliminating these errors but they tend to be relatively complex [13].

The improved segmented contact method is simple to implement and works by manipulating the data from single, double, and triple biased sections. The new approach subtracts background signals from the measurement, resulting in clean, accurate gain and absorption spectra. The alternative method is especially efficient for characterizing materials with small gain or absorption. Using a self-calibration method, a quantum dot gain spectrum is measured to an accuracy of less than 0.2 cm^{-1} at nominal gain values below 2 cm^{-1}. This capability also enables precise measurement of waveguide internal loss, unamplified spontaneous spectra and Stark shift data.

2.2 Theory of the Improved Segmented Contact Method

2.2.1 Conventional segmented contact method

The conventional segmented contact method, or "single-pass multi-section device" method, is based on the measurement of the amplified spontaneous emission (ASE) [10]. For the ASE, signals exist propagating in both directions along the optical cavity axis. The intensity, *I*, of the ASE that propagates in the positive x-direction is a function of the net modal gain, *g*, and the signal testing position, *x* [14, 15]:

$$\frac{dI}{dx} = gI + S$$

$$g = \Gamma g_m - \alpha_i$$

Eqn 2-1

Where the S is the intensity of the spontaneous emission emitted in all directions. Γ is the optical confinement factor, g_m is the material gain and α_i is the internal loss. Solving this equation, we can get the solution of I after the signal propagates a distance L:

$$\ln(I+\frac{S}{g})-\ln(I_0+\frac{S}{g})=GL \qquad \text{Eqn 2-2}$$

I_0 is the intensity of signal at $x = 0$ and for $x<0$, there is no injected current. For the single pass method, there is no ASE at $x=0$, so $I_0 = 0$. We obtain the solution as [16]:

$$I_{ASE}=\frac{S}{g}\left(\exp(g\cdot x)-1\right) \qquad \text{Eqn 2-3}$$

Now, if the ASE propagates a distance L and then $2L$, we can solve the equations to eliminate S and obtain [7]:

$$\begin{cases} I_L=\dfrac{S}{g}\left(e^{gL}-1\right) \\ I_{2L}=\dfrac{S}{g}\left(e^{2gL}-1\right) \end{cases} \qquad \text{Eqn 2-4}$$

$$g=\frac{1}{L}\ln\left(\frac{I_{2L}}{I_L}-1\right) \qquad \text{Eqn 2-5}$$

Equation 2-5 is the basic governing formula for the single pass multi-section method in which the ASE emitted from sections of length L and $2L$ are measured and put into a ratio to find the optical gain.

We can also get the total loss from the single pass method. For the condition that the emission signal propagates only in the $+x$ direction and that $I=0$, we can define the

ASE intensity at x_0 to be I_{x0}, and I_{x1} at x_1 ($x_1 > x_0$). From Equation 2-1, S=0 because there is no injected current. The solution then is:

$$I_{x1} = I_{x0} e^{-\alpha(x_1 - x_0)} \qquad \text{Eqn 2-6}$$

Here α is absorption. Rearranging, it can be calculated with Equation 2-7:

$$\alpha = -\frac{\ln\left(\frac{I_{x1}}{I_{x0}}\right)}{(x_1 - x_0)} \qquad \text{Eqn 2-7}$$

The conventional segmented contact method is usually performed with a device that has several electrically isolated sections as shown in the Figure 2-1. Each section has a length of L. In the testing, the first section is pumped with current density J to obtain I_L. Pumping both the first and second sections with current density of J yields I_{2L}. All of the other sections are reverse biased to eliminate the reflected light from the back facet.

The segmented contact method was successfully used to measure the gain and absorption of quantum well materials. However, in this familiar method, the unguided spontaneous emission is ignored. The unguided spontaneous emission will introduce error into gain and absorption data. The relation between ASE intensity and optical gain is not as Equation 2-4, but follows:

$$I = I_{ASE} + I_{leak} \qquad \text{Eqn 2-8}$$

Here the I_{leak} is the unguided spontaneous emission intensity. One possible source for the unguided spontaneous is leakage current in the device. With Equation 2-8, the Equations 2-5 and 2-7 are not tenable and there will be error in the net modal gain and loss calculation. For a quantum well (QW) gain medium, such error can be ignored given the relatively large gain of a QW sample.

2.2.2 Improved segmented contact method

For a QD amplifier, in which gain and loss both are much smaller than the QW, the error, which is introduced by the unguided spontaneous emission, cannot be ignored. To eliminae this error, we introduced an improved segmented contact method that is implemented by manipulating the data from single, double, and triple biased sections.

In our improved segmented-contact method, we calculate the net modal gain g by analyzing the ASE intensity using three different configurations of the pumped device. First, we measure the ASE intensity I_1 while only the first section is biased with a current density of J_1. Then, we measure the ASE intensity I_2 from a two-section configuration where the first and second sections are biased respectively with current densities J_1 and J. Finally, the ASE intensity I_3 is measured when the first section is pumped with a current density J_1 while the second and the third sections are biased with the same current density J. From the equations 2-2 and 2-8, the ASE intensities of I_1, I_2, and I_3 can be expressed as:

$$
\begin{aligned}
I_1 &= \frac{S_1}{g_1}\left[\exp(g_1 L)-1\right] + I_{leak1} \\
I_2 &= \frac{S}{g}\exp(g_1 L)\left[\exp(gL)-1\right] + \frac{S_1}{g_1}\left[\exp(g_1 L)-1\right] + I_{leak2} \\
I_3 &= \frac{S}{g}\exp(g_1 L)\left[\exp(2gL)-1\right] + \frac{S_1}{g_1}\left[\exp(g_1 L)-1\right] + I_{leak3}
\end{aligned}
\qquad \text{Eqn 2-9}
$$

The g_1 and g correspond to the net modal gains when a section is biased with a current density of J_1 and J, respectively. For the device geometries described above, most of the unguided spontaneous emission from sections 2 and 3 will radiate into the substrate before the coupling lens can collect it as shown in the Figure 2-5. Section 1 is the dominant source of unguided spontaneous emission; therefore, it is a reasonable

assumption that I_{leak} is the same for the different pumping configurations described above. As a result we have:

$$\frac{I_{3L}-I_L}{I_{2L}-I_L}=\frac{\exp(3gL)-\exp(gL)}{\exp(2gL)-\exp(gL)}=\exp(gL)+1 \qquad \text{Eqn 2-10}$$

In this case, the expression for the net modal gain g simplifies to:

$$g=\frac{1}{L}\ln\left(\frac{I_{3L}-I_L}{I_{2L}-I_L}-1\right) \qquad \text{Eqn 2-11}$$

With equation 2-11, the background signals are subtracted from the measurement, which results in a clean, accurate gain spectrum.

The absorption measurement can be corrected as well. To eliminate the error, the ASE intensity is measured in three different cases. I_1 is obtained when the first section is pumped with a current density of J_1; I_2 is measured when the first section is pumped with a current density J_1 and the second section with a current density J; I_{31} is measured while the first section is pumped with a current density of J_1, the second section has reverse voltage, and the third section is biased with a current density of J. Assuming that I_{leak} is the same for the different configurations, we can write

$$\begin{aligned} I_1 &= \frac{S}{g}\left(\exp(g\cdot L)-1\right)+I_{leak} \\ I_{21} &= \frac{S}{g}\left(\exp(g\cdot 2L)-1\right)+I_{leak} \\ I_{31} &= \frac{S}{g}\left(\exp(g\cdot L)-1\right)\exp\left((g-\alpha)\cdot L\right) \\ &\quad +\frac{S}{g}\exp(g\cdot L)-\frac{S}{g}+I_{leak} \end{aligned} \qquad \text{Eqn 2-12}$$

So

$$\frac{I_{21} - I_{31}}{I_{31} - I_1} = \exp(\alpha \cdot L) \qquad \text{Eqn 2-13}$$

The absorption α will be calculated by the following equation

$$\alpha = \frac{1}{L} \ln\left(\frac{I_{21} - I_1}{I_{31} - I_1}\right) \qquad \text{Eqn 2-14}$$

With Equation 2-14, the background signals are subtracted from the absorption measurement and the result is an accurate absorption spectrum.

In equations 2-11 and 2-14, the error introduced by the unguided emission is eliminated and a more accurate calculation of the gain and absorption is obtained over the whole spectrum [17]. Normally, the calculation will use the same current density and gain values throughout. However, the present technique allows for the gain and pump current density of the first section to be different from the other two. This alternative allows flexibility in biasing the front section for strong amplification, thus, a better signal to noise ratio in the case of a low light level from sections 2 and 3.

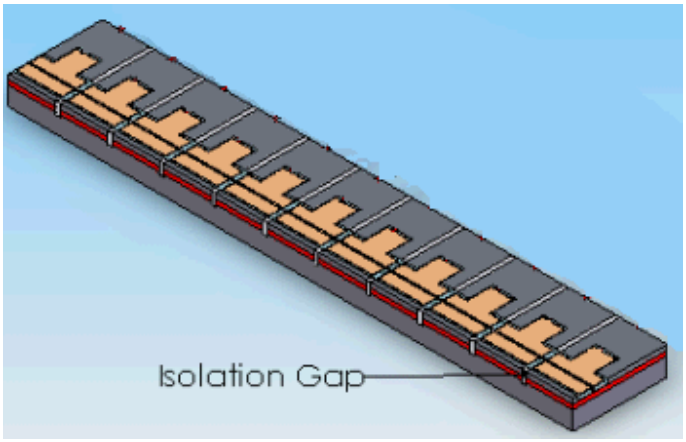

Figure 2-1 Structure of segmented contact device

2.3 Devices and Measurement Setup

2.3.1 Device structure and growth

With the improved segmented contact method, we characterized many QW and QD materials. As examples, three typical materials are introduced in this section. The segmented contact devices were processed using a six-stack dots-in-a-well (DWELL) laser structure, and a two-stack self-assembled InAs quantum dash-in-a-well (QDASH) on InP wafer.

The DWELL laser structure (Zia414) was grown by elemental source molecular beam epitaxy (MBE) on an n+-doped, <100> oriented GaAs substrate. The structure is shown in Figure 2-2. The epitaxial layers consist of an n-type (10^{18} cm^{-3}) 300-nm-thick GaAs buffer, an n-type lower $Al_{0.7}Ga_{0.3}As$ cladding layer, a 230-nm-thick GaAs waveguide surrounding the laser active region, a p-type upper cladding layer, and a p-doped (3×10^{19} cm^{-3}) 60-nm-thick GaAs cap. The cladding layers are doped at 10^{17} cm^{-3} and are each 2 μm thick. In the center of the waveguide, six DWELL layers were grown. In each layer, an equivalent coverage of 2.4 monolayer InAs QDs are confined approximately in the middle of a 10 nm $In_{0.15}Ga_{0.85}As$ QW. The QDs grown under these conditions have an area density of 7.5×10^{10} cm^{-2}, a base diameter <40 nm, and are about 7 nm high as determined by AFM measurements on a separate calibration sample. [18, 19].

The QDASH laser structure (Run1809) is grown on an n+ doped (001) InP substrate by MBE. Its active region consists of 2 stacks of InAs QDASHs in an $Al_{0.3}Ga_{0.03}In_{0.67}As$ compressively-strained QW separated by 50 nm of nominally lattice-matched

$Al_{0.3}Ga_{0.18}In_{0.52}As$ barrier. The active region is centered in a 1000 nm wide $Al_{0.3}Ga_{0.18}In_{0.52}As$ - waveguide. The cladding on the n-side is 100 nm Si-doped lattice-matched $Al_{0.48}In_{0.52}As$ (and the InP substrate), and on the p side is 1500 nm thick Be-doped $Al_{0.48}In_{0.52}As$. The structure has been capped with 150 nm Be-doped $Ga_{0.47}In_{0.53}As$. At the interfaces between the InP substrate and the n-cladding, between the cladding and waveguide, and the p-cladding and cap, graded quaternary layers have been grown to avoid steep changes in band energy. The InP substrate's surface orientation is 3^o off (001) toward (111B). This mis-cut substrate features atomic steps, which run perpendicular to [01-1], the direction of elongation of self assembled InAs-quantum dashes [20].

2.3.2 Device processing

For measuring the optical gain and absorption, the wafers are processed into multi-section devices following standard ridge waveguide laser processing. Wafers were processed to be 3 μm wide, deep-etched ridge waveguides with 16-segmented contact sections. Each section is 0.5-mm and the optical cavity length is 8 mm. The processing recipe is described in Figure 2-3.

After the first lithography with the ridge-waveguide-mask, the sample was etched to form 3μm wide, 1.8μm deep ridges by inductively coupled plasma (ICP) etching in BCl_3. Then the standard BCB processing was applied for isolating between the p-type metal and the etched cladding layer. The segmented-contact mask was used to make photoresist patterns for the p-type metal deposition and ion implantation. The isolation between the adjacent sections is provided by proton implantation, with an isolation resistance of >10 MΩ. After n-type metal deposited on the substrate side of the wafer, the sample was

annealed at 380°C for 1 minute. A temperature greater than 380°C can crack the BCB. Another Ti/Au metal layer was deposited for n-side mounting.

Such a device can be tested with either a free space coupling system or a single mode fiber. By changing the bonding configuration, different section-length devices can be created. In the following testing, two different section lengths were used, 1-mm/section and 1.5-mm/section. For the 1-mm/section testing, the first six (0.5-mm) sections of the device were configured by wire-bonding to form three 1-mm sections. The last ten sections were bonded together as an absorber to eliminate back reflections, shown as Figure 2-4. For the 1.5-mm/section test device, the first nine sections of device were wire-bonded to form three 1.5mm-sections, and the last eight sections were used as an absorber.

2.3.3 The net modal gain and loss measurement setup

The devices were mounted p-side up on an AlN submount on a copper heat sink. A TE cooler was used to control the heat sink temperature at 25 °C. The sections were wire-bonded and connected to a switch mechanism, with the exception of the absorption section. A reverse bias of 7V was applied to the absorption section to minimize reflection from the back facet.

The test setup includes two main blocks, an electrical-pumping block, and a signal-detecting block. Each of these two blocks has two configurations used in the net modal gain and absorption measurements. For the current-pumping block, we can choose either pulse-pumping or continuous-wave (CW) pumping. The pulse-pumping setup is mostly used for studying physical properties of the materials to avoid any heating effects in the measurement. The CW-pumping setup is used to determine the characteristics of the

device under actual working conditions. For the signal-detecting block, a free-space-coupling or a fiber-coupling setup can be used for different measuring requirements.

Two typical systems with their different blocks are shown in Figure 2-5. The Figure 2-5 (a) is the free space coupling setup with a monochromator and pulsed current pumping and (b) is the fiber-coupling setup with an optical spectrum analyzer (OSA) and CW-pumping. The setup in Figure 2-5 (b) has the potential for much faster data acquisition.

For pulsed pumping, the current source is triggered by an electrical signal-chopping system in order to decrease noise. The chopper includes two signal generators: an RC generator and a programmable waveform synthesizer. The RC generator provides a 1kHz sine-signal, which is used as the reference signal of the lock-in amplifier and the trigger signal for the programmable wave-form synthesizer. The programmable wave-form synthesizer works under gated mode to produce a 200 kHz sine wave signal, triggering the pulse current source. The injected pulsed current is generated by one current source and distributed to the different sections using three switches. The output signal from the wave-form synthesizer is shown in the Figure 2-6. The current applied through each section corresponds to the total current divided by the number of sections. Special care is taken that each section has very similar resistance characteristics. The current pulse is monitored with an oscilloscope. In the CW operation, each section has a dedicated current source. The bias current is checked with a multi-meter.

In the free-space-coupling setup block, the emission from the device is collected into a monochromator by lenses. A polarizer was placed between the first and second lens to select the TE-mode or the TM-mode emission. In this experiment, an InGaAs detector

cooled to 213K converted the light into an electrical signal. The latter is then amplified by a lock-in amplifier and recorded with the computer. The fiber-coupling setup is easier and faster for alignment and data collection. In the fiber-coupling system, the emission from the device is coupled into a polarization-maintaining fiber (PMF) by means of a coupling lens. An isolator was inserted to reduce reflection. An inline fiber-polarizer is connected to the PMF to select the TE mode or TM mode emission by switching the direction of the key on the FC connector. An OSA measures the ASE spectrum. The fiber-coupling setup has a bandwidth limit of 1.7 μm due to the OSA. In this dissertation, all data are based on TE mode emission.

The optical gain and absorption spectra are measured according to the theory described above. There is a calibration factor between the real ASE spectrum and the test spectrum, although this factor is the same for all spectra at a given wavelength, since the position of the device does not change during the testing. This factor is canceled by the net modal gain or absorption calculation, and the entire gain and absorption spectrum can be obtained with Equations 2-11 and 2-14. In fact, the alignment tolerances of the measurement described here is considerably relaxed compared to previous methods, but alignment stability is still important.

As introduced in the previous section, the pulsed-pumping setup is used mainly for studying the physical properties of the materials. The broad area device processed from the QDASH device (Run1809) did not lase at room temperature so the multi-section device of Run1809 was tested under pulsed-pumping setup to determine its optical properties. The multi-section QD devices of Zia414 were tested under CW operation.

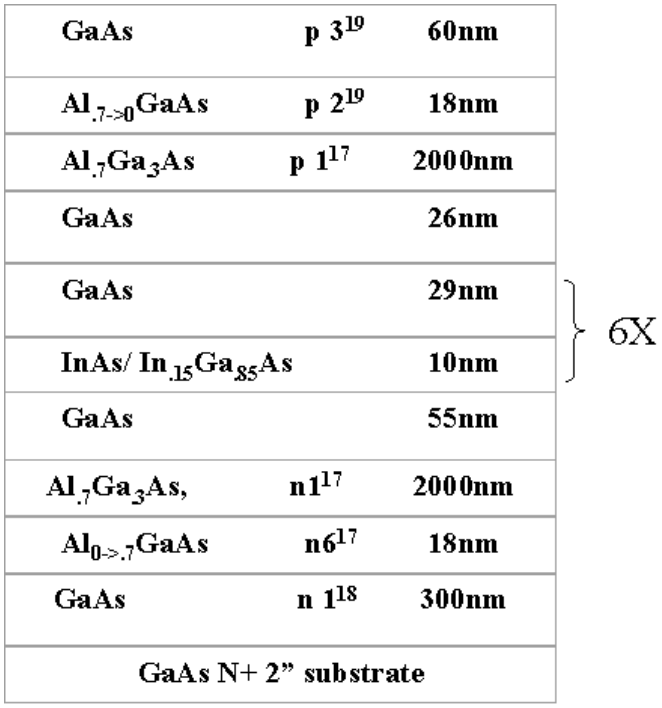

Figure 2-2 Structure of the 6-stack DWELL laser (Zia414)

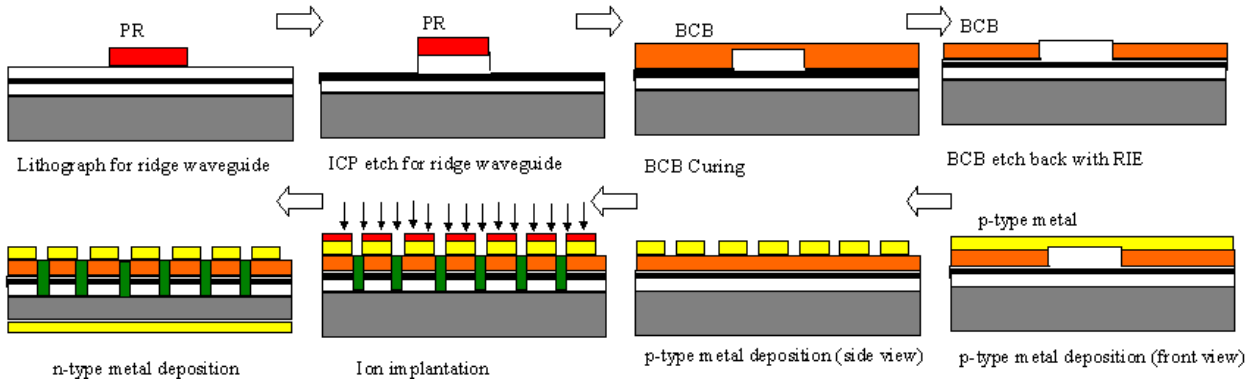

Figure 2-3. Processing of the segmented contact device

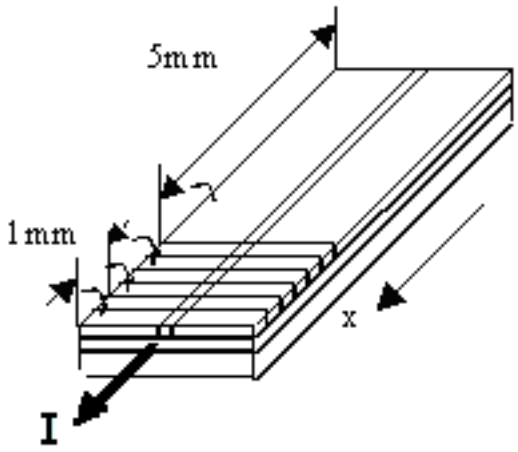

Figure 2-4 Schematic diagram of multi-section device structure.

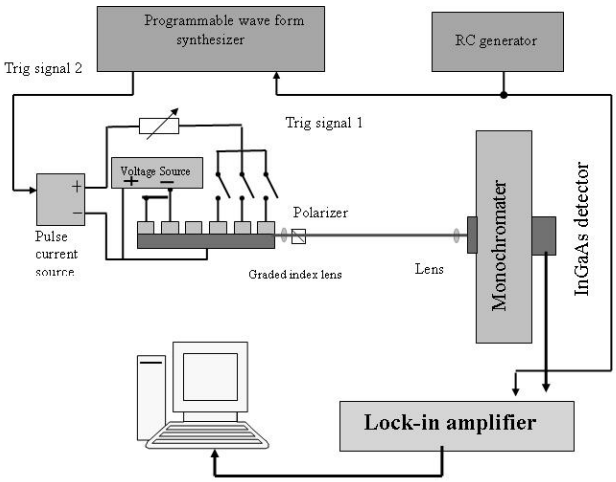

(a)

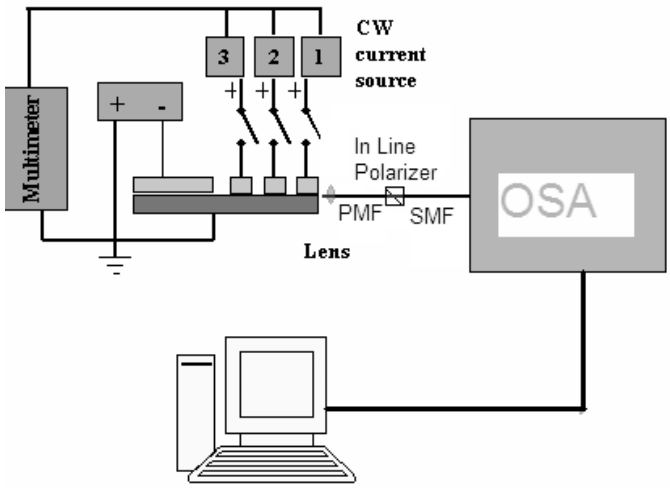

(b)

Figure 2-5 Test setup of the net modal gain and absorption measurement. (a) Free space coupling setup with monochromator for pulsed current pumping. (b) Fiber coupling setup with OSA for CW pumping. Both figures show configurations for gain measurement. In the case of absorption, the middle section would have a reverse bias voltage.

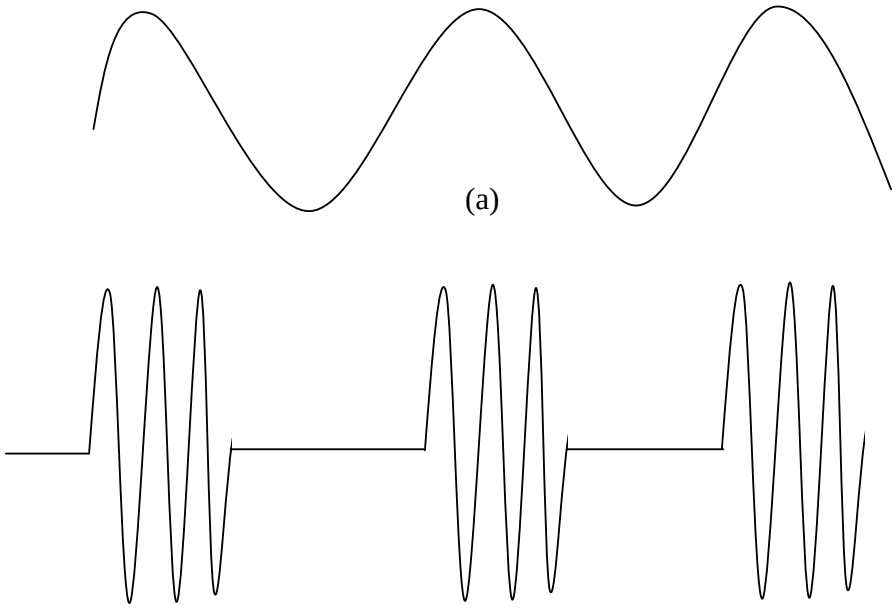

(a)

(b)

Figure 2-6 Schematic diagram of the sinewave signal generator and the programmable waveform synthesizer output signal (a) Output signal of RC generator: Trig signal 1 (b) Output signal of waveform synthesizer: Trigger signal 2.

2.4 Net Modal Gain and Absorption Of DWELL and QDASH

As shown in Figure 2-7, the ASE output from Zia414 using single, double, and triple-biased sections were measured under different current densities in the CW operation. A series of net modal gain spectra were obtained with Equation 2-11 from this ASE data and are shown in Figure 2-8.

Through the analysis of the net modal gain series, valuable information for the optimization of the QD lasers is obtained. Figure 2-9 and Figure 2-10 illustrates the evolution of the net modal gain at 1294 nm and the wavelength of the net modal gain peak versus the current density. The net modal gain saturates at 7.5 cm^{-1} when the current density reaches 1000 A/cm^2, a result attributed to the limited density of states available in this QD material. The gain saturation under pulsed operations occurs at a larger net gain value of about 15 cm^{-1}, as determined by the switch from ground state to excited state lasing in broad area lasers with different cavity length. This result shows the dramatic decrease in maximum gain that is possible in quantum dot devices due to heating under typical current densities of laser diodes. As the pump current density increases, the wavelength of the gain peak blue-shifts from 1306nm to 1291nm, presumably because the larger dots fill with carriers first. Also we can obtain the real gain data under different temperatures. As shown in the Figure 2-12, the maximum ground-state net modal gain is at 1286 nm with a value of 10 cm^{-1} under 15C. When the TEC temperature is increased to 25C, this peak red-shifts to 1294 nm and the maximum gain decreases to 7.5 cm^{-1}. Such data, which are under real working conditions, are valuable for device design optimization.

By measuring the ASE spectra and manipulating the data as decribed in Section 2.2.2, we obtained the absorption data for wafer Zia414. The various absorption spectra of the QD diode structure (obtained under CW operation for reverse biases ranging from 0V to -7V) are shown in Figure 2-11. It is noted that the absorption values at a given wavelength are significantly larger than the corresponding saturated gain [13]. In the range of wavelengths below the band edge of the material, the absorption does not vary with the wavelength indicating an internal loss value of 3 ± 0.5 cm^{-1}. This value is confirmed by the net gain spectra (Figure 2-8), which also converge to 3 ± 0.5 cm^{-1} for wavelengths greater than 1340 nm. Thus, the new segmented-contact method is efficient for extracting the internal loss of QD-based gain media.

Due to its ability to measure small gain and internal loss values accurately (see section below), the alternative segmented contact method has the ability to extract the gain and the absorption from a diode structure that does not exhibit lasing. This feature of the measurement is very useful for materials characterization, troubleshooting and low-signal, pulsed conditions. As an example, the 2-layer QDASH structure Run1809 had very low gain and did not show lasing during pulsed testing. Figure 2-13 shows the net modal gain spectrum of the QDASH structure measured with the alternative method under pulsed pump. The current density is 1000 A/cm^2, the pulse width 1μs, and the duty cycle 10%. The data are obtained using two different section configurations of 1.5-mm/section and 1.0-mm/section, which is the traditional test of consistency for the segmented-contact method.

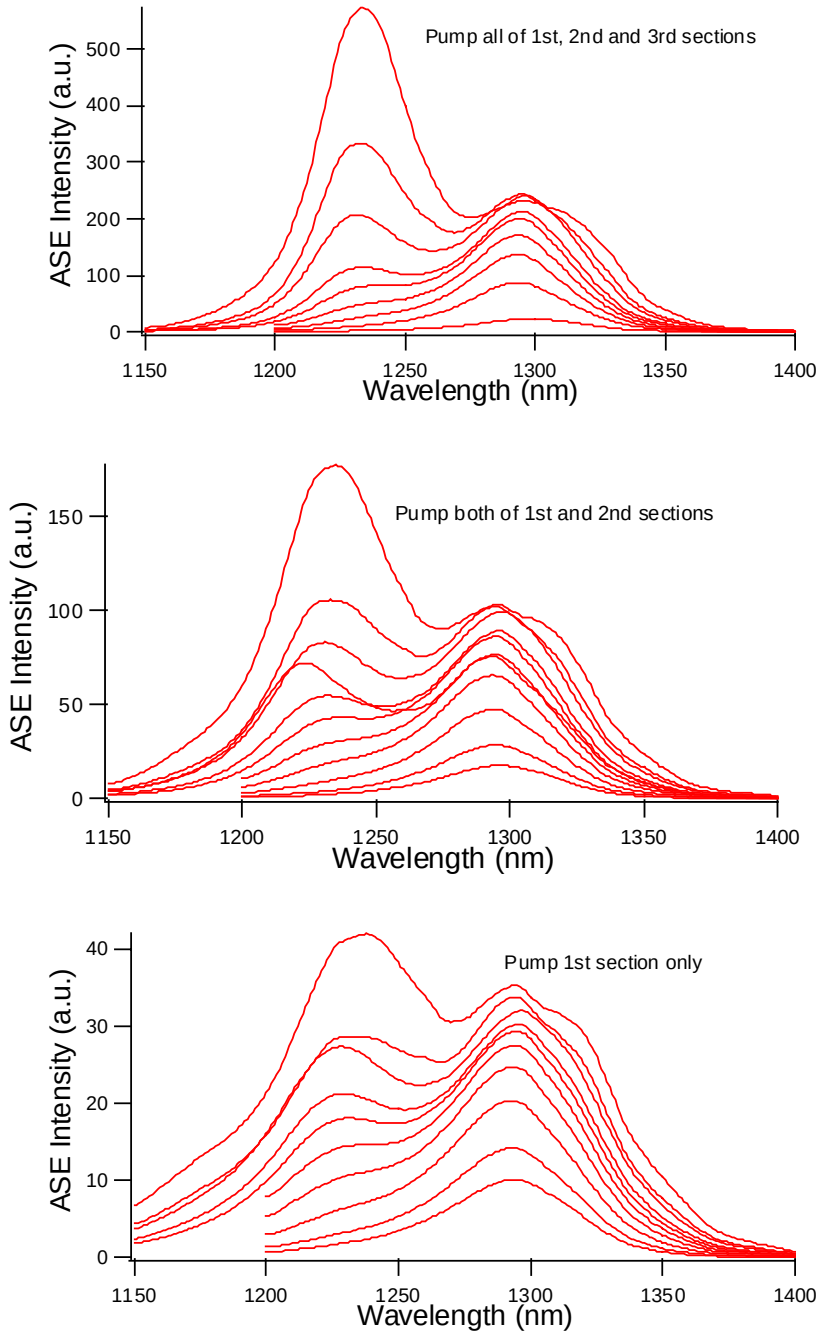

Figure 2-7 The spectra of amplified spontaneous emission with different injected CW current and pump sections. The temperature was set at 25 °C.

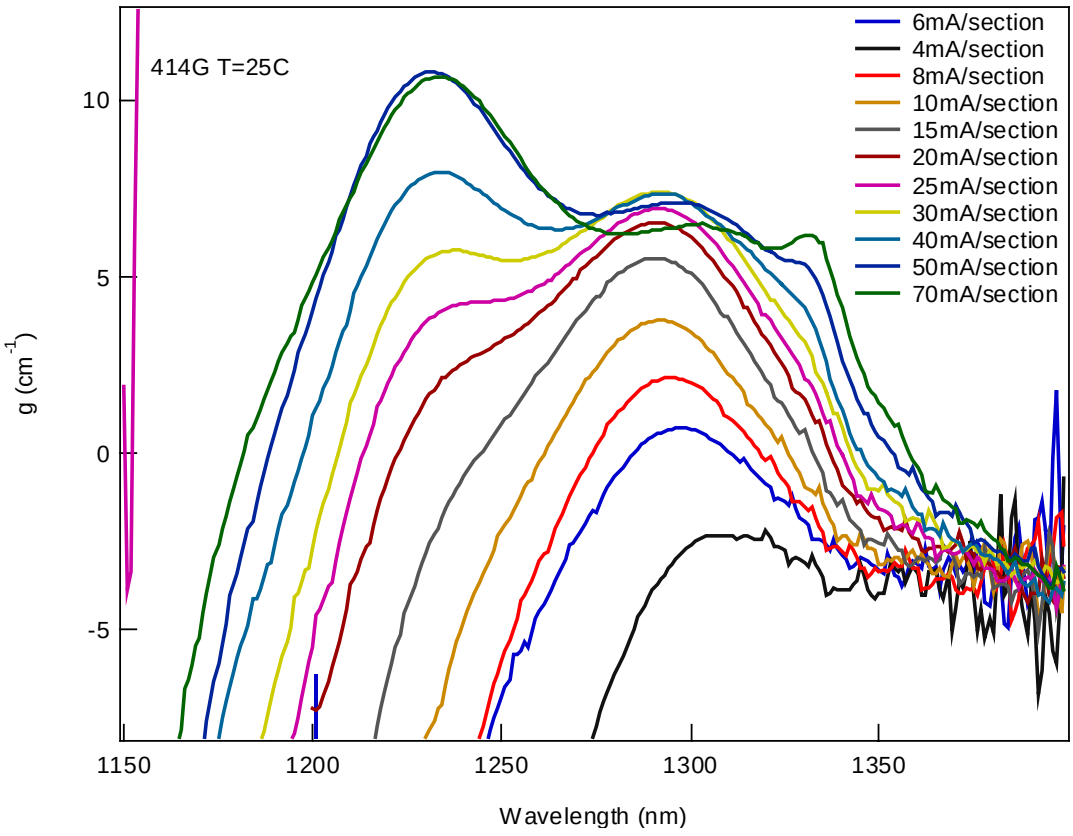

Figure 2-8 Net modal gain spectra of Zia414G with the improved segmented-contact method under CW pumping. The temperature was set at 25 °C.

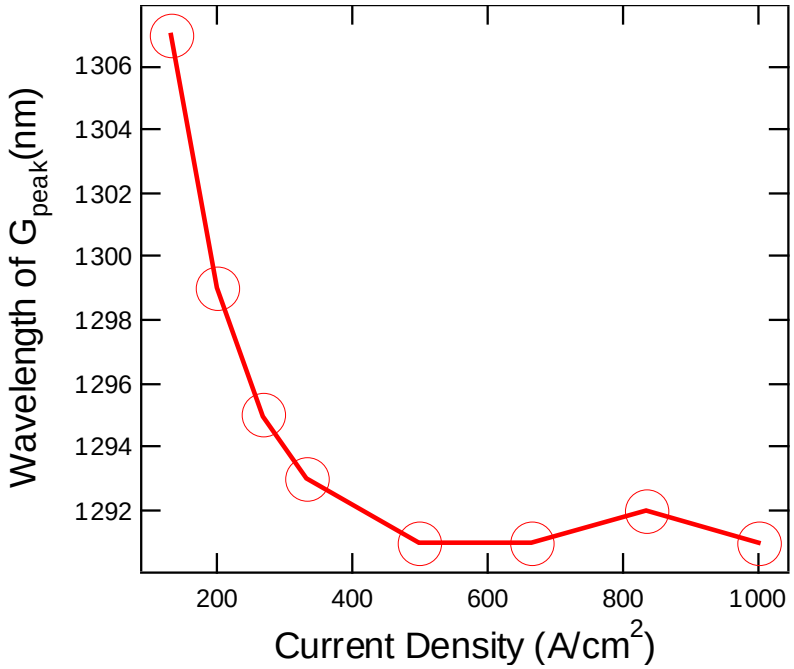

Figure 2-9 Evolution of the net modal gain peak wavelength versus the current density under CW pumping. The temperature was set at 25 °C.

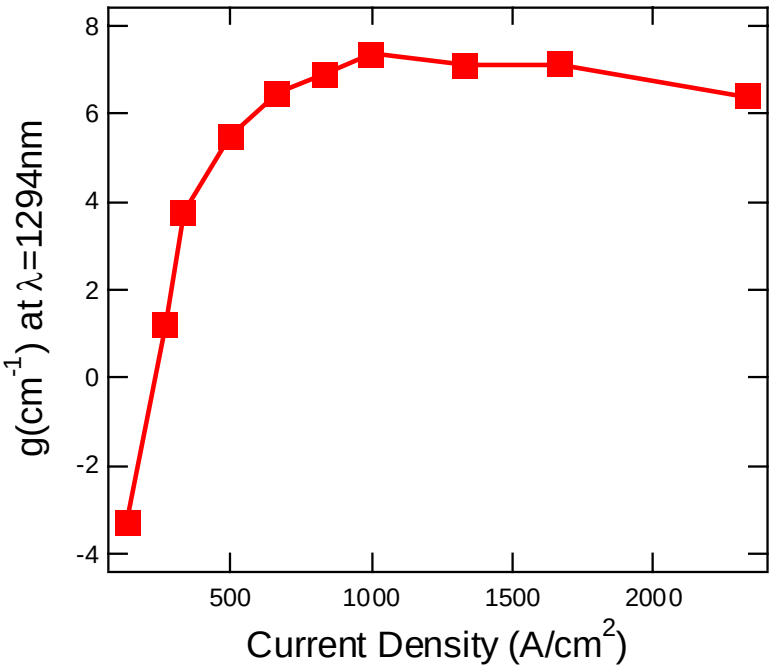

Figure 2-10 Evolution of the net modal gain at 1294 nm versus the current density at 25C.

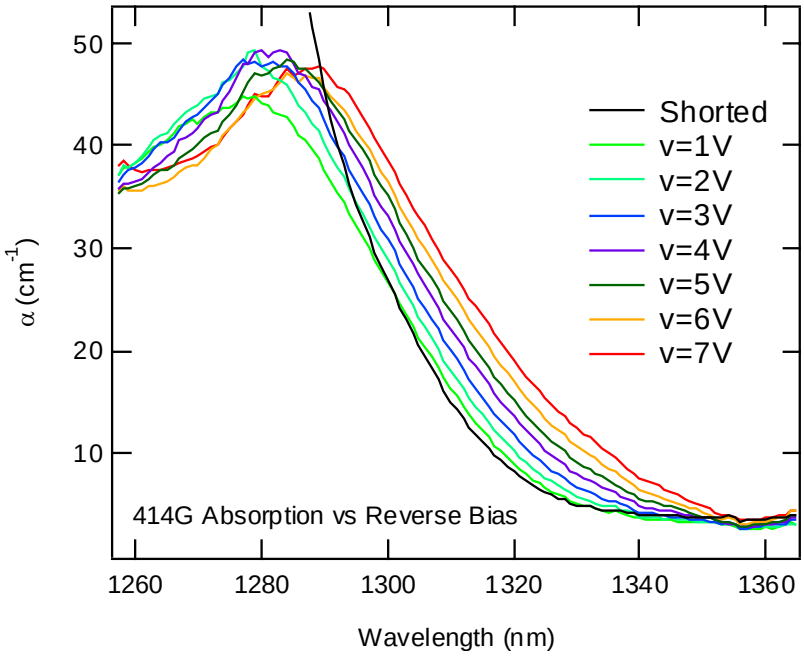

Figure 2-11 Modal absorption spectra under different reverse bias conditions under CW pumping. The temperature was set at 25 °C.

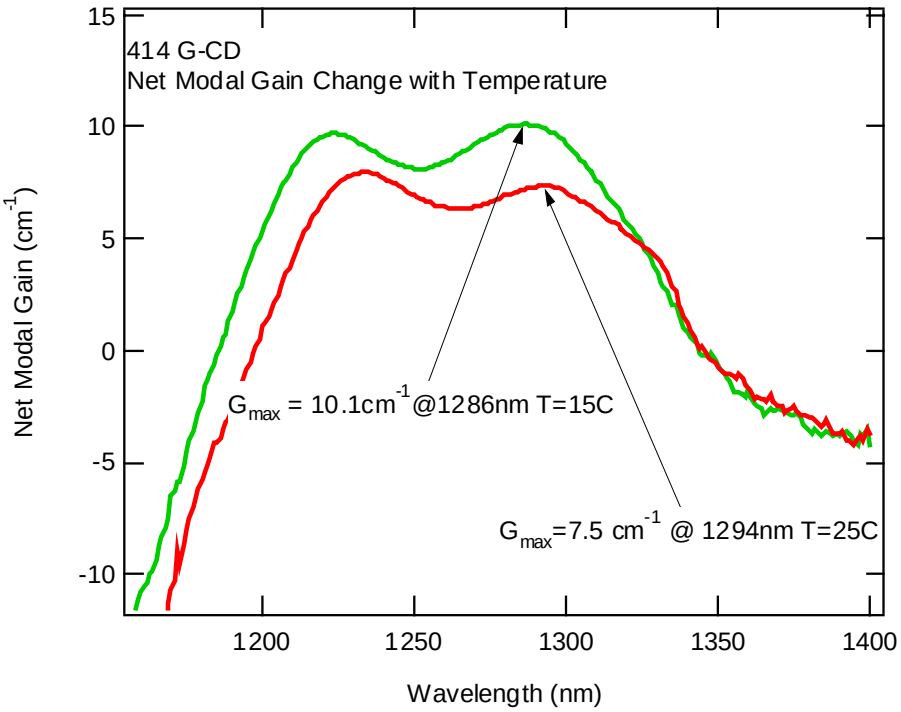

Figure 2-12 414 G Net Modal Gain under 15C and 25C under CW pumping.

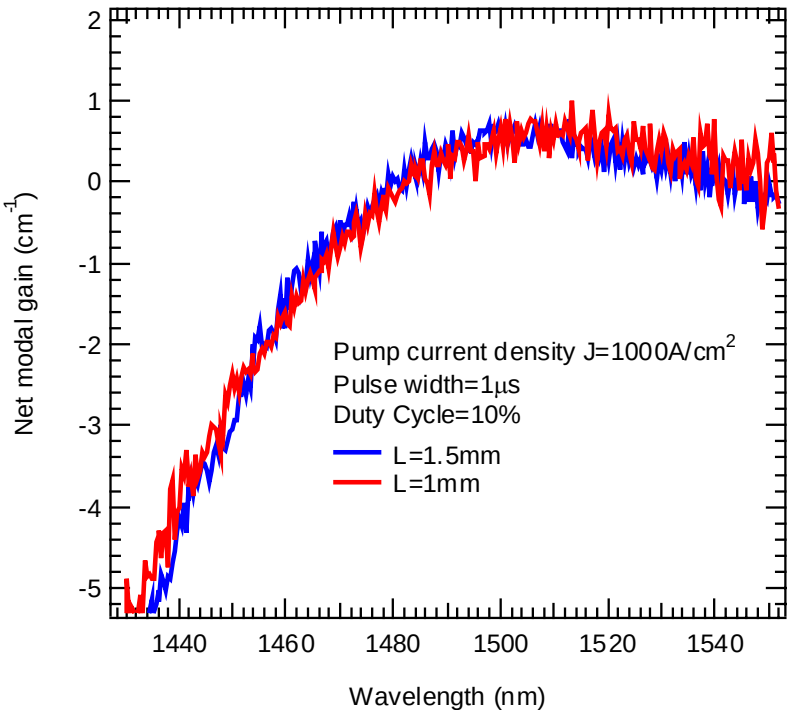

Figure 2-13 Net modal gain spectra of the QDASH structure with pulsed pumping. The solid line is data from the 1.5-mm section length configuration and the dashed line is from the 1-mm section configuration.

2.5 Accuracy Checking of the New Method

We used two conditions to check the accuracy of the improved segmented contact method: the linear gain assumption and the laser threshold data.

If the gain spectrum is accurate and the device works in the linear regime, the spectra from two different configurations should agree with each other. This method is suitable for the devices that do not operate as a laser. In Figure 2-13, the solid line is the net modal gain spectrum measured with the 1.5-mm/section device and the dashed line represents the1.0-mm/section device. The two separate measurements demonstrate a peak net modal gain of 0.7 cm^{-1} ± 0.2 cm^{-1} at a wavelength of 1510 nm and the agreement between the two curves is less than 0.3 cm^{-1} at the peak of the modal gain. The internal loss from the long-wavelength end of the net modal gain spectra is 2 cm^{-1} ± 1 cm^{-1}. The data of the 1.0-mm/section device is noisier than that from the 1.5 mm/section device because of a weaker ASE output.

There is alternative method for checking the accuracy of the net modal gain and absorption values. Since this method uses the same device without any change in the coupling conditions, it is called the self-calibration technique. The sole requirement is that the gain must be high enough to produce lasers since the comparison gain and absorption data is derived from the lasing condition. When all 16 sections are biased together with the same current, the device is equivalent to an 8-mm long ridge waveguide laser. At the laser threshold, the net modal gain equals the mirror loss, α_m. Assuming a cleaved-facet mirror reflectivity of 32%, the threshold current density and mirror loss can be used to calibrate the gain measurement at a single wavelength. It is found that the 8-mm QD laser emits at 1295 nm, has a corresponding threshold current density of 275

A/cm^2 and a mirror loss of 1.42 cm^{-1} as shown in the Figure 2-14. Under the same current density, the peak of the gain spectrum using the alternative segmented contact method is 1.45 cm^{-1} at 1295 nm. Accuracy within 0.1 cm^{-1} is achieved at a net modal gain lower than 2 cm^{-1}, as shown in Figure 2-15. The blue solid line is the net modal gain spectrum obtained with the improved segmented method and the gray line is with the conventional segmented method. With Figure 2-15, we can also find the significant accuracy improvement by the new measurement method. The conventional method has an inaccuracy of more than 1.8 cm^{-1} at a net modal gain lower than 2 cm^{-1}.

In order to verify the accuracy of the absorption spectra, a similar method is implemented using the data from a multi-section laser. When the 8-mm-long cavity is uniformly pumped with the exception of the second section, which is short-circuited to ground, the device lased at a wavelength of 1293 nm and the threshold current density is 666 A/cm^2, as illustrated by Figure 2-16.

At the threshold condition of the lower right corner of the hysteresis loop of Figure 2-17, the net modal gain in the optical cavity obeys the following expression:

$$g \cdot L_{active} = \alpha \cdot L_{absorb} + \alpha_m \cdot (L_{absorb} + L_{active}) \qquad \text{Eqn 2-15}$$

Of the total cavity length, L = 8-mm, L_{active} is 7-mm and L_{absorb} is 1-mm. The ASE spectra were measured at a current density of 666 A/cm^2 and the modal absorption and net modal gain spectra were calculated by equations (5) and (7). The results are shown in Figure 2-18 and Figure 2-19. From the net modal gain spectrum, g is found to be 6.3 cm^{-1} at 1293 nm. With this g value and equation (8), α is calculated to be 32.7 cm^{-1} and, for comparison, α is 33.4 cm^{-1} from the spectrum of absorption in Figure 2-19. This shows an error of less than 2%. This process can be repeated to find more calibration points by

applying different voltages to the absorption section that produce different lasing conditions.

2.6 Unamplified Electro-Spontaneous Spectra

From Equation 2-9 and assuming the I_{leak} is same for the different pumping configurations, the ASE intensity has a relation to the unamplified spontaneous intensity and the net modal gain as:

$$I_{2L} - I_L = \frac{S}{G}\left[\exp(G \cdot L) - 1\right]\exp(G \cdot L) \qquad \text{Eqn 2-16}$$

The unamplified spontaneous emission intensity S is related to the ASE intensity I_L, I_{2L} and the net modal gain G by:

$$S = G\frac{I_{2L} - I_L}{\left(\exp(G \cdot L) - 1\right)\exp(GL)} \qquad \text{Eqn 2-17}$$

In this improved segmented-contact method, an accurate spectrum of net modal gain G can be obtained and this allows us simply to obtain the unamplified spontaneous emission spectra without special processing and optical alignment. An example of unamplified spontaneous emission data as a function of wavelength calculated using Equation 2-17 appears in Figure 2-1.

2.7 Quantum Confined Stark Effect

To explore the electro-absorption effect further, the absorption spectra were measured under different reverse bias conditions by the method described above and shown in Figure 2-11. In Figure 2-11, the absorption spectra peak position red-shifts to a

smaller photon energy when the reverse bias voltage increases. The active region of the multilayer quantum dot laser structure wafer is about 140 nm. Assuming all reverse voltage was applied on the active region, the ground state absorption peak positions were plotted against the electric fields in Figure 2-21. The peak positions at different reverse bias can be described by a linear dependence approximately and the red-shift step is about 1.5meV/V at a reverse bias of |V|>1V, which deviates from the expected quadratic dependence. This result may be explained by the possibility that the electric field was large enough to begin dissociating the electron-hole pair and thus the transition energy was influenced [21, 22]. The Stark shift has amplitude of 9.8 meV under an electric field of 150 kV/cm and this is comparable with the measurement of an InAs QD on GaAs [23].

2.8 Conclusion

In this chapter, an alternative segmented contact method for net modal gain and absorption measurement was discussed. The new approach essentially subtracts background signals from the measurement and results in clean, accurate gain and absorption spectra using 3 biased sections instead of the conventional 2-section method. Experimental setups were described for CW and pulsed conditions demonstrating the flexibility and accuracy of the technique in a variety of pump and collection optics configurations. The gain and absorption spectra of QD and QDASH samples were highlighted as the alternative method is particularly useful for optical materials that have relatively low gain and absorption. A self-calibration method was introduced that takes advantage of laser data measured in the same optical cavity used in the multi-section technique. An accuracy of 0.2 cm^{-1} was obtained at nominal gain values below 2 cm^{-1}. The unamplified electro-spontaneous spectra were obtained with ASE spectra and net

modal gain spectra. The QCSE has been observed and the red shift has a linear dependence with reverse bias. This new technique is also a powerful tool for characterizing very low gain material samples that are difficult to characterize by other techniques.

This improved segmented contact gain-loss measuring technique will be used in mode-locking characterization, mode-locked lasers and SLED device design in the following chapters.

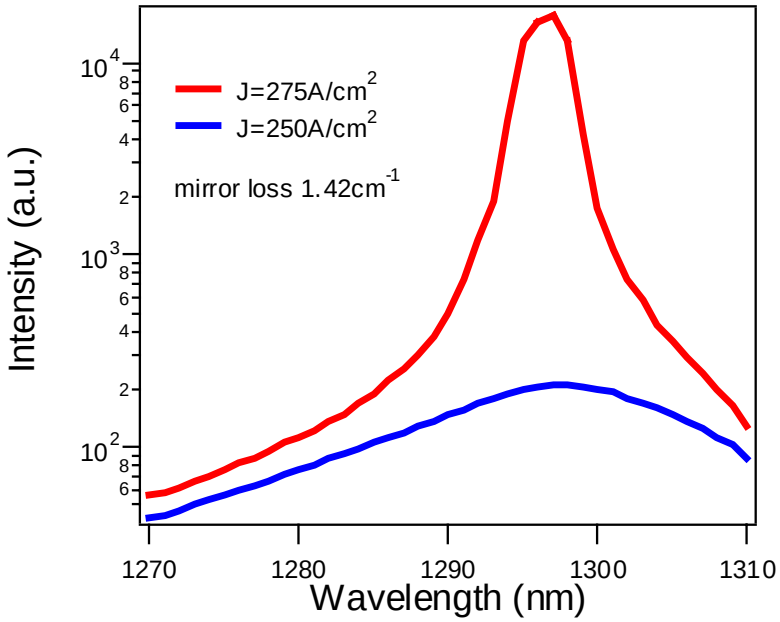

Figure 2-14 Spectra of Zia 414 when all sections are pumped uniformly. The red line is under an injected current density of 275 A/cm^2 and the blue line is under an injected current density of 250 A/cm^2.

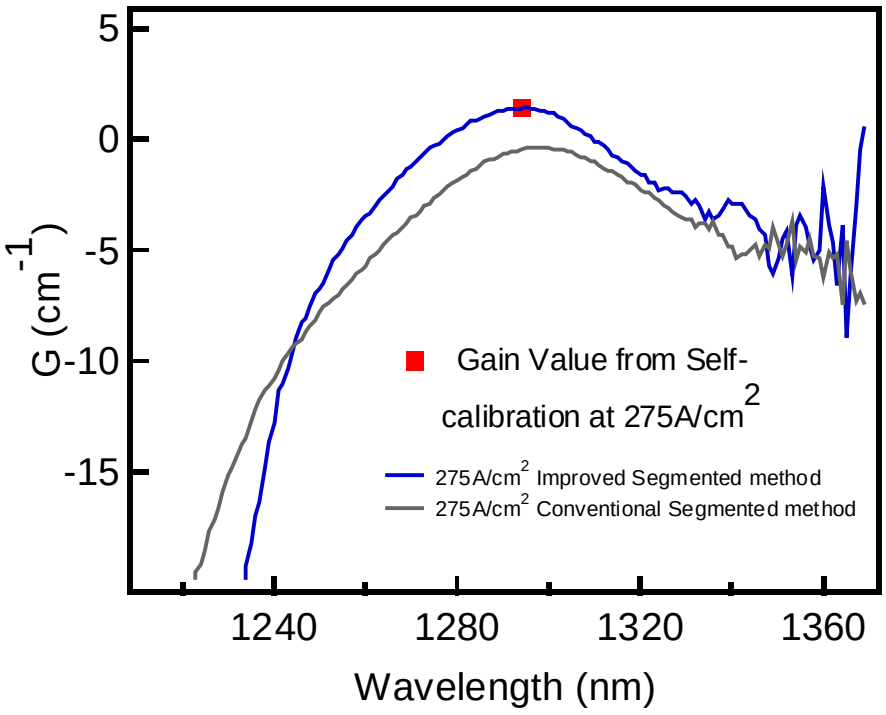

Figure 2-15 Net modal gain of Zia414 under pumping current density of 275A/cm^2. The blue solid line is the net modal gain spectrum obtained with the improved segmented method and the gray line is with the conventional segmented method.

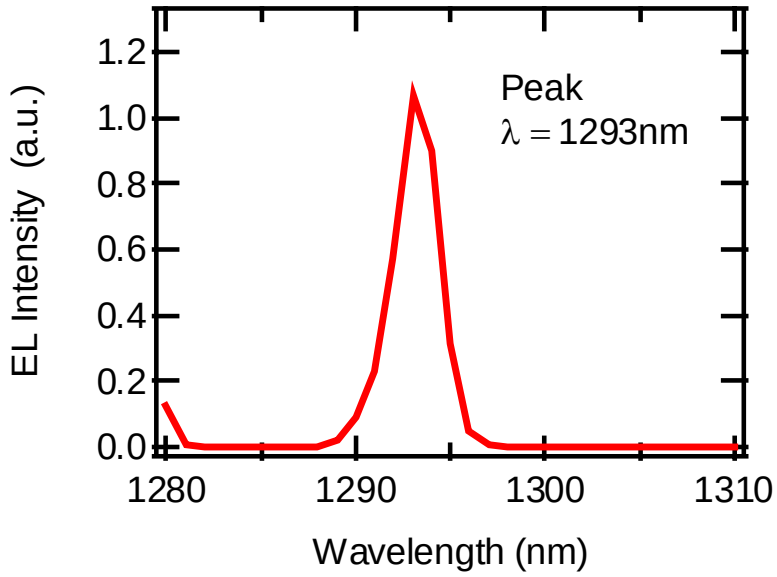

Figure 2-16. The spectrum of Zia414with second section grounded

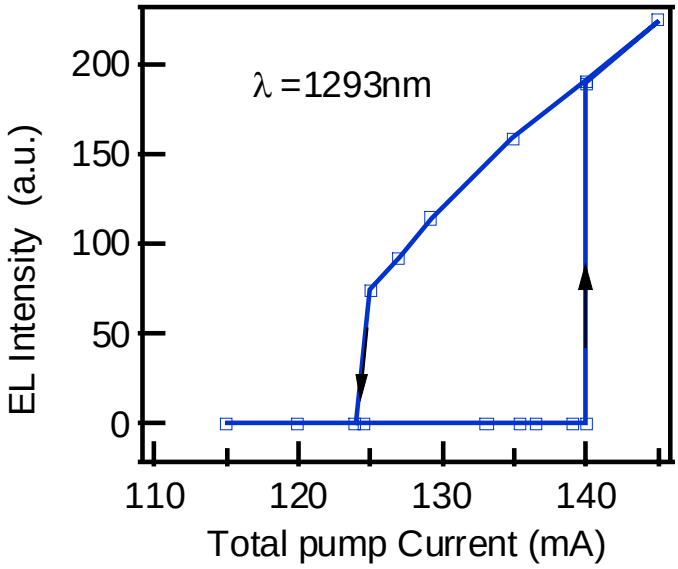

Figure 2-17. L-I curve of Zia414 with second section grounded.

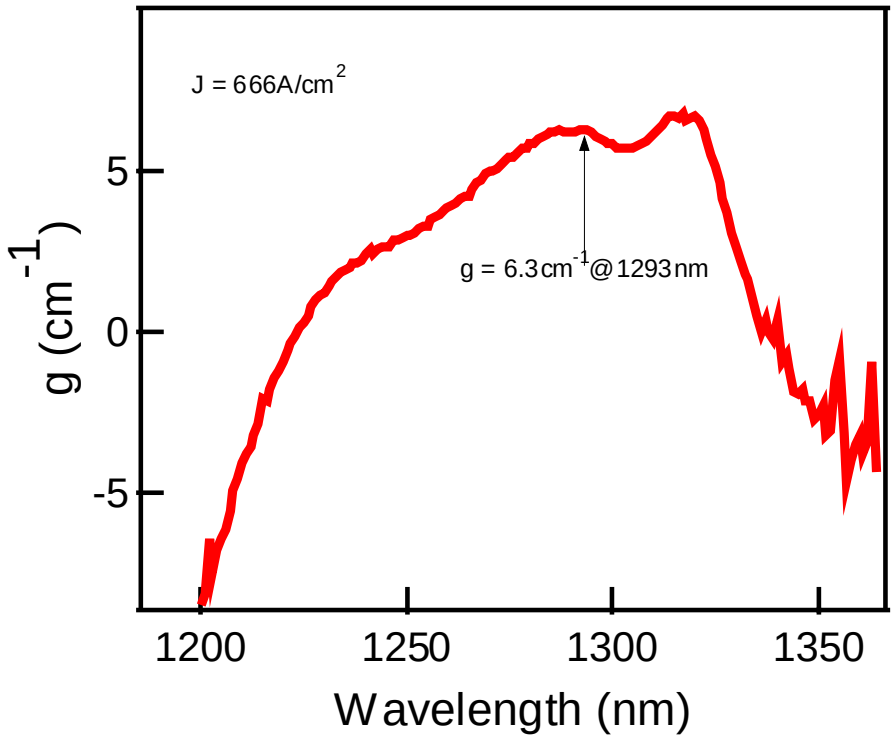

Figure 2-18 Net modal gain of Zia414 under injected current density of 666A/cm^2 (20mA/section). The net modal gain is to 6.3cm^{-1} at wavelength of 1293nm.

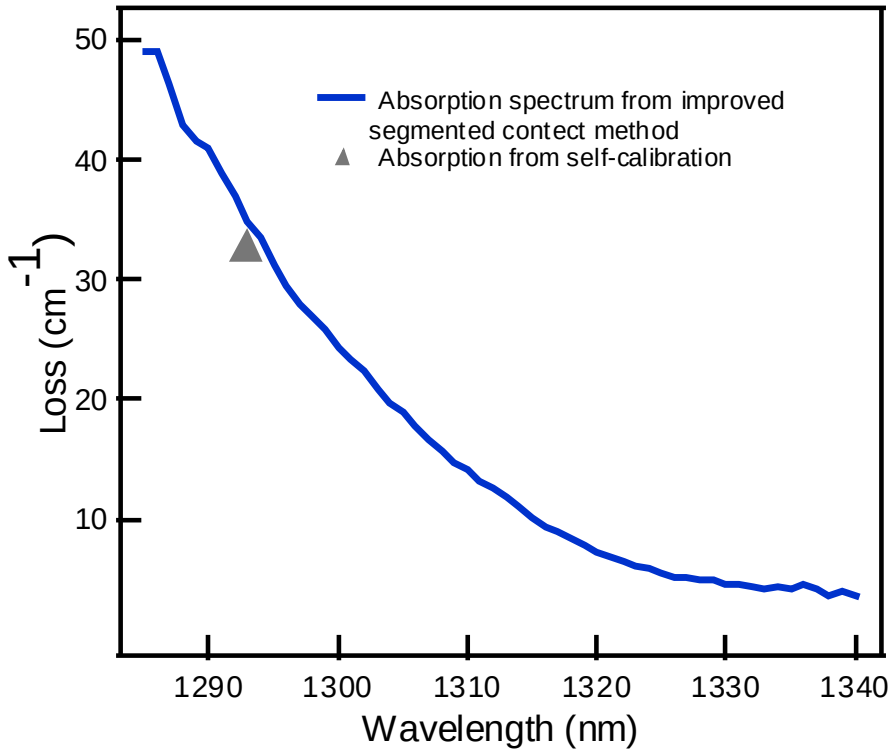

Figure 2-19. The absorption spectrum when the 2nd section was shorted and the absorption calibration value from the self-calibration.

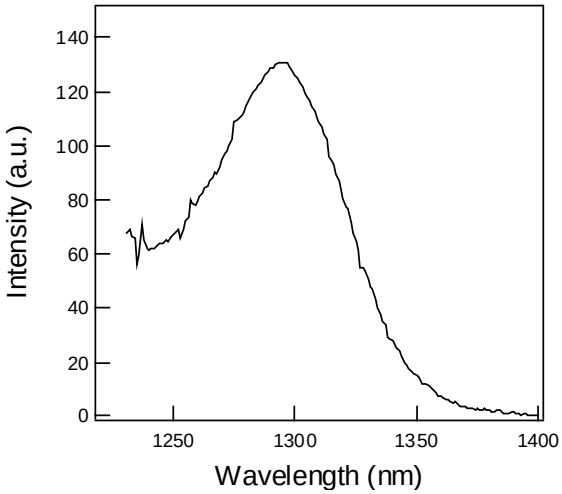

Figure 2-20 Unamplified electro-spontaneous emission spectrum under current density of 6mA/section

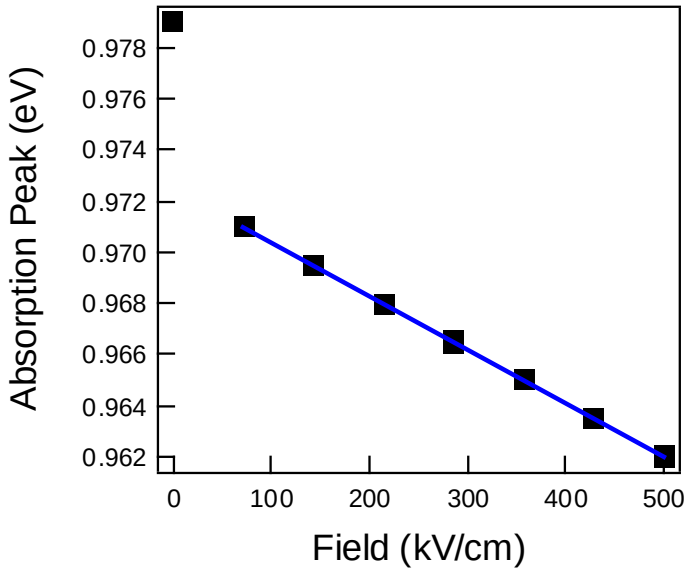

Figure 2-21 Modal absorption spectrum peak positions under different reverse bias conditions

2.9 References For Chapter 2

1 M. Asada, Y. Mityamoto, Y. Suematusu, " Gain and the threshold of 3-dimensional quantum-box lasers", IEEE J. Quantum Electron. 22, pp1915, 1986

2 K.J. Vahala, "Quantum Box Fabrication Tolerance and Size Limits in Semiconductors and Their Effect on Optical Gain," IEEE J. Quantum Electron. 24, pp523, 1988

3 N. Kirstaedter, O.G. Schmidt, N.N. Ledentsov, D. Bimberg, V.M. Ustinov, A.Y. Egorov, A.E. Zhukov, M.V. Maximov, P.S. Kopev, Z.I. Alferov, "Gain and differential gain of single layer InAs/GaAs quantum dot injection lasers," Appl. Phys. Lett. 69, 1226-1228, 1996

4 M. Grundmann and D. Bimberg, "Gain and threshold of quantum dot lasers: Theory and comparison to experiments," Japan. J. Appl. Phys. v.36, pp4181, 1997

5 H. Jiang and J. Singh, "Nonequilibrium distribution in quantum dot lasers and influence on laser spectral output," J. Appl. Phys. v.85, pp7438, 1999

6 P. M. Smowton, E. Herrmann, Y. Ning, H. D. Summers, and P. Blood, “Optical mode loss and gain of multiple-layer quantum-dot lasers”, Applied Physics Letters v.78, (18) pp2629, April 2001

7 P.M Smowton, P. Blood, “On the determination of internal optical mode loss of semiconductor lasers”, Applied Physics Letters, v. 70(18) pp. 2365, May 5, 1997

8 Piprek J, Abraham P, Bowers JE, “Carrier nonuniformity effects on the internal efficiency of multiquantum-well laser”, Applied Physics Letters, v. 74(4) pp. 489, Jan. 25, 1999

9 B. W. Hakki and T. L. Paoli, “CW degradation at 300°K of GaAs double-heterostructure junction lasers. II. Electronic gain”J. Appl. Phys. 44, 4113 (1973)

10 Oster, A., Erbert, G., and Wenzel, H., "Gain spectra measurements by a variable stripe length method with current injection," *Electronics Letters*, vol. 33, no. 10, pp. 864-866, 1997.

11 J. D. Thomson, H. D. Summers, P. J. Hulyer, P. M. Smowton, and P. Blood, "Determination of single-pass optical gain and internal loss using a multisection device," *Applied Physics Letters* **75**, 2527-2529, 1999

12 Smowton, P. M., Herrmann, E., Ning, Y., Summers, H. D., Blood, P., and Hopkinson, M., "Optical mode loss and gain of multiple-layer quantum-dot lasers," *Applied Physics Letters*, vol. 78, no. 18, pp. 2629-2631, 2001.

13 P. Blood, G. M. Lewis, P. M. Smowton, H. Summers, J. Thomson, and J. Lutti, "Characterization of semiconductor laser gain media by the segmented contact method," *IEEE Journal of Selected Topics in Quantum Electronics* **9**, 1275-1282, 2003.

14 Abraham NB, Huang JC, Kranz DA, Rockower EB, “Amplified-Spontaneous-Emission Intensity Fluctuations”, Physical Review A , v. 24(5) pp. 2556 1981

15 Joseph T.Verdeyen, *Laser Electronics*, 1995

16 Oster, A; Erbert, G; Wenzel, H, "Gain spectra measurements by a variable stripe length method with current injection", *Electronics Letters* **33**, 864-866, 1997

17 Xin, Y. C., Li, Y., Martinez, A., Rotter, T. J., Su, H., Zhang, L., Gray, A. L., Luong, S., Sun, K., Zou, Z., Zilko, J., Varangis, P. M., and Lester, L. F., "Optical gain and

absorption of quantum dots measured using an alternative segmented contact method," *IEEE Journal of Quantum Electronics*, vol. 42, no. 7-8, pp. 725-732, 2006.

18 L. F. Lester, A. Stintz, H. Li, T. C. Newell, E. A. Pease, B. A. Fuchs, and K. J. Malloy, "Optical characteristics of 1.24-mu m InAs quantum-dot laser diodes," *IEEE Photonics Technology Letters* **11**, 931-933 1999.

19 G. T. Liu, A. Stintz, H. Li, T. C. Newell, A. L. Gray, P. M. Varangis, K. J. Malloy, and L. F. Lester, "The influence of quantum-well composition on the performance of quantum dot lasers using InAs/InGaAs dots-in-a-well (DWELL) structures," *IEEE J. Quantum Electron.* **36**, 1272-1279, 2000.

20 Stintz, A., Rotter, T. J., and Malloy, K. J., "Formation of quantum wires and quantum dots on buffer layers grown on InP substrates," Journal of Crystal Growth, vol. 255, no. 3-4, pp. 266-272, 2003

21 G. W. Wen, J. Y. Lin, H. X. Jiang, and Z. Zhen, "Quantum-confined Stark effects in semiconductor quantum dots" *Phys. Rev. B*, **52**, 5913–5922, 1995.

22 X. D. Huang, A. Stintz, H. Li, A. Rice, G. T. Liu, L. F. Lester, J. Cheng, and K. J. Malloy, "Bistable operation of a two-section 1.3-mu m InAs quantum dot laser - Absorption saturation and the quantum confined Stark effect," *IEEE Journal of Quantum Electronics* **37**, 414-417, 2001

23 P. W. Fry, I. E. Itskevich, D. J. Mowbray, M. S. Skolnick, J. J. Finley, J. A. Barker, E. P. O'Reilly, L. R. Wilson, I. A. Larkin, P. A. Maksym, M. Hopkinson, M. Al Khafaji, J. P.

R. David, A. G. Cullis, G. Hill, and J. C. Clark, "Inverted electron-hole alignment in InAs-GaAs self-assembled quantum dots," *Physical Review Letters* **84**, 733-736, 2000

Chapter 3 Quantum Dot Monolithic Multi-Section Passively Mode-Locked Lasers

3.1 Introduction

As the speed of microprocessors using electrical clock distribution increases beyond 3.6 GHz, the challenges and limitations of copper-based metal interconnects become more apparent. With the silicon CMOS feature size shrinking from today's state-of-the-art of 90 nm to 32 nm and beyond, speed bottlenecks due to RC delays on chip and increasing electrical power consumption are expected to become serious problems [1, 2]. These problems can be avoided by the use of optical interconnects for clock distribution.

The compact size, low cost, low power consumption, and direct electrical pumping of semiconductor monolithic mode-locked lasers make them promising candidates for inter-chip/intra-chip clock distribution [3, 4] as well as other applications including high bit-rate optical time division multiplexing [5, 6, 7, 8, 9], high speed electro-optic sampling [10], and impulse response measurement of optical components [2]. However, the compact diode laser pulse sources have generally not been able to match the pulse quality of the best mode-locked lasers [11]: they suffer from longer pulse durations, impaired stability, asymmetric pulses, chirped spectra and compromised peak power. For improving the characteristic of semiconductor mode-locked lasers, research on both physics and devices are necessary.

Development of quantum dot (QD) lasers with 1.3-μm emission wavelength showing very low threshold current [12, 13], large T_0 [14], and suppressed beam filamentation [15], presents a breakthrough towards optoelectronic applications. Some unique

characteristics of QD lasers, such as ultrabroad bandwidth, ultrafast gain dynamics, easily saturated absorption, strong inversion, low alpha parameter and wide gain bandwidth, make them an ideal choice for semiconductor monolithic mode-locked lasers [16, 17, 18, 19]. Also the 1.25 μm emission wavelength, which is transparent to Si waveguides and detectable by SiGe photodetectors, makes the InAs QD mode-locked lasers suitable for Si-based optoelectronic integrated-circuits [20, 21].

In this chapter, a brief introduction of the mutual saturation mode-locking [22] is given in Section 3.2. The device structure and measurement setup are described in Section 3.3. In Section 3.4, the relationship between the 2-section SCPM laser operation characteristics and the QD material parameters is studied, and the solution of the master equation of mode-locking with a fast saturable absorber is verified. In Section 3.5, we present experimental results of novel multi-section monolithic passive mode-locked lasers that emit near 1.3 μm using QDs as the active region on the GaAs substrate. The multi-section configurations containing an absorber, a gain section, and a passive section (AGP) significantly increase the peak pulsed power (> 45%) and decrease the pulse width (>35%) of the QD mode-locked lasers compared with conventional 2-section devices consisting of only gain and absorber regions. The multi-section geometry also allows setting the absorber position to form the gain-absorber-gain (GAG) structure within the same optical cavity to achieve complete harmonic mode-locking up to the 7^{th} harmonic and incomplete locking as high as the 15^{th} harmonic.

3.2 Colliding Pulse Mode-Locking and Self-Colliding Pulse Mode-Locking Lasers

The passive InAs QD mode-locked lasers that are studied in this chapter are based on mutual saturation mode-locking concept [22], which is also known as colliding pulse mode-locking (CPM) [23]. A schematic plot of a monolithic passive CPM laser is shown in the Figure 3-1(a) [24]. There is only DC current to drive the laser, and no external RF modulation is used. When two counter-propagating pulses do "collide" in the saturable absorber, they will mutually saturate the absorber and produce a much stronger saturation than if the two pulses arrive in sequence. Figure 3-2 shows the computed pulse propagation in the laser cavity for a single round trip in steady state [24]. Before the arrival of the optical pulse, the loss and gain values are at their small signal values, and the small signal loss is a little higher than the small signal net modal gain. In a passive mode-locking laser, to generate optical pulses, the loss has to saturate faster than the gain, which is the stability condition of a passively mode-locked laser:

$$s = \frac{E_{sat,g}}{E_{sat,abs}} = \frac{h\nu A_m / \Gamma\, dg/dN}{n_{tr} h\nu A_m} = \frac{1}{n_{tr}\Gamma \dfrac{dg}{dN}} > 1 \qquad \text{Eqn 3-1}$$

Where $E_{sat,\,abs}$ is the saturation energy of the absorber, and $E_{sat,g}$ is the saturation energy for the gain section. A_m is the mode cross-sectional area, h is Planck's constant, ν is the optical frequency, n_{tr} is the transparency density, Γ is the confinement factor and dg/dN is the differential gain with respect to carrier density. The s is defined as the stability parameter [25]. For stable passive mode-locking, the s should be greater than 1, which

means a small differential gain, confinement factor and dot density are helpful for stable CPM operation.

A saturable absorber is called a slow absorber if its recovery time is much longer compared to the duration of pulses produced in the laser. Otherwise, the absorber is called a fast absorber [26, 27]. Figure 3-3 shows the pulse generation with the gain and loss saturation and recovery in a passive mode-locked laser with (a) a slow absorber and (b) a fast absorber [28].

The self-colliding pulse mode-locking (SCPM) is also based on the mutual saturation. A SCPM laser is like cutting a CPM laser from the center except that for the same cavity length the CPM device has twice the repetition rate of the SCPM laser. The absorber is located next to a high reflection (HR)-coated mirror where the optical pulse collides with itself in the saturable absorber for pulse narrowing. The schematic plot of a monolithic self-colliding pulse mode-locked laser is shown in Figure 3-1(b). The time between the arrival of consecutive pulses in SCPM is equal to the cavity round-trip time:

$$T_R = \frac{2Ln}{c}$$
$$f = \frac{1}{T_R} \qquad \text{Eqn 3-2}$$

where L is the cavity length and n is the group index. The corresponding repetition rate f for a practical mode-locked laser is on the order of 1 GHz to100GHz [14].

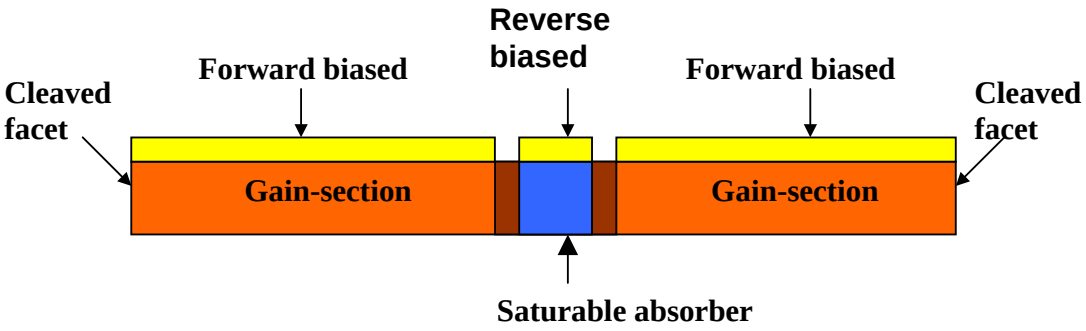

(a)

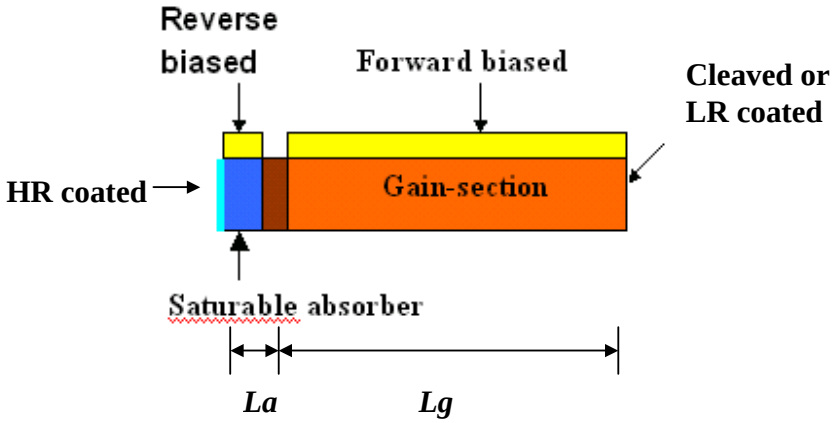

(b)

Figure 3-1 (a) Schematic plot of a monolithic CPM laser [24]. (b) Schematic plot of a monolithic SCPM laser.

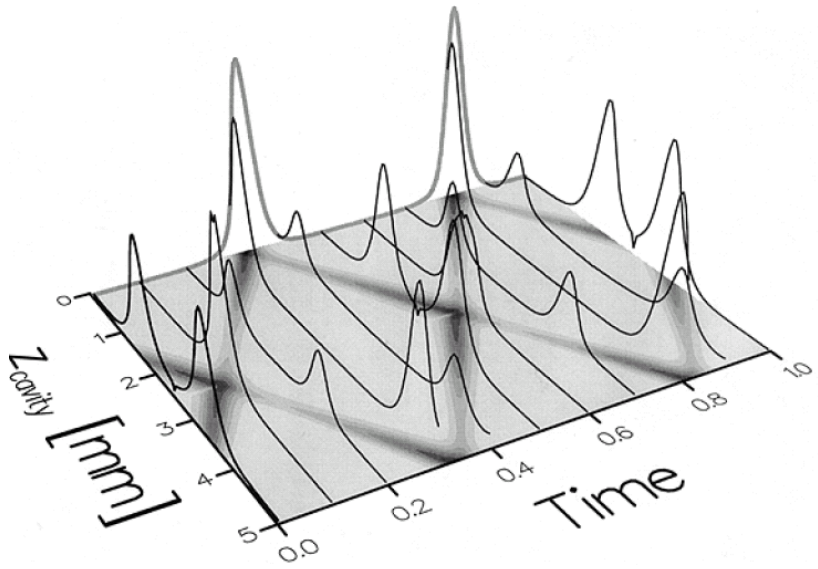

Figure 3-2. The pulse propagation in the laser cavity for a single round trip, when steady state is reached. [24]

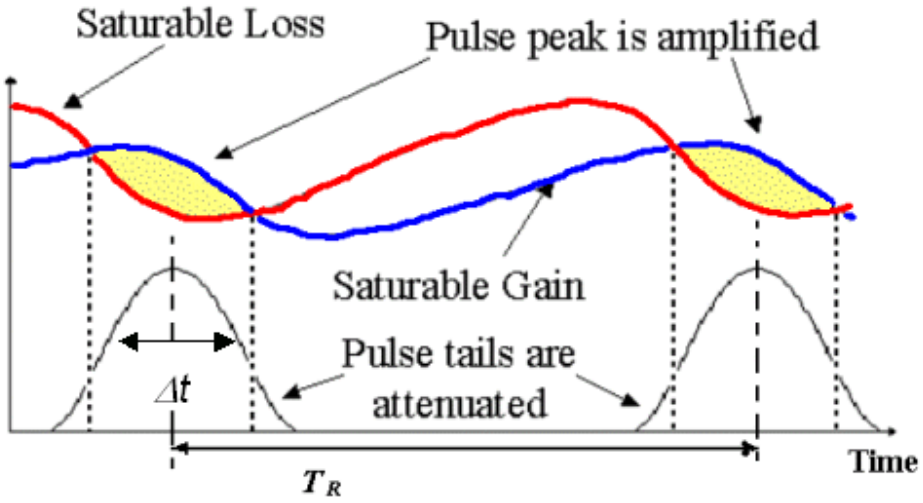

(a)

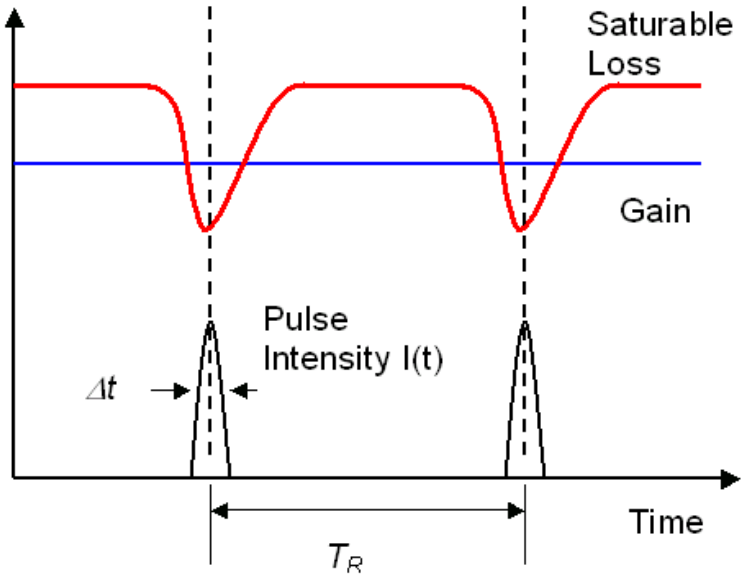

(b)

Figure 3-3 Passive mode-locking with a (a) slow saturable absorber and (b) fast saturable absorber [28].

3.3 Devices and Measurement Setup

3.3.1 Device structure and fabrication

The laser epitaxial structure consists of a 6-stack "Dots-in-a-WELL" (DWELL) active region grown by solid source molecular beam epitaxy (MBE) on a (001) GaAs substrate with a photoluminescence (PL) peak emission wavelength of 1.25 μm [29, 30]. The details of the MBE growth parameters and the device processing are described elsewhere [31]. The structure is similar to the un-doped QD material described in Chapter 2.

The multi-section device structure provides a flexible layout and is used to study mode-locked lasers for both the physics modeling and devices characterization [32, 33]. In our experiments, the devices are segmented ridge-waveguide lasers with a ridge width of 3 μm, and are fabricated according to the standard multi-section device processing [34]. After the standard ridge laser processing, the sample is cleaved to form devices consisting of 16 sections (for a cavity length of 8 mm) or 11 sections (for a cavity length of 5.5 mm). One cleaved facet was HR-coated (R≈95%) and the other facet was low reflection (LR)-coated (R≈15%). The 0.5-mm sections were wire-bonded or probed to provide the desired experimental configurations that are described below. The devices were mounted on copper heatsinks, and for all the results presented in this chapter, the measurements were performed at a controlled substrate temperature of 20^{o}C if not specified.

3.3.2 The mode-locked laser measurement setup

The operational characteristics of mode-locked lasers include the repetition rate, the optical pulse width, the optical spectrum, the peak power, the timing jitter, the transparency current density, and the threshold current. The characteristics of basic QD lasers include the net modal gain, the absorption, the internal loss, and the saturation power of absorption. An experimental setup has been built that can measure all these data from one single device.

The test setup includes two main blocks: an electrical-pumping block, and a signal-detection block, as shown in Figure 3-4(a). A 16-channel laser diode controller (ILX Lightwave LDC-3916) was used as the current source. A 16-probe card was used to distribute the injection current from each channel to different sections on the multi-section device as shown in Figure 3-4(b). By controlling the 16-channel current source output, we can pump every section on the multi-section device individually. A multi-meter was used to monitor the total injection current. A DC power source was used to apply reverse bias on the absorber. An integrated optical head mounted on a 5-axis precision linear stage was used to collect the output emission of the mode-locked laser. The integrated optical head consists of a polarization-maintaining fiber (PMF) pigtail, a collection lens, and an isolator. The lens focuses the output light into the PMF through the isolator, which is used to avoid interference effects. The collected emission is fed into the autocorrelator (Femtochrome FR-103XL Autocorrelator described in the Appendix) to measure the pulse width, and the optical spectrum analyzer (Agilent 86142B OSA) to measure the optical spectra through fiber couplers. The repetition rate and timing jitter are measured by the spectrum analyzers (HP 8563E ESA). An inline-polarizer was

inserted between the optical head and OSA when measuring the net modal gain and absorption spectra as described in Chapter 2. The light-current (L-I) characteristics can be obtained if the optical head is replaced with an integrating sphere and photodetector. Therefore, we can obtain the multi-section mode-locked laser pulse repetition rate, the optical pulse width, the optical spectrum, the average and peak power, the timing jitter, the threshold current, the modal gain and loss spectra, the transparency current density, the internal loss, and the group refractive index with one single multi-section mode-locked laser device.

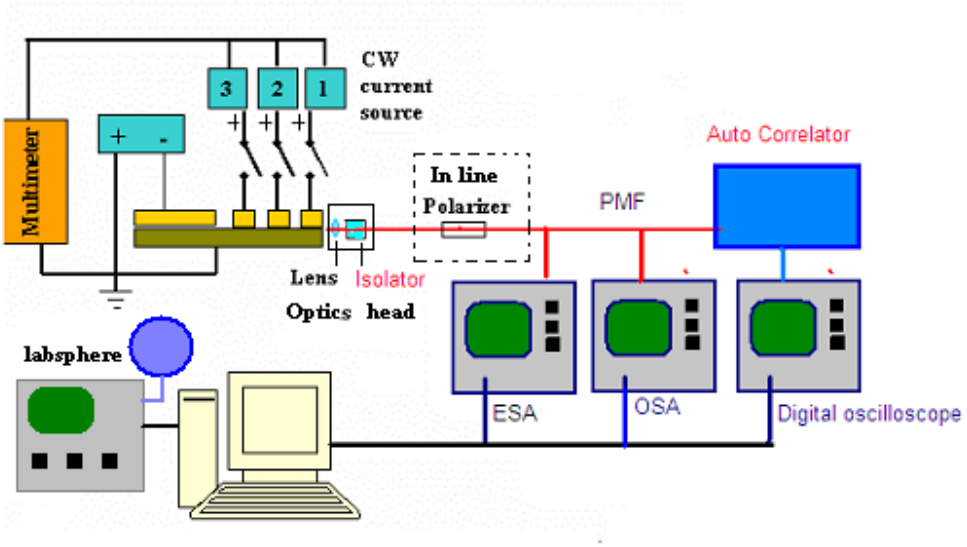

(a)

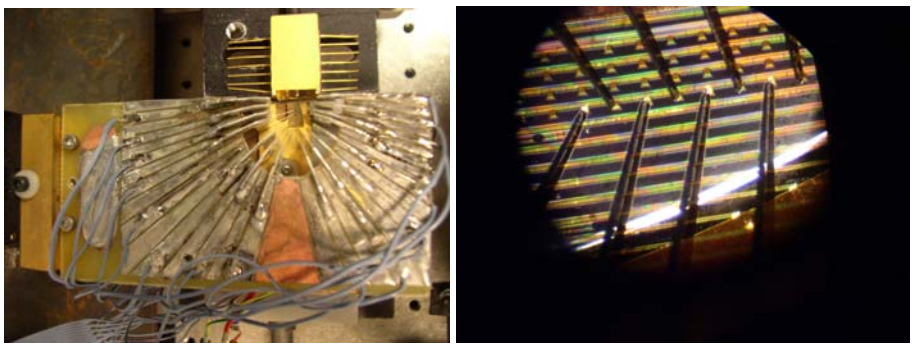

(b)

Figure 3-4. (a) Schematic diagram of the mode-locked laser measurement setup. (b) Multi-section device with probe card.

3.4 Two-Section QD Passive Mode-Locking Laser Characteristics and Master Equation

3.4.1 Two-section QD passive mode-locking laser characteristics

The 16-section device Zia792F-AF was fabricated from wafer #Zia792F. The unit length from section #2 to #15 is 0.5mm/section. However, section #1 and #16 were cleaved to be 0.3 mm and 0.7 mm, respectively. The total length of the gain section (L_g) is 6.8mm and the length of the absorber (L_a) is 1.2mm. The cleaved facet near section 16 was HR-coated (R=95%), and the other facet was AR-coated (R=15%). We configured the 16-section device for different measurements by changing the bias functions through the probe card. Sections #10 to #16 were reverse biased to form a 3.5-mm absorber, and sections #1 through #3 were pumped individually during the net modal gain and loss measurements. To make the same device operate as a two-section SCPM laser sections #15 and #16 were biased together with a reverse voltage, working as the saturable absorber, and meanwhile all the other sections were pumped uniformly to form one gain section.

We obtained accurate net modal gain and loss spectra using the improved segmented contact method, as shown in Figure 3-5. From the net modal gain spectra, we obtained the information on how the net modal gain changes as a function of emission wavelength and current density. Figure 3-9 shows the net modal gain of 1213 nm under different pump current densities. The transparency current density of a certain wavelength can also read from the net modal gain spectra. From the loss spectra at long wavelength, an internal loss of the ridge waveguide of 2cm^{-1} is found.

With the 2-section mode-locked laser configuration, we measured the operational characteristics from the same waveguide under different absorber bias voltages and gain currents. The L-I characteristics near the threshold of 2-section mode-locked laser with the absorber biased from –1V to –5V are shown in Figure 3-6. Figure 3-7 shows other characteristics under an absorber bias of –5V. An average power of up to 30 mW at gain current of 168 mA and a high/low threshold current of the 91mA/87mA due to bistability can be read from the CW L-I characteristics shown in Figure 3-7 (a). Under a gain current of 136 mA, the CW optical spectrum has a peak wavelength of 1224 nm and bandwidth of 5.2 nm; the autocorrelation signal exhibits a pulse width of 11.6 ps at a repetition rate of 5.17 GHz. The series curves of FWHM pulse width vs. gain current under absorber bias of –1V to –5V are shown in Figure 3-8 (a). The pulse width increases with increasing gain current or decreasing absorber bias voltage. With the data of FWHM pulse width and the L-I curve, the peak powers can be calculated with $P_{peak} = P_{average} / (f \cdot \Delta t)$, where Δt is the FWHM pulse width, and is shown in Figure 3-11. The peak power decreases with decreasing absorber bias voltage, which means the pulse width broadens faster than the average power increases with lower absorber bias voltage. A maximum peak pulsed power of approximately 410 mW is achieved at the laser facet under an absorber bias of –5V and a gain current of 88 mA that is near the threshold. Therefore, the characteristics of the 2-section mode-locked laser that is configured from the multi-section device are similar to a normal QD passive mode-locked laser.

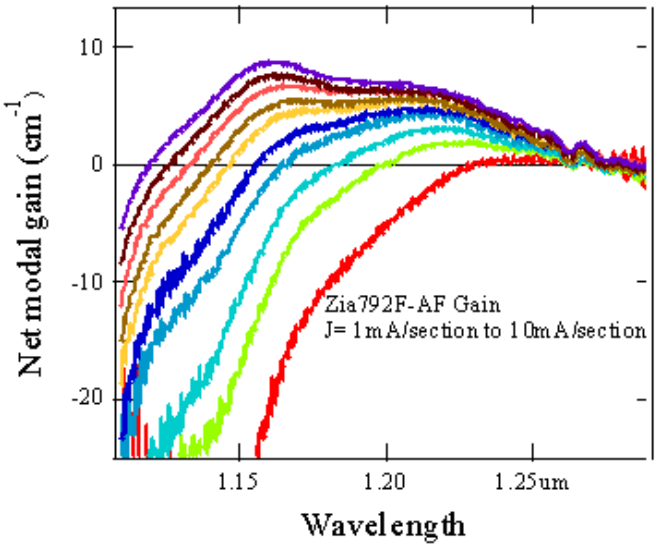

(a)

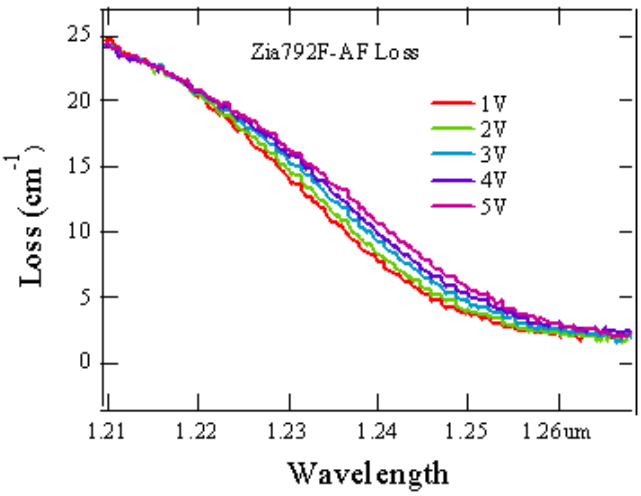

(b)

Figure 3-5. (a) Net modal gain and (b) Loss spectra of Zia792F-AF 16-section device.

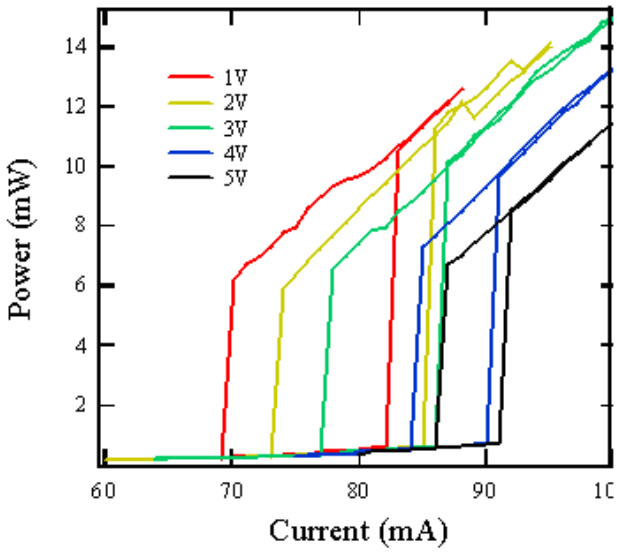

Figure 3-6 L-I curve of 2-section mode-locked laser with absorber biased from –1V to –5V.

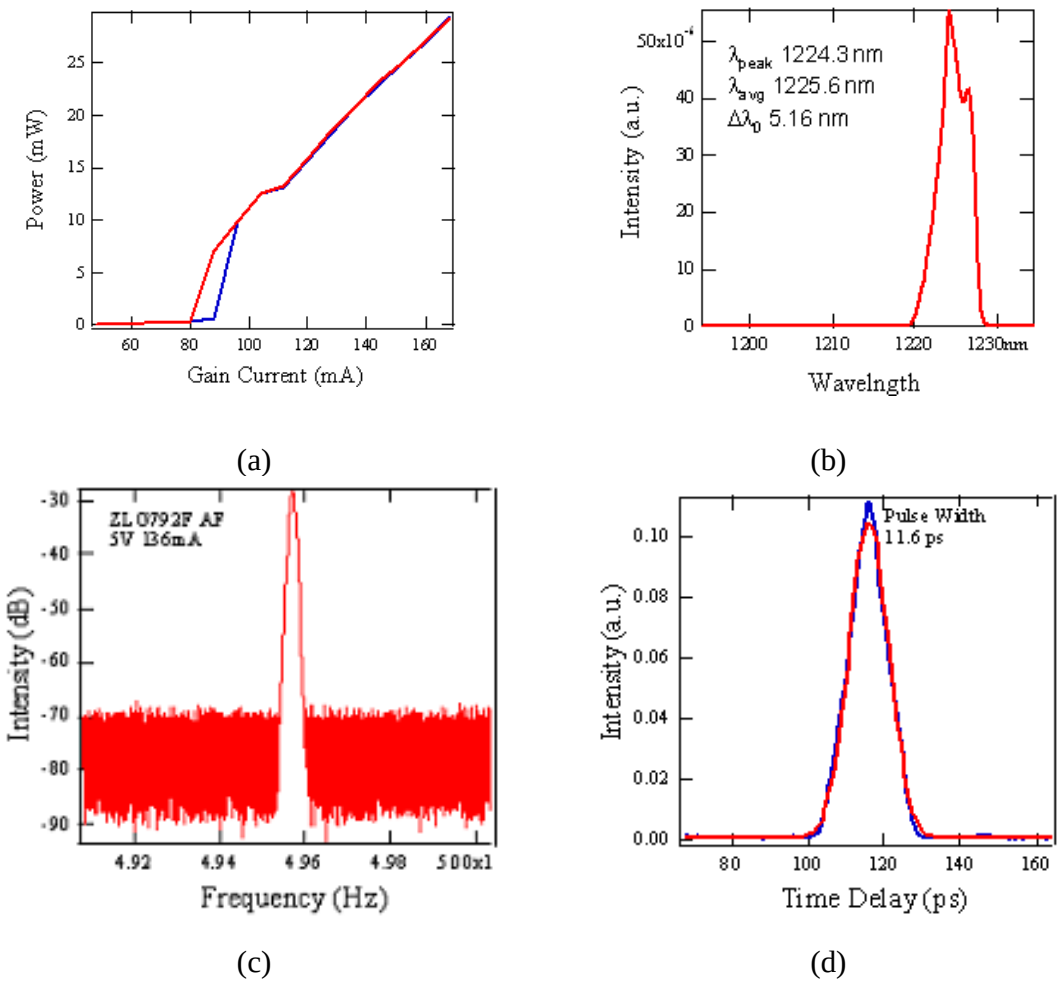

Figure 3-7. Operating characteristics of the two-section-configuration QD passive mode-locked laser under absorber bias of –5V. (a) The CW L-I characteristics. (b) The CW Optical spectrum under a gain current of 136 mA. (c) The ESA spectrum of the 1st harmonic under a gain current of 136 mA. (d) The autocorrelation signal under gain current 136 mA. The FWHM pulse width is 11.6 ps.

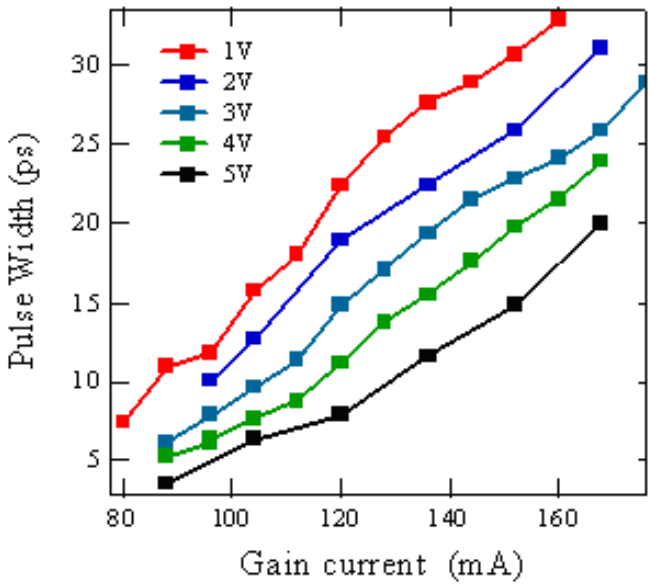

Figure 3-8. The FWHM pulse widths of the two-section-configuration QD passively mode-locked laser under an absorber bias of –1 to –5V.

3.4.2 QD mode-locked laser master equation

Plentiful work has been done on the theory of the semiconductor quantum well (QW) and QD passive mode locking lasers [25, 35, 36, 37]. The physical scheme for passive mode-locking in a QD laser remains the same as in other semiconductor lasers: the absorbing medium saturates faster than the amplifying one, and, therefore, a short window of net gain emerges for the pulse amplification. Therefore, the basic master equation of mode-locking should be valid for QD mode-locked laser performance. With the multi-section mode-locked laser, it is the first time that we can measure all the parameters in the master equation from a single monolithic semiconductor laser and check the solution of the master equation.

Complementary investigations of the carrier dynamics have demonstrated a fast recovery time (~1 ps) in quantum-dot waveguide structures [38]. For a passive semiconductor mode-locked laser, with a fast absorber and the geometrical layout shown in Figure 3-1(b), consider a Lorentzian profile for the gain

$$g(\omega) = \frac{g_0}{1 + i\dfrac{(\omega - \omega_0)}{\Delta\omega_g}} \qquad \text{Eqn 3-3}$$

and the absorption saturates as

$$\alpha = \frac{\alpha_o}{1 + |A|^2 / I_s^a} \qquad \text{Eqn 3-4}$$

and the master equation is then [26]:

$$\frac{\partial A}{\partial z}+\frac{1}{\upsilon_g}\frac{\partial A}{\partial t}=g_n\left(1+\frac{1}{\Delta\omega_g^2}\frac{\partial^2}{\partial t^2}\right)A-\frac{\alpha_{0,n}}{1+\left|A\right|^2/I_s^a}A \qquad \text{Eqn 3-5}$$

where $g_n = g\,L_g/L-\alpha_i-\alpha_m$ is the distributed small-signal gain in the amplifying section, $\alpha_{0,n}=\alpha_0\,L_a/L$, $\alpha_{0,n}$ is the distributed small-signal unsaturated loss in the absorber, L is the total cavity length, L_a is the length of the absorber and L_g is the length of the amplifying section, I_s^a is the saturation intensity of absorber, υ_g is the group velocity, α_{m} is the mirror loss, and α_{i} is the internal loss. The pulse envelope denoted as *A(z, t)* is a function of time and the spatial position. While there are steady-state pulses forming in the cavity, the master equation reduces to

$$\left(g_n-\alpha_{0,n}\right)A+\frac{g_n}{\Delta\omega_g^2}\frac{\partial^2 A}{\partial\eta^2}+\alpha_{0,n}\frac{\left|A\right|^2}{I_s^a}A=0 \qquad \text{Eqn 3-6}$$

where $\eta=t-z/\upsilon_g$. This equation has a solution [26]:

$$A(z,t)=\frac{A_0}{\cosh\gamma\left(z-\upsilon_g t\right)}$$

with

$$\upsilon_g\gamma=\left(\frac{a_{0,n}}{2g}\Delta\omega_g^2\frac{\left|A_0\right|^2}{I_s^a}\right)^{1/2} \qquad \text{Eqn 3-7}$$

and

$$\alpha_{0,n}-g_n=\frac{g_n}{\Delta\omega_g^2}\left(\upsilon_g\gamma\right)^2 \qquad \text{Eqn 3-8}$$

The pulse width for the hyperbolic secant pulse shape is

$$FWHM \approx 1.76\left(\frac{2g_n I_s^a}{\alpha_{0,n}\Delta\omega_g^2 \left|A_0\right|^2}\right)^{1/2} \qquad \text{Eqn 3-9}$$

where the relation between the intensity and power is the following:

$$\frac{\left|A_0\right|^2}{I_s^a} = \frac{P_{peak}}{P_s^a} \qquad \text{Eqn 3-10}$$

in which P_{peak} is the peak power of the pulse, P_s^a is the saturation power of the absorber. We can express the FWHM of the pulse as

$$\Delta t \approx 1.76\left(\frac{2g_n P_s^a}{\alpha_{0,n}\Delta\omega_g^2 P_{peak}}\right)^{1/2} \qquad \text{Eqn 3-11}$$

From this equation we can see that for the same peak power, the FWHM of the pulse decreases with decreasing $g_n/\Delta\omega_g^2$ and saturation power, and increasing normalized absorption assuming that gain saturation, which has been ignored, is negligible.

The peak powers can be calculated with the measured pulse width, repetition rate and average power. The spectra of the net modal gain, the loss and the internal loss can be measured using the segmented contact method. The bandwidth Δω is calculated from the FWHM of optical spectra as $\Delta\omega = c\Delta\lambda/\lambda^2$. Theoretically, we can calculate the saturation power from the measured peak power, optical pulse width *Δt*, FWHM of the optical spectrum, and distributed small-signal gain and absorption, under different bias conditions with Equation 3-11.

The saturation power P_s^a can also be obtained from the small signal absorption α_0 and threshold gain g_0 near the lower threshold with the equation below:

$$g_0 L_g = (\alpha_m + \alpha_i)L + \frac{\alpha_0}{1 + P_{peak} / P_s^a} L_a \qquad \text{Eqn 3-12}$$

Here α_0 was read from the absorption spectra at the corresponding wavelength and bias voltage. The threshold gain g_0 was read from the gain spectrum at the corresponding wavelength under the current density as the point "A" shown in the Figure 3-9, which is the intersection point of the extrapolated line from the L-I curve to the current axis. From the Net modal gain and absorption spectra we have the internal loss of $2cm^{-1}$. The mirror loss is 1.2 cm^{-1} (HR coating of 95% and AR coating of 15%).

We can compare the calculated saturation powers by the two methods to verify the mode-locked laser master equation. However, an accurate saturation power is hard to obtain with Equation 3-12 because of the following issues:

1. The complete mode-locking current is usually significantly higher than the threshold current. It is difficult to measure the pulse width near the threshold current where non-linear gain effects are minimized.
2. The lasing wavelength usually shifts at different bias conditions. The saturation power calculated from the threshold condition does not strictly apply to other wavelengths.

Table 3-1 shows the calculated data of the absorption saturation power near the threshold condition. The Equation 3-12 requires that the lower threshold current is near to the starting current of mode-locking. Therefore, from the table, only the data of reverse bias voltage 5V and 4V are good for the calculation of the saturation power. With Equation 3-11, we calculated absorption saturation powers under different reverse bias from 1V to 5V as shown in the

Table 3-2. The absorption saturation powers by the two methods are plotted in Figure 3-10. Comparing the saturation powers of 5V, 0.45W to 2.2 W, there is a rather large difference between the results of the two methods. We noticed that the master equation model does not treat the effect of nonlinear gain. Since the modal gain also saturates after the device starts lasing, the threshold gain should be smaller than the small signal gain under the threshold current density. This will introduce error in the absorption saturation power calculation. We can check the master equation solution through other methods.

From Equations 3-7 and 3-8, we have:

$$\alpha_{0,n} - g_n = \frac{g_n}{\Delta\omega_g^2}\left(\upsilon_g \gamma\right)^2 = \frac{\alpha_{0,n}}{2}\frac{\left|A_0\right|^2}{I_s^a} = \frac{\alpha_{0,n}}{2}\frac{P_{peak}}{P_s^a}$$
$$\Rightarrow P_{peak} = 2\cdot\left(1-\frac{g_n}{\alpha_{0,n}}\right)P_s^a \qquad \text{Eqn 3-13}$$

From Equation 3-13, P_{peak} is a function only of the small-signal absorption, the gain, and the saturation power. After a mode-locked laser lases, g_n of the lasing wavelength is a constant. The P_s^a and small signal $\alpha_{0,n}$ are functions of the bias voltage and the wavelength. A conclusion from the above discussion is that the peak power at the same wavelength does not change with the pump current or the average power. As shown in Figure 3-11, the peak power for similar operating wavelengths is relatively constant. Another research group has also reported this behavior [39].

There is another form of the Equation 3-11:

$$
\begin{aligned}
(\Delta t)^2 &\approx 1.76^2 \frac{2g_n P_s^a}{\alpha_{0,n}\Delta\omega_g^2 P_{peak}} \\
\Rightarrow P_{peak}\cdot\Delta t\cdot\Delta t\cdot f &= 1.76^2 \frac{2g_n P_s^a}{\alpha_{0,n}\Delta\omega_g^2}\cdot f \\
\Rightarrow P_{average}\cdot\Delta t &= 1.76^2 \frac{2g_n P_s^a}{\alpha_{0,n}\Delta\omega_g^2}\cdot f \\
\Rightarrow \Delta t &= 1.76^2 \frac{2g_n P_s^a}{\alpha_{0,n}\Delta\omega_g^2}\cdot\frac{f}{P_{average}}
\end{aligned}
$$

Eqn 3-14

Here f is the repetition rate. Therefore, for the same average power, the pulse width decreases with normalized loss increasing, gain spectrum broadening, normalized gain decreasing and saturation power decreasing.

In conclusion, because the nonlinear gain is not treated in the mode-locked laser master equation, the master equation model has limitations on the mode-locked laser's properties quantitative calculations. However, this model is still useful for obtaining baseline parameters for a more sophisticated model such as the prediction of the peak power being constant with gain current changing.

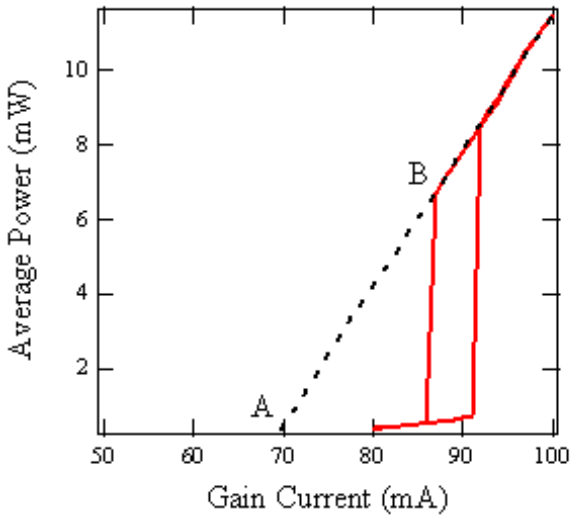

(a)

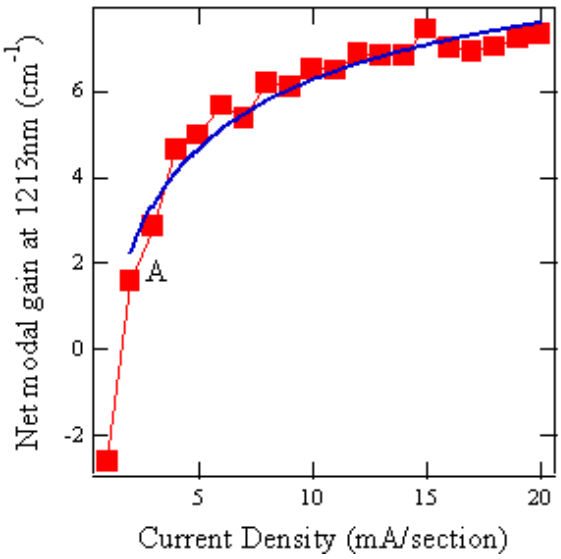

(b)

Figure 3-9 (a) L-I curve under reverse bias of 5V. (b) Net modal gain at 1213 nm vs. current density.

Reverse Bias (V)	Low I_{th} (mA)	Starting current of mode-locking	Point A current (mA)	g_0 at lower I_{th} (cm^{-1})
5	87	88 mA	67	6.97
4	85	88 mA	65.9	6.93
3	78	88 mA	62.3	6.75
2	74	88 mA	53.4	6.3
1	69	80 mA	51.6	6.14

Saturated absorption α (cm^{-1})	Small signal absorption α_0 (cm^{-1})	P_{peak} at starting current of mode-locking (W)	P^a_{sat} (W)
18.03	21.4	0.411	2.2
17.80	21.6	0.326	1.5
16.78	21.2	NA	NA
14.23	21.4	NA	NA
13.32	21.5	NA	NA

Table 3-1 Calculated saturation power near the threshold with Equation 3-12.

Absorber Bias voltage (V)	Current (mA)	Current density (mA/section)	Pulsewidth (ps)	Wavelength (nm)	Average power (mW)	Frequency (GHz)
5V	88	6.5	3.5	1213.1	7.128	4.94
4V	88	6.5	5.3	1213.34	8.472	4.9444
3V	88	6.5	6.1	1213.38	9.9	4.9444
2V	96	7.1	10.1	1224.02	13.464	4.9559
1V	80	5.9	7.5	1214.18	9.71	4.9525

Peak Power (W)	Modal gain (cm^{-1})	Small signal absorption (cm^{-1})	$\Delta\lambda$ (nm)	FWHM of optical spectra (Hz)	P^{a}_{sat} (W)
0. 411	6. 97	21. 4	3. 36	6.85×10^{11}	0. 451
0. 326	6. 93	21. 6	3. 04	6.19×10^{11}	0. 672
0. 326	6. 75	21. 2	2. 92	5.95×10^{11}	0. 880
0. 269	6. 3	18. 298	3. 12	6.25×10^{11}	2. 20
0. 263	6. 14	21. 5	2. 64	5.37×10^{11}	1. 09

Table 3-2 Calculated saturation power with the master equation solution (Equation 3-11).

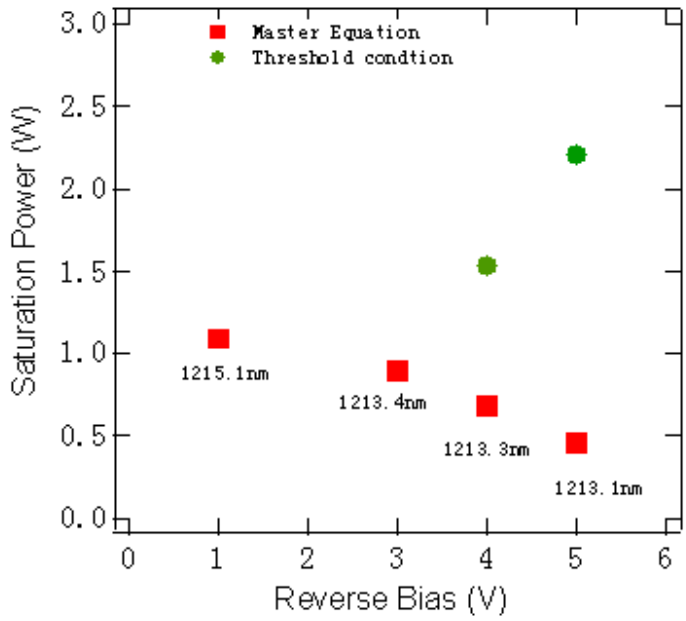

Figure 3-10. The absorption saturation powers under different reverse biased voltages.

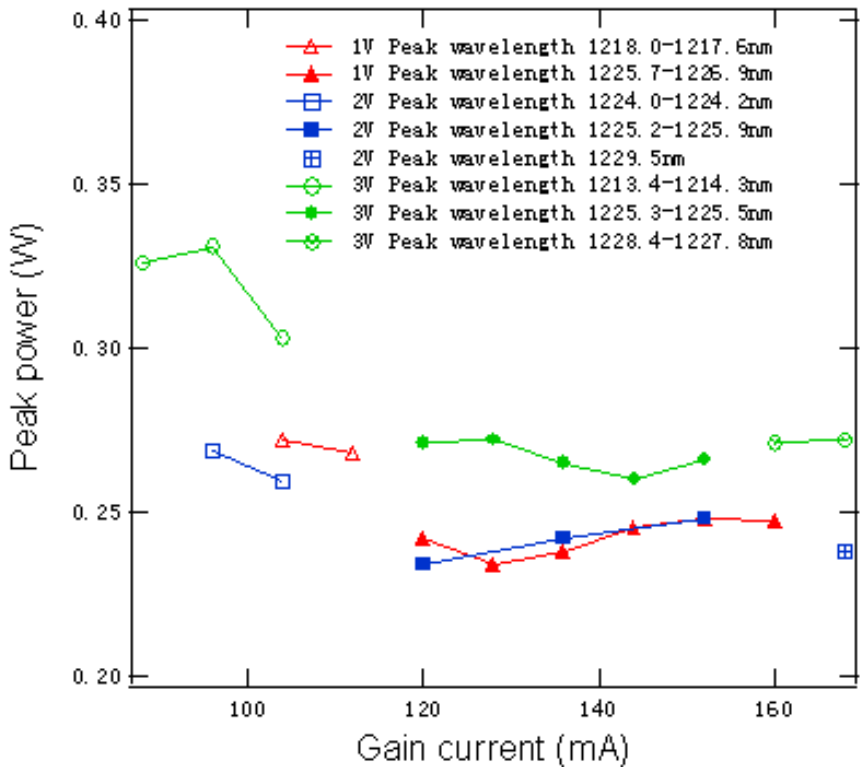

Figure 3-11. Peak power of the 2-section mode-locked laser..

3.5 Monolithic Multi-Section Passively Mode-Locked Lasers

With the highly flexible, reconfigurable multi-section approach, we obtained and compared different laser layouts within the same device. The objectives in studying the multi-section mode-locked laser are focused on pulse narrowing and higher order harmonic mode-locking.

3.5.1 Optical pulse narrowing with multi-section mode-locked lasers.

In this dissertation, the multi-section mode-locked laser design divides a passive mode-locked laser into three sections: an absorber section, a gain section and a passive waveguide section. A similar technique has been applied to QW mode-locked lasers. A monolithically integrated passive waveguide was embedded in a QW passive mode-locked laser to reduce the repetition rate to a relatively low frequency. The passive waveguide was fabricated with quantum well intermixing (QWI). This structure also reduces the phase noise, consequently, the timing jitter by the ratio of the active section reduction [40].

In the QD multi-section mode-locked laser, the device is composed of a single-mode ridge waveguide divided into three electrically isolated sections as shown in Figure 3-12 by pump method selections. The quasi-passive waveguide does not require any special processing and is pumped at the transparency current density so that the light sees zero net modal gain in this section at the operating wavelength. The transparency current density is found from the net modal gain data measured by the improved segmented contact method on the actual device, not a test device.

Keeping the total cavity length the same, the addition of the passive waveguide forces the gain section in the 3-section mode-locked laser to work at the higher current density shown as point “B” in Figure 3-13 (b). This differential gain is much smaller than that of the 2-section mode-locked laser operating at point “A”. The novel design will improve the mode-locked laser characteristics in the following ways:

- The multi-section QD mode-locked laser design increases the saturation photon density by running the gain section in strong population inversion, decreases nonlinear gain suppression and should result in narrower pulse width and higher peak powers.
- Since the gain section operates at higher current density, the wider gain bandwidth should result in pulse narrowing based on Equation 3-11.
- The inclusion of a passive waveguide increases the overall ratio of stimulated to spontaneous emission in the cavity, which should decrease noise.

Considering that it is desirable to locate the absorber near an HR mirror facet to induce the self-colliding pulse effect [33], there are two realistic layouts for mode-locking the 3-section mode-locked laser at the round-trip frequency of the laser cavity. In the absorber-gain-passive (AGP) design (Figure 3-12), the gain section is positioned between the absorber and the passive section. In the absorber-passive-gain (APG) layout, the passive section is between the absorber and the gain section. During operation, the passive section is biased with a current to achieve optical transparency since we are not able to fabricate a truly passive section in these particular designs.

Another approach for pulse narrowing is the dual-gain section or absorber-gain section- gain section (AGG) geometry. The two gain sections have different amplifier

lengths. The short gain section is pumped at a higher current density and the longer one at a lower current density than in the case of the 2-section laser with a single amplifying segment. The AGG design is intended to widen the gain spectrum in the mode-locked laser device, and generate a narrower pulse width by increasing the number of locked modes.

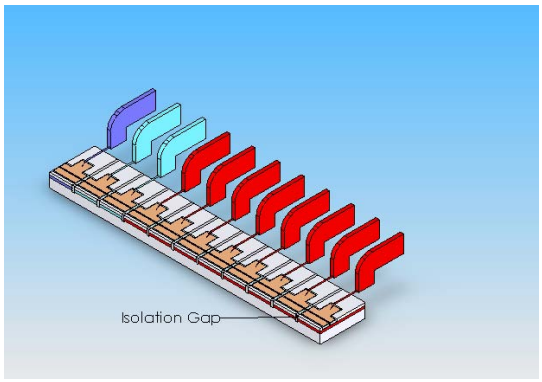

(a) APG

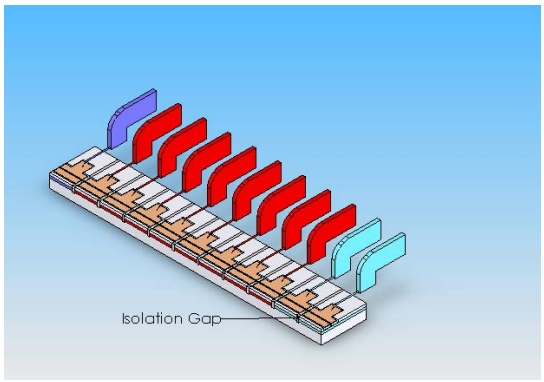

(b) AGP

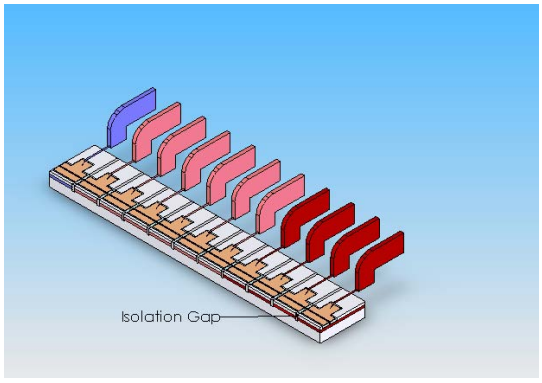

(c) AGG

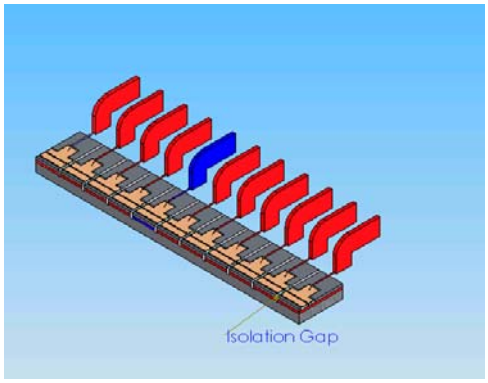

(d) GAG

Figure 3-12. The device layout of the (a) absorber -passive-gain (APG) mode-locked laser, (b) absorber-gain-passive (AGP) mode-locked laser, (c) absorber-low pump gain-high pump gain (AGG) mode-locked laser, (d) gain-absorber-gain (GAG) mode-locked laser.

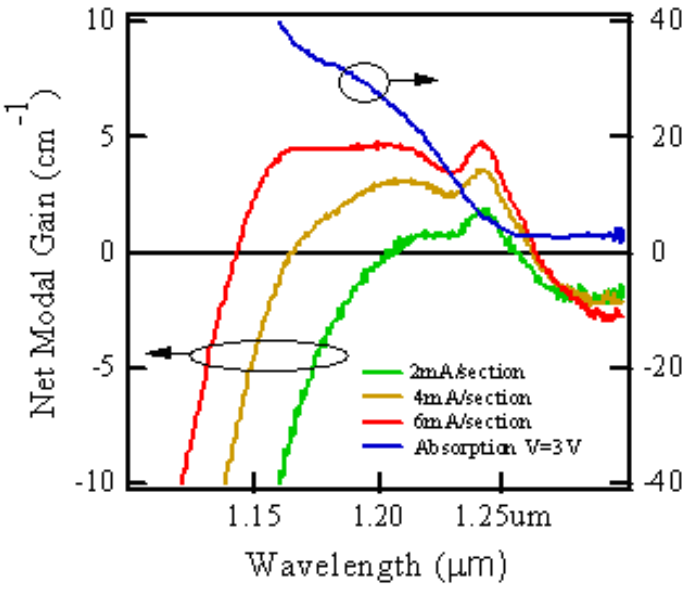

(a)

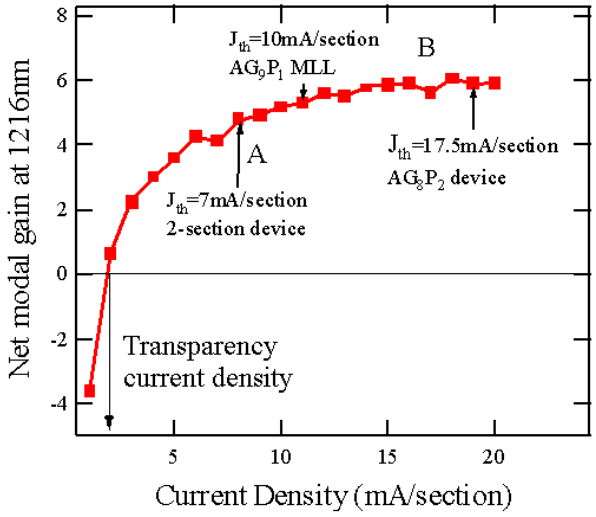

(b)

Figure 3-13. (a) Measured net modal gain and absorption spectra of the QD active region. (b) The net modal gain at 1216nm. The arrows point out the operation gain value of 2-section and AGP structures.

The total device length of 5.5-mm was segmented into 11 implant-isolated 0.5-mm sections. The 11 sections were pumped by either a multi-channel current source to form various individual gain sections or a voltage source supplying reverse bias to the absorber. The QD mode-locked laser was systematically configured in the APG, AGP, AGG and GAG layouts. The measurements were performed at a controlled substrate temperature of 20°C.

For pulse width and peak power improvement at the fundamental repetition rate, six different geometrical configurations were tested: the AGP and APG versions with 1-mm and 0.5-mm passive sections, the AGG structure with 3- and 2-mm gain sections, and a conventional 2-section mode-locked laser. The length of the absorber section was kept constant at 0.5 mm. From the net modal gain and the absorption spectra, which were obtained with the segmented contact method [34, 41] and are shown in Figure 3-13, the passive section was biased with a current density of 1.5 mA/section (100 A/cm^2) to achieve optical transparency, while a reverse bias voltage of 3V was applied on the absorber. The repetition rate of the devices was about 7.2 GHz, and the pulse width as a function of the average output power is shown in Figure 3-14 (a). All of the multi-section mode-locked lasers achieved narrower pulse widths compared to the 2-section mode-locked laser. With same passive waveguide section length, the AGP structure shows better pulse narrowing effect than the APG structure. A longer passive section in a mode-locked laser is generally better in terms of pulse width and peak power, which confirms the hypothesis that operating the gain section under strong population inversion improves the mode-locked laser performance. The optimized configuration, the AGP structure with a 1-mm passive section, improves the pulse width by about 35% compared to the 2-

section device, correspondingly the peak power increases up to 49% as shown in Figure 3-14 (b). The AGG geometry has no significant advantage over the APG or AGP layouts probably because the gain spectrum, as shown in Figure 3-13, is already rather inhomogeneous for this particular QD laser wafer. With an average power of above 12 mW, the pulsewidth of AGP devices is 1-3 ps narrower than that of the APGs, which is believed to be caused by reduced non-linear gain effects in the shorter continuous gain path in the AGP.

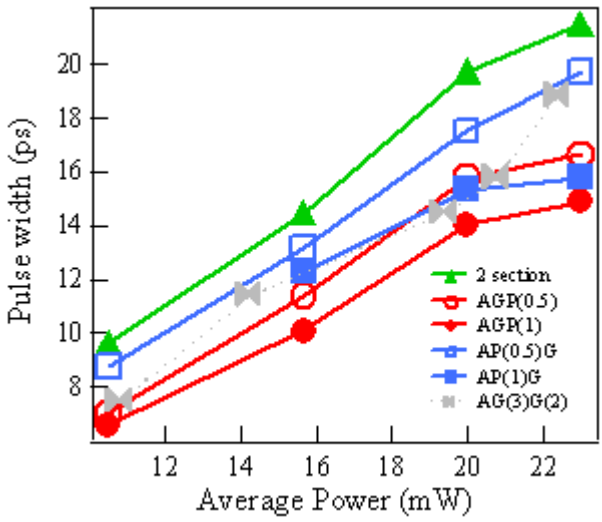

(a)

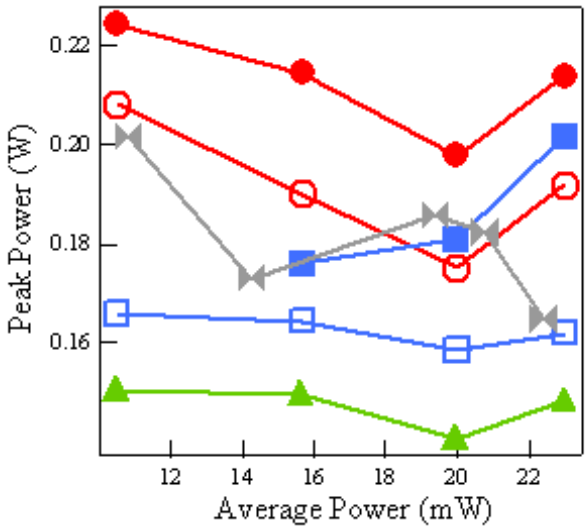

(b)

Figure 3-14. (a) Pulse width of the QD mode-locked lasers vs. average power. (b) Peak power of the QD mode-locked lasers vs. average power.

3.5.2 Higher order harmonic mode-locking in multi-section mode-locked lasers

The final triple-section configuration of interest positions the absorber between the two gain sections (GAG) as shown in Figure 3-12(d), and can be implemented to excite higher order harmonics of the fundamental repetition rate using the asymmetrical colliding pulse technique [42, 43].

To achieve harmonic mode-locking at multiples of the 7.2 GHz fundamental frequency, the 0.5-mm absorber was placed in one of the cavity sections away from the end mirrors. The equivalent structures of higher order harmonically mode-locked CPM lasers are shown in Figure 3-15. The HR mirror effectively folds the cavity without power loss and this has a profound effect on the relative strength of the pulses colliding in the absorber. Inserting the absorber at position 9, 8, 6, 5 or 4 resulted in good mode-locking, and the corresponding repetition rates with the different absorber locations are listed in Table 3-3. Since the ESA has a span limit from 9kHz to 26.5GHz, the repetition rate of the 6^{th} and 7^{th} harmonic exceeds this limit and is calculated directly from the period between the two pulses measured in the autocorrelator. The pulse shapes and ESA spectra of different harmonic mode-locking configurations are shown in Figure 3-16. The mode-locking pulse and peak power are mapped as a function of gain current and absorber voltage in Figure 3-17. With the mode-locked laser operated under harmonic mode-locking conditions, the pulses are narrowed due to CPM. While the repetition rate increased from the 1^{st} order to the 3^{rd} order, the achieved maximum peak power also increased. The peak power of 234 mW from the 6^{th} harmonic mode-locking is a record peak power for QD mode-locked lasers operating over 40 GHz [14].

A broad operation range is desirable for a semiconductor mode-locked laser, which will permit the device to operate stably with a high reverse bias voltage and a wide span of gain currents. An operating range with wide span of gain currents will minimize the instability due to the current or temperature changing. A higher reverse bias on the absorber causes a shorter electron transit time in the absorber that works similar to high-speed PIN photodiode. With a shorter electron transit time, the carrier density in the absorber will relax faster and the recovery time will be shorter. Hence, the pulse width is improved with increasing reverse bias. Also, with increasing reverse bias on the absorber, the small signal absorption increases due to the quantum confined stark effect in the DWELL structure. This effect will also narrow the pulse. Inserting the absorber at position 8, an extra-broad operation range with pulse width below 10 ps was obtained. The operation range area is almost 3 times larger than the area of the same device with absorber instead at section number 11 adjacent to the HR-coated facet. From the Figure 3-15, the structure with the 8^{th} section as absorber has the most symmetric gain section length ratio near to 1.07:1:1.07. It is the reason that the structure with the 8^{th} section as the absorber exhibited extra-broad operation range due to its symmetric cavity geometry.

The gain and absorber section lengths are discrete since the minimum section length is 0.5mm. However, sections at both ends can be less or more than 0.5 mm due to cleaving. Therefore, we can obtain very high frequency mode-locking when the location of the absorber satisfies the nth order harmonic CPM condition [42]. With the absorber placed at section 9 and the bias voltage set at 0 V, we obtained incomplete mode-locking at 115 GHz with pump currents ranging from 100 mA to 130 mA. The pulse shape is

shown in Figure 3-18. We can expect to obtain even higher frequencies by cleaving the end sections to different lengths without decreasing the absorber's length.

3.6 Conclusion

In this chapter, the relationship between the 2-section SCPM laser operation characteristics and the QD material characteristics was studied, and the solution of the master equation of mode-locking with a fast saturable absorber was checked. Novel multi-section monolithic passive mode-locked lasers with quasi-passive waveguide were introduced. The AGP multi-section mode-locked laser significantly increased the peak pulsed power (> 45%) and improved the pulse width (>35%) of the QD mode-locked lasers compared with conventional 2-section SCPM lasers. By setting the absorber position to form the GAG structure within the same optical cavity, the device can operate at high order harmonics. Up to the 7^{th} harmonic with complete locking was demonstrated, and incomplete locking as high as the 15^{th} harmonic was achieved.

Absorber Position No.	11	9	8	6	5	4
Repetition Rate (GHz)	7. 21	42. 4	21. 6	14. 42	50. 7	21. 6
Max Peak Power (mW)	393	243	473	491	70	

Table 3-3**.** Higher order harmonic mode-locking repetition rates achieved with the absorber placed at different positions in the optical cavity.

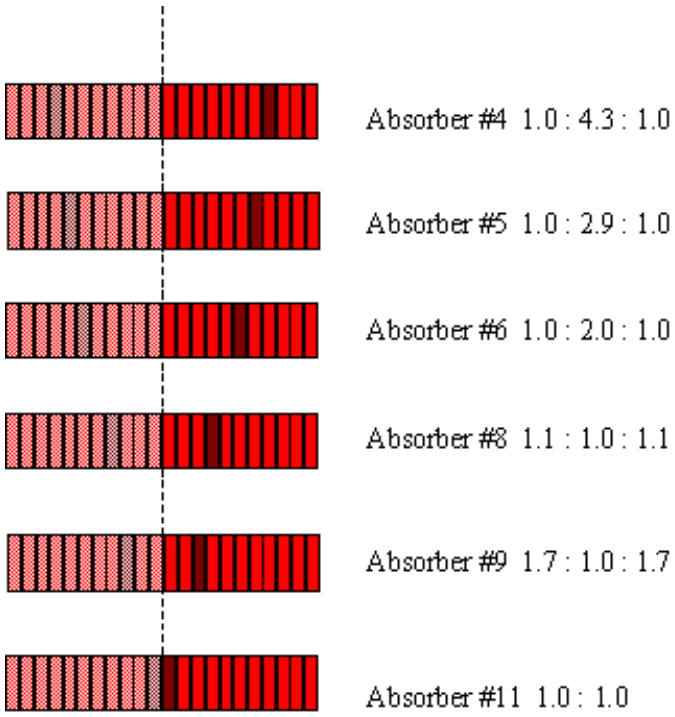

Figure 3-15 Equivalent structures of higher order harmonically mode-locked CPM lasers. The dashed line represents the HR coating which effectively folds the cavity.

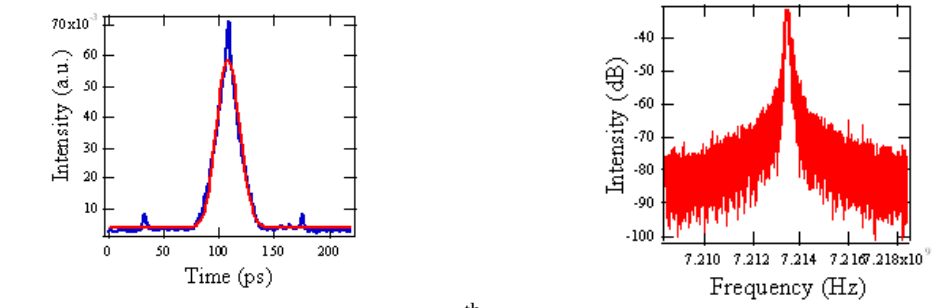

11th 9V 150mA

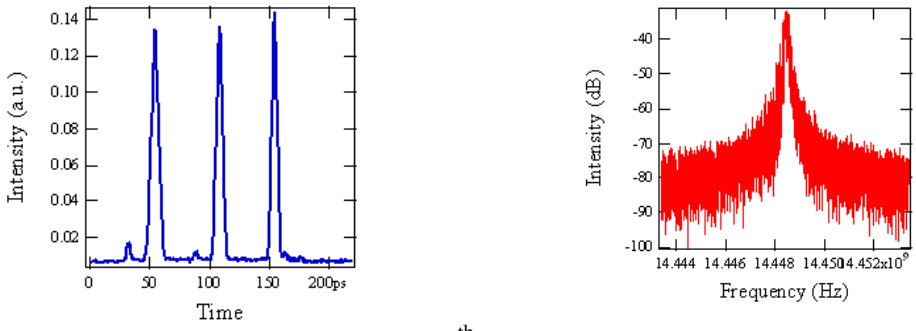

6th 6V 170mA

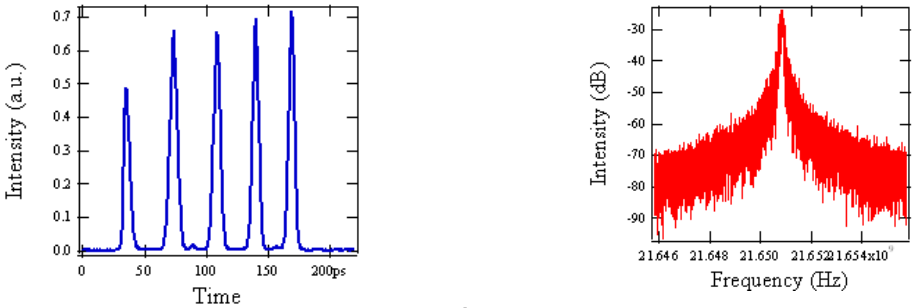

8th 8V 300mA

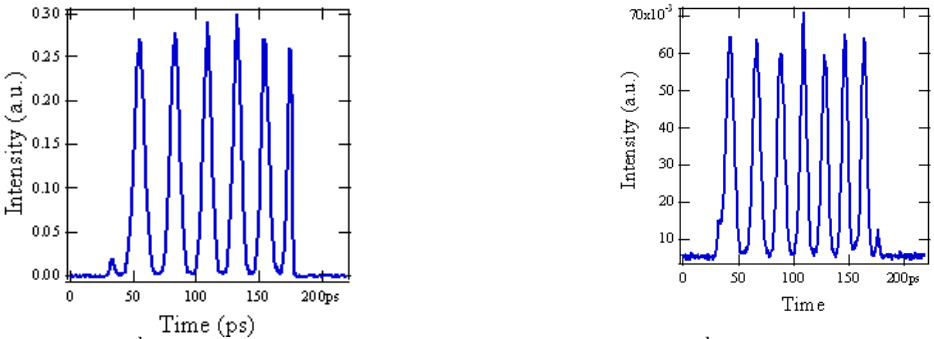

9th 8V 320mA　　5th 1V 150mA

Figure 3-16 Pulse shape of multi-section mode-locked lasers.

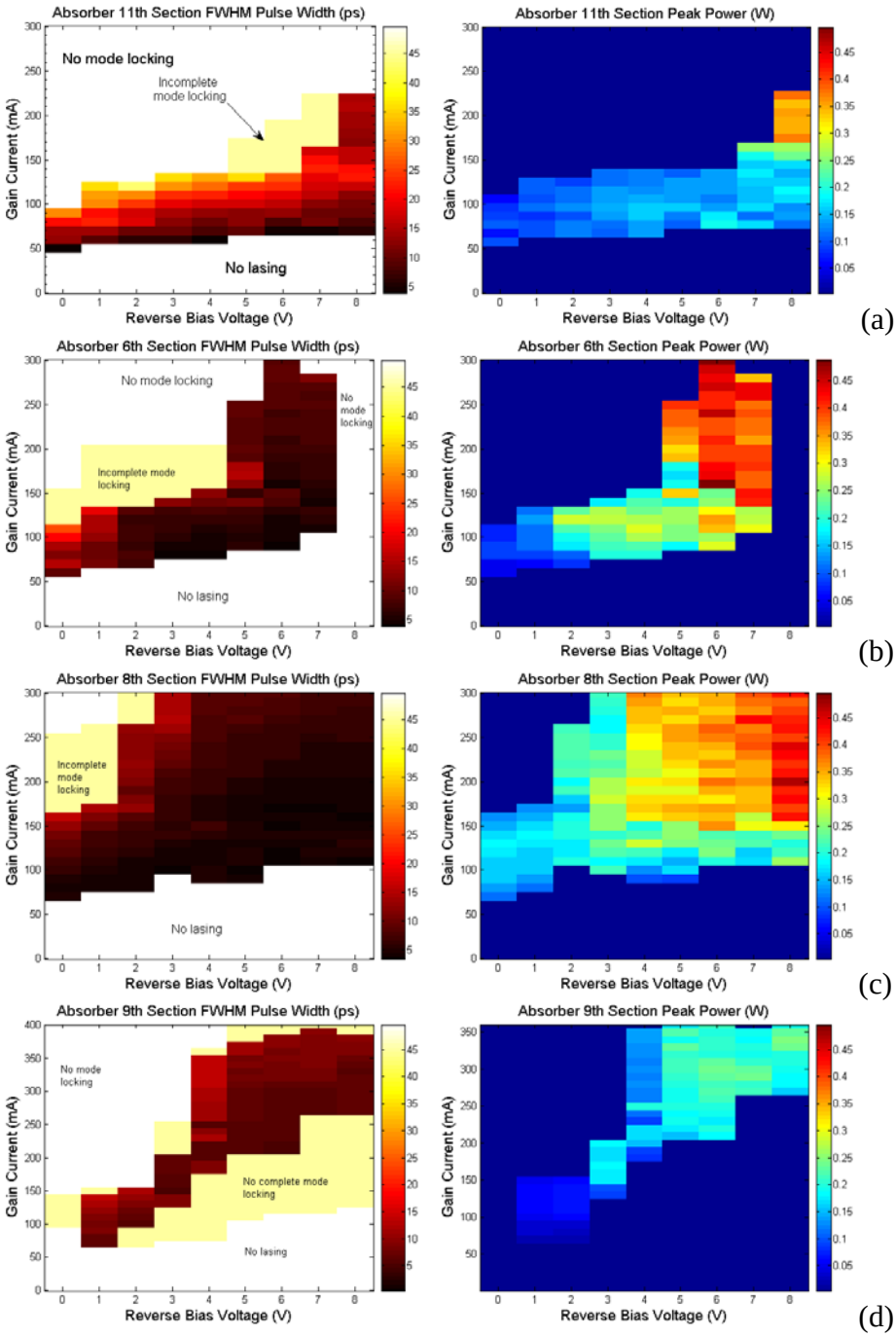

Figure 3-17 Optical Pulse width and peak power maps of the 1st, 2nd, 3rd, 6th harmonic mode-locking configurations.

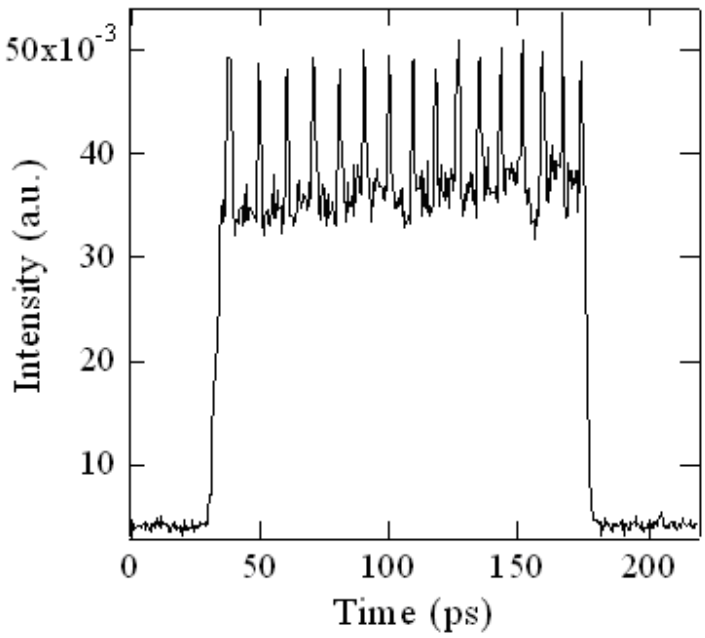

Figure 3-18. Incomplete mode-locking of a QD mode-locked laser with the absorber at position 9. The pump current is 120 mA and reverse bias is 0 V.

3.7 References for Chapter 3

1 Gaburro, Z., “Optical interconnect”, in Silicon Photonics; 2004; Vol.94, pp.121-176, Pavesi L & Lockwood, D. J., Topics in Applied Physics, Springer Verlag, 2004.

2 L.Zhang, L.Cheng, A.L.Gray, S.Luong, J.Nagyvary, F.Nabulsi, L.Olona, K.Su, T.Tumolillo, R Wang, C.Wiggins, J.Ziko, Z.Zau, P.M.Varangis, Su, H., and Lester, L. F., "5 GHz Optical Pulses From a Monolithic Two-Section Passively Mode-locked 1250/1310 nm Quantum Dot Laser for High Speed Optical Interconnects," *Optical Fiber Communication Conference.Technical Digest.OFC/NFOEC*, vol. 3 2005.

3 Miller, D. A. B., "Rationale and challenges for optical interconnects to electronic chips," *Proceedings of the IEEE*, vol. 88, no. 6, pp. 728-749, 2000.

4 Keeler, G. A., Nelson, B. E., Agarwal, D., Debaes, C., Helman, N. C., Bhatnagar, A., and Miller, D. A. B., "The benefits of ultrashort optical pulses in optically interconnected systems," *IEEE Journal of Selected Topics in Quantum Electronics*, vol. 9, no. 2, pp. 477-485, 2003.

5 Sotobayashi, H., Chujo, W., Konishi, A., and Ozeki, T., "Wavelength-band generation and transmission of 3.24-Tbit/s (81-channel WDMX40-Gbit/s) carrier-suppressed return-to-zero format by use of a single supercontinuum source for frequency standardization," *Journal of the Optical Society of America B-Optical Physics*, vol. 19, no. 11, pp. 2803-2809, 2002.

6 Mielke, M., Alphonse, G. A., and Delfyett, P. J., "168 channels x 6 GHz from a multiwavelength mode-locked semiconductor laser," *IEEE Photonics Technology Letters*, vol. 15, no. 4, pp. 501-503, 2003.

7 J.-C. Diels. Apparatus and method for line of sight laser communication. United States Patent, Approved Nov. 30, 2001 2002. Patent Application Serial N0 09/215,420

8 Landa Arissian and Jean-Claude Dieals. " Mode-locked laser as a combined radio frequency and optical clock stabilized to a reference cavity, and calibrated through coherent interaction with rubidium." *Applications of Photonic Technology 6, vol. 5260-82, pp. 1-10, SPIE, 2003*

9 Jean-Claude Diels, Ladan Arissian. " Applications of stabilized frequency combs to metrology". *Proceedings of the International Conference on Coherent and Nolinear Optics, and on Lasers, Applications and Technologies (ICONO/LAT 2005). SPIE, 2005*

10 Kolner, B. H. And Bloom, D. M., "Electrooptic Sampling In Gaas Integrated-Circuits," *Ieee Journal Of Quantum Electronics*, Vol. 22, No. 1, Pp. 79-93, 1986.

11 Williams, K. A., Thompson, M. G., and White, I. H., "Long-wavelength monolithic mode-locked diode lasers," *New Journal of Physics*, vol. 6 pp. 179, 2004.

12 Liu, G. T., Stintz, A., Li, H., Malloy, K. J., and Lester, L. F., "Extremely low room-temperature threshold current density diode lasers using InAs dots in In0.15Ga0.85As quantum well," *Electronics Letters*, vol. 35, no. 14, pp. 1163-1165, 1999.

13 Huffaker, D. L., Park, G., Zou, Z. Z., Shchekin, O. B., and Deppe, D. G., "Continuous-wave low-threshold performance of 1.3-mu m InGaAs-GaAs quantum-dot

lasers," *IEEE Journal of Selected Topics in Quantum Electronics*, vol. 6, no. 3, pp. 452-461, 2000.

14 Bimberg, D. and Ledentsov, N., "Quantum dots: lasers and amplifiers," *Journal of Physics-Condensed Matter*, vol. 15, no. 24, pp. R1063-R1076, 2003.

15 Ribbat, C., Sellin, R. L., Kaiander, I., Hopfer, F., Ledentsov, N. N., Bimberg, D., Kovsh, A. R., Ustinov, V. M., Zhukov, A. E., and Maximov, M. V., "Complete suppression of filamentation and superior beam quality in quantum-dot lasers," *Applied Physics Letters*, vol. 82, no. 6, pp. 952-954, 2003.

16 Huang, X. D., Stintz, A., Li, H., Lester, L. F., Cheng, J., and Malloy, K. J., "Passive mode-locking in 1.3 mu m two-section InAs quantum dot lasers," *Applied Physics Letters*, vol. 78, no. 19, pp. 2825-2827, 2001.

17 Huang, X. D., Stintz, A., Li, H., Rice, A., Liu, G. T., Lester, L. F., Cheng, J., and Malloy, K. J., "Bistable operation of a two-section 1.3-mu m InAs quantum dot laser - Absorption saturation and the quantum confined Stark effect," *IEEE Journal of Quantum Electronics*, vol. 37, no. 3, pp. 414-417, 2001.

18 Sellin, R. L., Ribbat, C., Grundmann, M., Ledentsov, N. N., and Bimberg, D., "Close-to-ideal device characteristics of high-power InGaAs/GaAs quantum dot lasers," *Applied Physics Letters*, vol. 78, no. 9, pp. 1207-1209, 2001.

19 Kuntz, M., Fiol, G., Lammlin, M., Bimberg, D., Thompson, M. G., Tan, K. T., Marinelli, C., Penty, R. V., White, I. H., Ustinov, V. M., Zhukov, A. E., Shernyakov, Y.

M., and Kovsh, A. R., "35 GHz mode-locking of 1.3 mu m quantum dot lasers," *Applied Physics Letters*, vol. 85, no. 5, pp. 843-845, 2004.

20 Mauro J. Kobrinsky, et al., "On-Chip Optical Interconnects, "Intel Technology Journal, Volume 8, Issue 2, 2004

21 Mike Salib, et al., "Silicon Photonics", Intel Technology Journal, Volume 8, Issue 2, 2004

22 I. S. Ruddock and D. J. Bradley. " Bandwidth-Limited subpicosecond pulse gerneration in mode-locked cw dye lasers", *Appl. Phys. Lett.*, vol. 29, No. 5. pp 296. 1976.

23 R. L. Fork, B. I. Greene, And C. V. Shank, "Generation Of Optical Pulses Shorter Than 0.1 Psec By Colliding Pulse Mode-Locking," *Appl. Phys. Lett*. **38,** 671-672 (1981).

24 Bischoff, S., Mork, J., Franck, T., Brorson, S. D., Hofmann, M., Frojdh, K., Prip, L., and Sorensen, M. P., "Monolithic colliding pulse mode-locked semiconductor lasers," *Quantum and Semiclassical Optics*, vol. 9, no. 5, pp. 655-674, 1997.

25 Koumans, R. G. M. P. and vanRoijen, R., "Theory for passive mode-locking in semiconductor laser structures including the effects of self-phase modulation, dispersion, and pulse collisions," *IEEE Journal of Quantum Electronics*, vol. 32, no. 3, pp. 478-492, 1996.

26 Vasilev P., *Ultrafast Diode Lasers, Fundamentals and Applications, 1995.*

27 Joseph T. Verdeyen, *Laser Electronics*, 3rd edition, 1995.

28 Keller, U., "Recent developments in compact ultrafast lasers," *Nature*, vol. 424, no. 6950, pp. 831-838, 2003.

29 Liu, G. T., Stintz, A., Li, H., Malloy, K. J., and Lester, L. F., "Extremely low room-temperature threshold current density diode lasers using InAs dots in In0.15Ga0.85As quantum well," *Electron.Lett.*, vol. 35, no. 14, pp. 1163-1165, 1999.

30 Stintz, A., Liu, G. T., Gray, A. L., Spillers, R., Delgado, S. M., and Malloy, K. J., "Characterization of InAs quantum dots in strained InxGa1-xAs quantum wells," *Journal of Vacuum Science & Technology B*, vol. 18, no. 3, pp. 1496-1501, 2000.

31. L. Zhang, R. Wang, Z. Zou, A. Gray, L. Olana, T. Newell, D. Webb, P. Varangis and L. Lester, “InAs quantum dot DFB lasers on GaAs for uncooled 1310nm fiber communications,” Optical Fiber Communications 2003, Paper FG2, Atlanta, Mar. 23-28, 2003.

32 Venus, G. B., Gadzhiev, I. M., Gubenko, A. E., Il'inskaya, N. D., and Portnoi, E. L., "Picosecond semiconductor lasers with a multisection saturable absorber, fabricated by heavy ion implantation," *Technical Physics Letters*, vol. 25, no. 7, pp. 506-508, 1999.

33 Derickson, D. J., Helkey, R. J., Mar, A., Karin, J. R., Wasserbauer, J. G., And Bowers, J. E., "Short Pulse Generation Using Multisegment Mode-Locked Semiconductor-Lasers," *Ieee Journal Of Quantum Electronics*, Vol. 28, No. 10, Pp. 2186-2202, 1992.

34 Xin, Y. C., Li, Y., Martinez, A., Rotter, T. J., Su, H., Zhang, L., Gray, A. L., Luong, S., Sun, K., Zou, Z., Zilko, J., Varangis, P. M., and Lester, L. F., "Optical gain and absorption of quantum dots measured using an alternative segmented contact method," *IEEE Journal of Quantum Electronics*, vol. 42, no. 7-8, pp. 725-732, 2006.

35 Haus, H. A., "Mode-Locked Semiconductor Diode-Lasers," *Philosophical Transactions of the Royal Society of London Series A-Mathematical Physical and Engineering Sciences*, vol. 298, no. 1439, pp. 257-266, 1980.

36 Haus, H. A. And Silberberg, Y., "Theory Of Mode-Locking Of A Laser Diode With A Multiple-Quantum-Well Structure," *Journal of the Optical Society of America B-Optical Physics*, vol. 2, no. 7, pp. 1237-1243, 1985.

37 Viktorov, E. A., Mandel, P., Vladimirov, A. G., and Bandelow, U., "Model for mode locking in quantum dot lasers," *Applied Physics Letters*, vol. 88, no. 20, pp. 201102, 2006.

38 Rafailov, E. U., White, S. J., Lagatsky, A. A., Miller, A., Sibbett, W., Livshits, D. A., Zhukov, A. E., and Ustinov, V. M., "Fast quantum-dot saturable absorber for passive mode-locking of solid-state lasers," *IEEE Photonics Technology Letters*, vol. 16, no. 11, pp. 2439-2441, 2004.

39 L. Zhang, L. Cheng, A. L. Gray, H. Li, S. Luong, J. Nagyvary, F. Nabulsi, L. Olona, K. Sun, T. Tumolillo, R. Wang, C. Wiggins, J. Zilko, Z. Zou, and P. M. Varangis, L. Lester "Low timing jitter, 5 GHz optical pulses from monolithic two-section passively mode-locked 1250/1310 nm Quantum Dot lasers for high speed optical interconnects", OFC 2005.

40 Camacho, F., Avrutin, E. A., Bryce, A. C., and Marsh, J. H., "Passive modelocking in semiconductor lasers with monolithically integrated passive waveguides," *IEE Proceedings-Optoelectronics*, vol. 145, no. 1, pp. 43-46, 1998.

41 Osborne, S. W., Blood, P., Smowton, P. M., Xin, Y. C., Stintz, A., Huffaker, D., and Lester, L. F., "Optical absorption cross section of quantum dots," *Journal of Physics-Condensed Matter*, vol. 16, no. 35, pp. S3749-S3756, 2004.

42 Shimizu, T., Wang, X. L., and Yokoyama, H., "Asymmetric colliding-pulse mode-locking in InGaAsP semiconductor lasers," *Optical Review*, vol. 2, no. 6, pp. 401-403, 1995.

43 Shimizu, T., Ogura, I., and Yokoyama, H., "860 GHz rate asymmetric colliding pulse modelocked diode lasers," *Electronics Letters*, vol. 33, no. 22, pp. 1868-1869, 1997.

Chapter 4 Quantum Dot Super-Luminescent Light Emitting Diodes

4.1 Introduction

Super-luminescent light emitting diodes (SLEDs) are the ideal source for applications that require high output power and a broad emission spectrum. They are of increasing interest for a range of applications such as gyroscopes, fiber-optics sensors, wavelength division multiplexing (WDM) system testing and optical coherence tomography (OCT) as the correspondingly short coherence length can significantly improve the spatial resolution in coherence based systems.

Optical coherence tomography (OCT) is a rapidly emerging high-resolution biomedical imaging technology that provides two-dimensional, cross-sectional, micron-scale images of biological and medical specialties [1, 2].

There are three key technological parameters of OCT related to the optical source: longitudinal (axial) resolution, possible penetration into the investigated tissue, and overall costs of the OCT system. The longitudinal resolution is related to the bandwidth of the optical source as [3]:

$$\Delta z = 2\ln(2)\frac{\lambda^2}{\pi\Delta\lambda} \qquad \text{Eqn 4-1}$$

Standard resolution OCT with 10-15 μm axial resolution has been applied extensively for imaging tissue microstructure in several medical specialties, ranging from ophthalmology, cardiology to gastroenterology [4, 5]. However, the median size of a skin cell is approximately 20 μm and a resolution of about 5 μm is required for the OCT to diagnose an aberrant cell. As shown in the Figure 4-1 [3], with the bandwidth of the optical source

improving from 100 nm to 150 nm, the longitudinal (axial) resolution of OCT will improve from 8μm to 5μm. Therefore, optical sources with spectral bandwidths greater than 150 nm are desirable in OCT [3, 6]. Due to strong multiple scattering in skin tissue, an operating wavelength of 1.3 μm is important for improving possible penetration in medical applications. The ultrahigh resolution optical coherence tomography (UHR-OCT) with axial resolution of 1-3 μm was demonstrated using either femtosecond solid-state lasers or femtosecond lasers in combination with nonlinear optical fibers [7, 8]. However, femtosecond lasers are expensive and difficult to operate, a situation that presents a major challenge to the widespread adoption of UHR-OCT imaging technology in the clinical setting [9]. SLED sources are compact, robust, easy to operate, and much less expensive than femtosecond solid-state lasers, thus, minimizing the overall costs of OCT.

In quantum well (QW) SLEDs, many approaches have been applied to achieve these features including multiplexed broadband super luminescent diodes [9], post-growth quantum well intermixing [10], SLEDs integrated with a tapered semiconductor optical amplifier [11], and chirped multiple quantum wells (MQWs) [12, 13]. However, these techniques have one or several problems such as large spectral modulation, low output power, limited bandwidth, or complex growth techniques. Recently, QD active regions have attracted attention for SLEDs because of the wide inhomogeneously broadened spectrum made possible by controlling the dot composition and geometry [14, 15, 16, 17, 18, 19, 20, 21]. These QD approaches compare favorably with quantum well versions, but simultaneously wide spectral bandwidth (> 150 nm) and reasonable power (>1 mW) in a QD SLED has been elusive.

In this chapter, we will describe a novel ridge-waveguide QD SLED that emits near 1.3 μm. The multi-section device configuration enables the realization of ultra-wide 3-dB bandwidth (> 150 nm) and an output power greater than 1 mW with a uniform multi-stack QD structure. The new SLED allows a high flexibility in the design and can be reconfigured to adjust independently the power and the spectral bandwidth relative to the ground state (GS) and the excited state (ES) of the QD. The other advantage is that it doesn't require complex growth techniques.

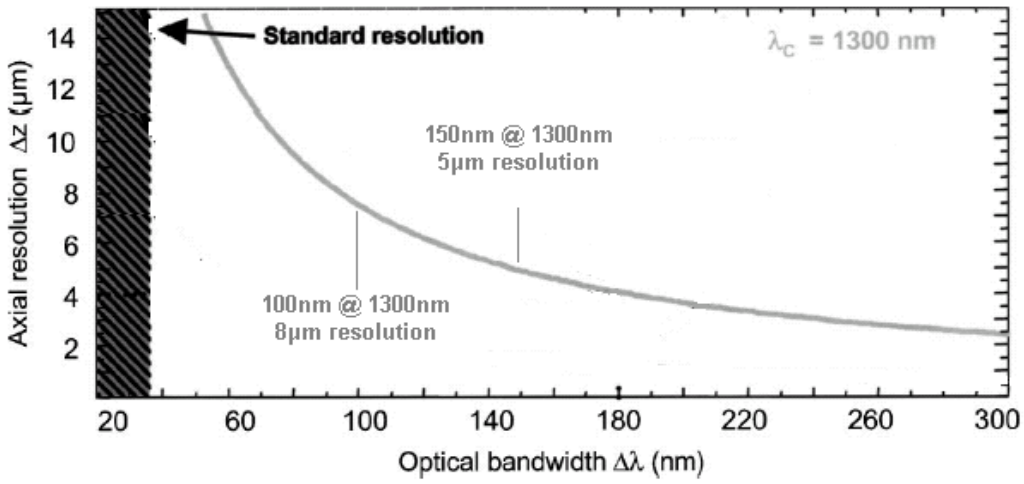

Figure 4-1 Longitudinal (axial) resolution vs. the bandwidth of the OCT optical source

4.2 Two-section QDs SLEDs

4.2.1 Introduction of two-section SLEDs

There are two main conventional SLEDs structures: tilted waveguide SLEDs and two-section SLEDs. The titled waveguide SLED has an angle of 5-7° tilted from the normal to the waveguide direction to eliminate back-reflected light from the facets. However, such a structure introduces more complexity in alignment and output coupling in the typical optical fiber packaging. A multi-section SLED consists of a single-mode ridge waveguide divided into two electrically isolated sections. In the two-section SLED, the front section is forward biased and works as the gain section to provide light emission; the second section is reverse biased and works as the absorber to eliminate the back reflected light and suppress stimulated emission. The two-section SLEDs can use standard packaging techniques for a semiconductor laser diode. In our research, we use straight waveguide structures.

The emission intensity of two-section SLEDs is a function of the net modal gain, g, and the gain section length, L:

$$I = \frac{S}{g}\left(\exp(g \cdot L) - 1\right) \qquad \text{Eqn 4-2}$$

Where the S is the intensity of the spontaneous emission. The bandwidth of SLEDs is related to both the bandwidth of the net modal gain and the gain section length.

4.2.2 Device structure and fabrication

The two-section SLED devices were fabricated from uniform 6-stack un-doped QDs structure grown by molecular beam epitaxy [22]. The wafer number is Zia393. The photon luminescence spectra of the un-doped QDs have full wave half maximum (FWHM) over 80 nm with ground state peak wavelength of 1.25 μm. The wide inhomogeneous line broadening of un-doped quantum dot spontaneous emission is caused by a relatively large fluctuation in the self-assembled QD sizes. The wafers were processed into two-section devices following standard ridge waveguide laser processing. The samples were etched to form a 3-μm wide ridge waveguide by inductively coupled plasma (ICP) etching in BCl_3. The ridges are etched down to 200 nm above the active region for improved optical field confinement. Ion implantation was used to isolate the adjacent sections. After n-type metal was deposited on the substrate side of the wafer, the samples were annealed at 380°C for one minute. The final two-section device has a total length of 8.0 mm and composed of 2 segmented-contact sections. The gain section lengths vary from 0.6 mm to 5.0 mm.

4.2.3 Two-section SLED characterization

The two-section SLEDs were mounted on a copper heat sink and a temperature controller was used for maintaining the stage temperature at 25 °C. The gain section was pumped with a pulse current source. The pulse had a duty cycle of 5% and pulse width of 0.5 μs. A reverse bias of 7.0 V was applied on the absorber.

The evolution of the output power and FWHM of different gain section length SLEDs were tested and are shown in Figure 4-2 and Figure 4-3. As the gain section length

increases, the output power increases and the FWHM decreases rapidly. The FWHM of a 2-section SLED that has a gain section length of 0.8 mm can be up to 120 nm. However, the maximum output power is less than 0.1 mW. A 2-section device with 3-mm gain section has an output power of 0.3 mW and an FWHM or 65 nm or an FWHM of 100 nm with an output power of only 0.1 mW. In general for the two-section SLEDs, the gain section length was limited to 3 mm to ensure an FWHM > 100 nm and power > 0.1 mW. In addition, if too much gain current is applied over a long gain section (L>3 mm), the SLED will start to operate as a laser since the reverse biased quantum dot absorber is saturable.

In conclusion, it is difficult to satisfy the requirement of wide bandwidth and high output power in a two-section QD SLED. A new SLED structure is needed for achieving high power and wide bandwidth with nominally uniform QD materials.

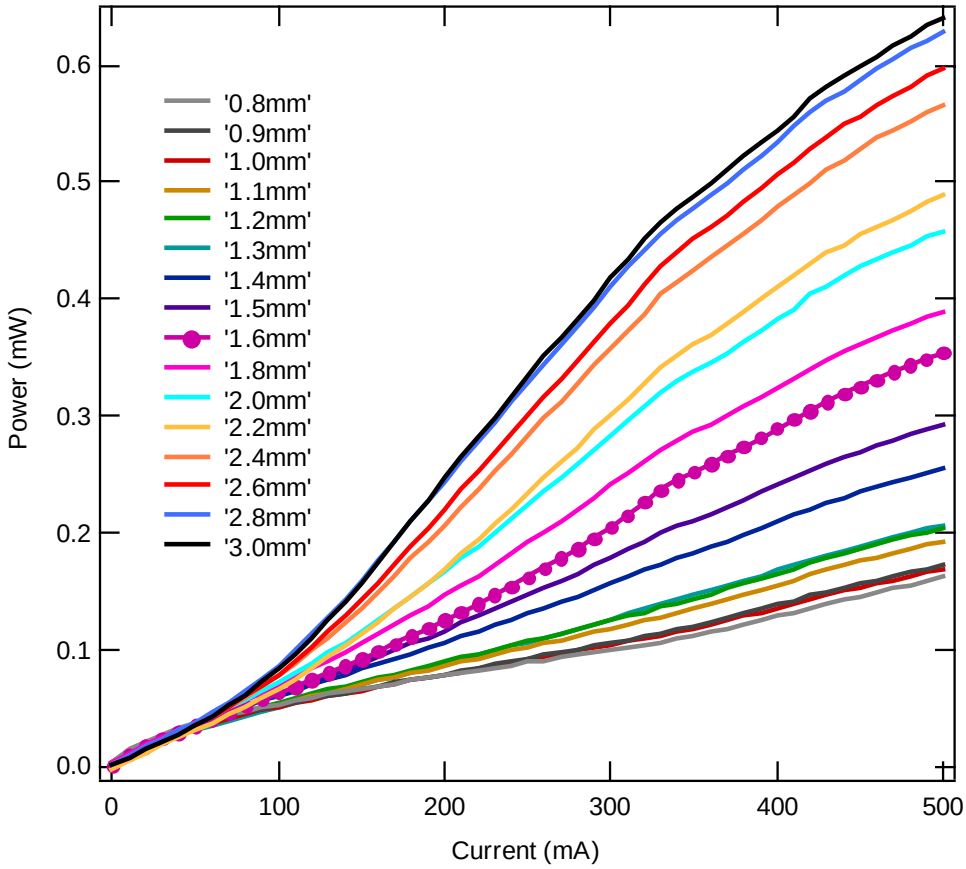

Figure 4-2 L-I curves of two-section SLEDs with different gain section lengths. The gain section length varies from 0.8 mm to 3.0 mm.

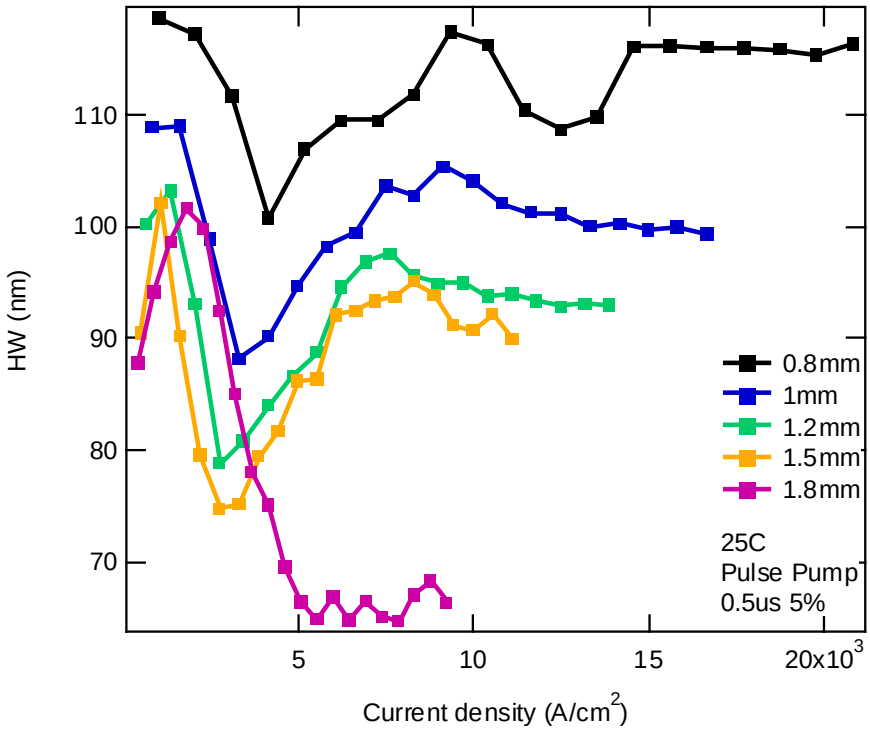

Figure 4-3 FWHM as a function of bias current density of two-section SLEDs with different gain section lengths.

4.3 Multi-section SLEDs

As we discussed before, the two-section SLED is difficult to satisfy both the requirement of wide bandwidth and high output power. For achieving high power and wide bandwidth SLEDs with conventional QD structures, a novel device structure for SLEDs is required. In our work, we have observed that a three-section structure with two asymmetrically pumped gain sections and one absorber is a key for significantly improving the SLEDs' bandwidth and output power simultaneously. The ratio of the sections lengths is important in optimizing multi-section SLEDs.

4.3.1 Basic principles of the improved multi-section SLED

The improved SLED design consists of a single-mode ridge waveguide divided into three electrically isolated sections as shown in Figure 4-6. The absorber section, *Abs*, located at the rear facet, is reverse-biased to eliminate the back reflections. The two gain sections, A_1 and A_2, amplify the spontaneous emission. The optical gain and the spectral bandwidth of the amplifiers are tuned through the current densities and the sections lengths, L_1 and L_2.

The intensity of the amplified spontaneous emission (ASE) changes with transmission length and the optical gain. The amplified spontaneous emission can be found from the following equation [23]:

$$I_{ASE} = (I_0 + \frac{S}{G})\exp(G \cdot x) - \frac{S}{G} \qquad \text{Eqn 4-3}$$

Where I_{ASE} is the ASE intensity, G is the net modal gain defined by $G = \Gamma g_m - \alpha_i$, Γ is the confinement factor, g_m the material gain, and α_i is internal loss. S is the pure spontaneous emission intensity. I_0 is the initial light intensity at x=0.

In the 3-section SLED, the single-pass ASE is amplified in the two gain sections which have different injected current densities. The optical gain and spontaneous emission are functions of the wavelength λ, injected current density J, and junction temperature, T. Assuming that the output of section A2 is the input to section A1, the overall output of the 3-section SLED with two gain sections is described by the equation:

$$I(\lambda) = \frac{S(J_2,T_2,\lambda)}{G(J_2,T_2,\lambda)}\exp\left[G(J_2,T_2,\lambda)\cdot L_2 + G(J_1,T_1,\lambda)\cdot L_1\right] + \left(\frac{S(J_1,T_1,\lambda)}{G(J_1,T,\lambda_1)} - \frac{S(J_2,T_2,\lambda)}{G(J_2,T_2,\lambda)}\right)\exp\left(G(J_1,T_1,\lambda)\cdot L_1\right) - \frac{S(J_1,T_1,\lambda_1)}{G(J_1,T_1,\lambda_1)} \qquad \text{Eqn 4-4}$$

Here I is the ASE intensity at the wavelength λ. J_1 and J_2 are the injected current densities in the first and second sections respectively.

Hence, for a given 3-section SLD, adjustment of the current densities and lengths in A_1 and A_2 permits control of the power output and bandwidth related to the ground state (GS) or excited states (ES) of the dots. For best performance, the device is typically operated such that amplifier A_1 is saturated with peak emission at the QD ES and A_2 is biased with output favoring the QD GS. This approach reduces the optimization to the manageable problem of tailoring the sum and relative lengths of the gain sections. Increasing the lengths of the amplifiers results in increasing the power but also in a narrowing of the spectral bandwidth. The optimal configuration obtains an equivalent

power for the GS and ES bands and simultaneously maximizes the bandwidth by minimizing the intensity dip between the two states. In addition, the red shift of the excited state emission from section A_1 due to its higher junction temperature from a large bias current density reduces the dip between the GS and ES.

Gain spectra and pure spontaneous emission of an undoped QD amplifier were tested with the improved segmented method and are shown in Figure 4-4. With the Equation 4-4, we can estimate the output emission for differently configured multi-section SLEDs. The Figure 4-5 shows the calculated output emissions of 2-section (a) and 3-section devices (b). The figures show that the 3-section SLED has wider bandwidth and better spectral shape than the same cavity size 2-section SLEDs. By changing the section lengths, the output emissions were modulated. From the theory and the measured gain and spontaneous emission data, we can predict an optimal configuration with L_1 = 2.5 mm and L_2 = 4.2 mm, which has both a high output power and reasonably flat spectrum shape. These predicted gain section lengths are used as guidelines for designing the undoped QD devices in the following sections. It will be seen that this equation 4.4 and the data from the improved segmented contact model come very close to predicting the optimized values of the real device.

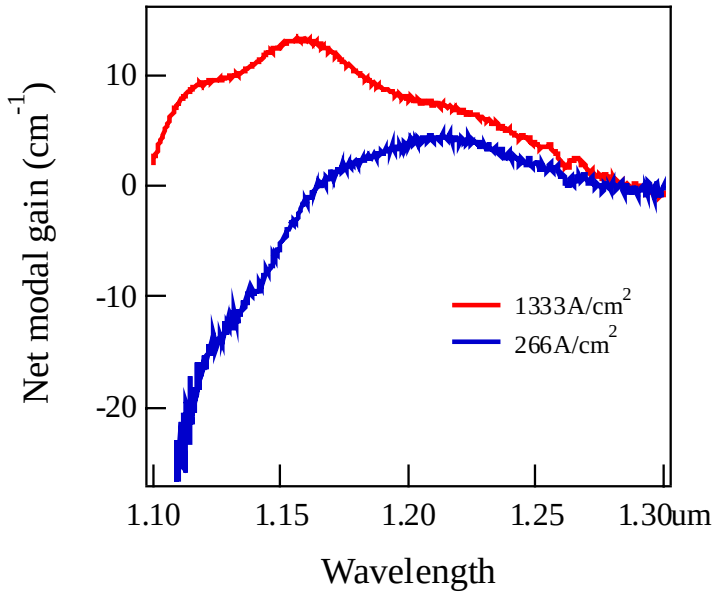

(a)

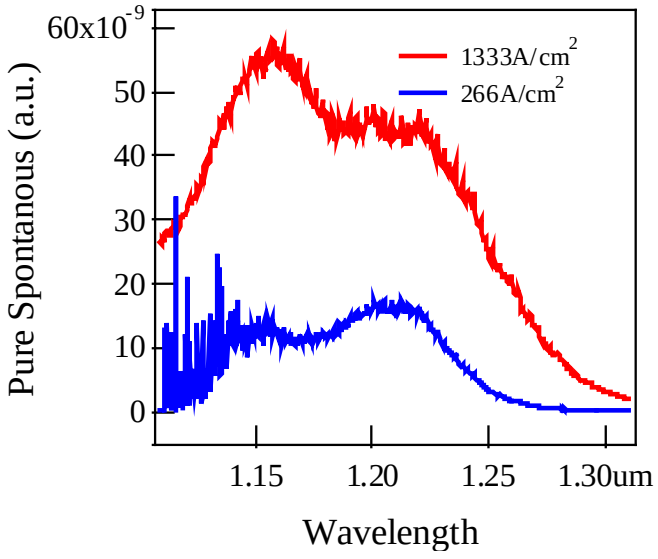

(b)

Figure 4-4. (a) Gain spectra of QDs under pump current densities of 266A/cm^2 and 1333A/cm^2. (b) Pure spontaneous spectra under pump current densities of 266A/cm^2 and 1333A/cm^2.

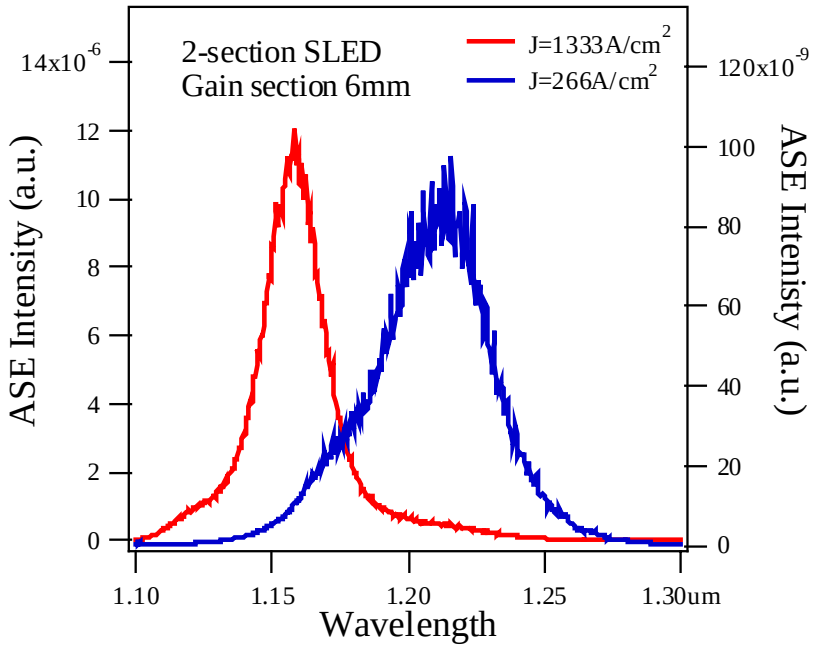

(a)

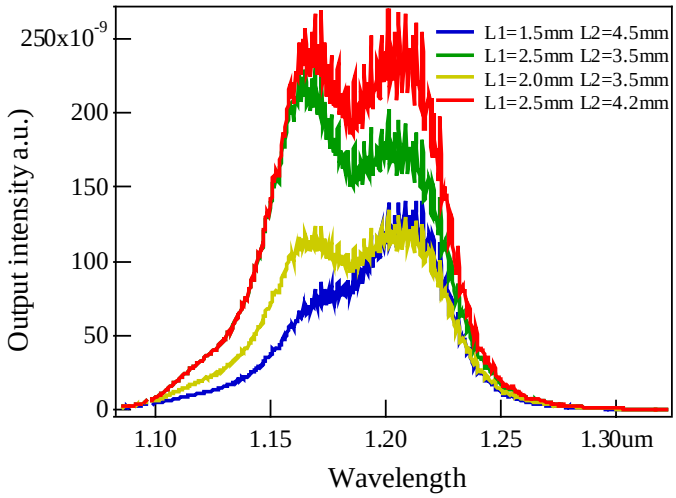

Figure 4-5. (a) Output emission spectra of 6mm 2-section SLEDs calculated with Equation 4-3. (b) Output emission spectra of multi-section SLEDs calculated with Equation 4-4. The injected current density on the section 1 is 266 A/cm^2 and on the section 2 is 1333 A/cm^2.

4.3.2 Device structure and fabrication

The SLED devices were fabricated from two uniform multi-stack QD structures, un-doped QDs (Zia393) and p-type modulation doped QDs (Zia857). The p-doped SLED active region is made of 6 p-doped InAs/GaAs QD layers. Both structures have been grown by molecular beam epitaxy [22]. Broad area light emitters fabricated from the p-doped QD material showed emission at 1.25 μm on the ground state with a FWHM of 50 nm and 1.19 μm for the excited state. The wafers were processed into multi-section devices following standard ridge waveguide laser processing. The samples were etched to form a 3-μm wide ridge waveguide by inductively coupled plasma (ICP) etching in BCl_3. The ridges are etched down to 200 nm above the active region for improved optical field confinement. Ion implantation was used to isolate the adjacent sections. A final multi-section device is composed of 16 segmented-contact sections. Each section is 0.5-mm and the total optical cavity length is 8-mm. After n-type metal was deposited, the samples were annealed at 380°C for one minute. Such a device can be tested with either a free space coupling system or a single mode fiber. By changing the wire-bonding configuration, we can vary the section lengths in same device.

4.3.3 Multi-section SLED characterization

The multi-section device configuration enables the realization of ultra-wide 3-dB bandwidth and a reasonable output power with a uniform multi-stack QD structure. The devices were mounted p-side up on a copper heatsink. A TE cooler was used to control temperature. A reverse voltage of –7.0V was applied on the absorber to eliminate the reflected light from back facet. The SLEDs were tested under pulsed and continuous-

wave (CW) pumping conditions. For the pulsed pumping test, the two gain sections were pumped with one pulse current source and a series resistor was used to distribute different current densities into the two gain sections. For CW pumping, sections *A1* and *A2* were pumped by two CW current sources individually. By varying the lengths of the gain sections and current densities on the two gain sections, we can optimize the SLED designs for different purposes.

For this particular case, the undoped QD materials have an advantage of wider bandwidth than the p-doped QD materials (80 vs. 50 nm FWHM). The p-doped QDs structures have higher optical gain and higher characteristic temperature (T_0 > 100 K vs 50 K) than the un-doped QDs so that it is promising for high current density, high output power applications that dissipate a lot of heat.

4.3.3.1 Undoped QD SLEDs

Figure 4-7 shows the output power of 3-section un-doped QD SLED versus the total current in pulsed operation with L_1 = 0.5 mm and L_2 = 2.5 mm under different current distributions. We can find that the output power decreases as the current distribution asymmetry increases. Figure 4-8 shows the emission spectra of a 3-section undoped QD SLED under different current distributions. The ratio between the current i_1/i_{total} equals 60%, and 50%, respectively. Figure 4-9 reduces this spectral data to the more convenient FWHM figure-of-merit and illustrates the evolution of the FWHM versus the total current in pulsed operation. As the current distribution inhomogeneity increases, the bandwidth increases. Meanwhile, the dip in light emission between the ground state and exited state decreases. Figure 4-10 shows the spectrum when the current applied on section *A1*, i_1, is 300 mA and the total current is 500 mA. The FWHM is as much as 220 nm, which is a

record for a single emitter SLED, with an output power of 0.15 mW. The dip between the GS and the ES is less than 1.5 dB. As a reference, a 2-section SLED with a 3-mm gain section has a bandwidth of 74 nm when the injected current is 500 mA.

By changing the bonding configuration, the section lengths were varied and an optimized structure for pulsed and CW operation was obtained with the same device. The optimized structure has L_1 = 2 mm and L_2 = 4 mm, which is very close to the simulation values from the previous section. The devices were tested under pulsed and CW pumping. Figure 4-11 shows the complete emission spectra, and Figure 4-12 illustrates the evolution of the FWHM and the output power versus the total current (i.e., i_1+ i_2) in pulsed operation. The ratio between the bias currents, i_1/i_2, is 3.2. Our measurements show a maximum FWHM of 164 nm with an output power of 1.2 mW for a total current of 1 A. Moreover, the dip between the GS and the ES is less than 1 dB.

During CW pump test, the TEC was set at 5°C. The section A_1 worked at 400 mA where its ES emission saturated. For a given combination of L_1, i_1 and L_2, our experiments show that the FWHM exhibits a maximum value for a certain current i_2, while the output power keeps increasing with i_2. This is illustrated in Figure 4-13, where the FWHM and the CW output power are plotted versus i_2. The FWHM stays constant (~90 nm) until i_2 = 30 mA, and then increases with i_2 to reach a maximum value of 136 nm for i_2 = 57 mA. The corresponding CW power is 0.18 mW. The abrupt increase in bandwidth comes from the emergence of the GS emission from section *A2* as shown in the Figure 4-13 inset. The bandwidth decreases at higher current when section A_2 dominates the emission. Further increase of the current i_2 above 57 mA decreases both

the bandwidth and output power because the ES intensity from the dots is suppressed at high junction temperature.

With the multi-section un-doped SLED, a high resolution OCT image of an onion skin was obtained by Southwest Sciences and is shown in Figure 4-14. The SLED operated at a condition of FWHM equal to 90 nm and a peak wavelength of 1225 nm. Total light power was only about 0.10~0.12 mW into the fiber used for coupling. The measured spatial (axial) resolution was 7.8 um, compared to the theoretical value of 7.3 um.

The multi-section SLED fabricated from the undoped QD wafer has the advantage of a record FWHM. However, its small gain and low characteristic temperature of about 40-50 K at the ES limits the output power. For the characteristics of a multi-section SLED, the p-doped QD structure is actually the preferred choice for simultaneous high power and wide bandwidth.

4.3.3.2 P-doped QD SLEDs

As mentioned previously, the p-doped QD structures typically have higher maximum optical gain and higher characteristic temperature than the un-doped QDs. The exact values of maximum gain and T_0 are not known. Nonetheless, the modulation doping using Be in the GaAs barrier also increases the spontaneous emission rate because of the presence of a high hole concentration in the dots. The FWHM and the CW output power of a wide bandwidth p-doped SLED (wafer Zia857) at 10 °C are plotted versus i_2 in the Figure 4-15. The device has a 1.5-mm 1st section and a 5-mm 2nd section. The spectra of this SLED are shown in Figure 4-16. The FWHM stays constant (~100 nm) until 60mA,

and then increases strongly with i_2 to reach a maximum value of 168 nm for i_2 = 100 mA. The corresponding cw output power is 0.43 mW.

By increasing L_1 to 2 mm and keeping L_2 = 5 mm, a higher CW power of 1.25 mW can be obtained, but a lower FWHM of 123 nm for i_1 = 700 mA and i_2 = 140 mA is observed as shown in the Figure 4-17 and Figure 4-18.

4.3.4 Discussion

Finally, we discuss some general findings on the optimization of the section length ratio, L_1/L_2. Figure 4-19 plots the maximum bandwidth and the related power of an undoped QD SLD as a function of L_1/L_2 for a total length of 6-mm. As shown in the figure, the FWHM monotonically decreases with increasing L_1/L_2. Concurrently, the output power at maximum FWHM will increase when L_1/L_2 is less than 0.4 and then decrease above this value. From Figure 4-19, an optimized L_1/L_2 that balances the GS and ES emission should be between 0.2 to 0.6 for increased bandwidth beyond a conventional single-section device and a power above 1 mW. This plot shows that the multi-section SLD is not overly sensitive to exact section lengths and bias currents.

4.4 Conclusion

Novel ridge-waveguide QD SLEDs with 2 gain sections and one absorber that emit near 1.3 μm were discussed in the chapter. Theoretical equations were also presented that accurately predict the optimal values for device section lengths in these 3-section SLEDs. The multi-section device geometry enables the simultaneous realization of an ultra-wide 3-dB bandwidth (> 150 nm) and an output power greater than 1 mW with a nominally uniform multi-stack QD structure. The new SLD allows a high flexibility in the design

and can be reconfigured to adjust independently the power and the spectral bandwidth relative to the ground state (GS) and the excited state (ES) of the QD. Combined with more complex materials structures such as chirped QDs, further improvement in bandwidth and power may be possible.

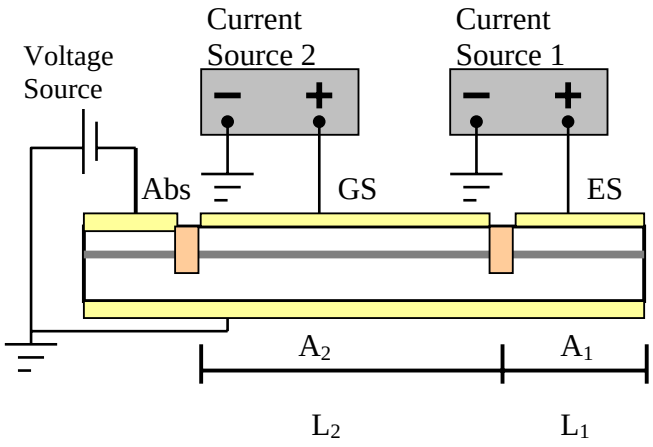

(a)

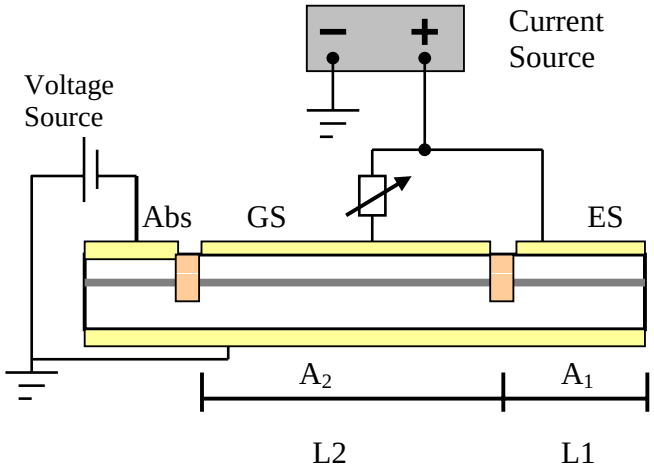

(b)

Figure 4-6. Geometrical layouts of the 3-section SLEDs and bias configurations.

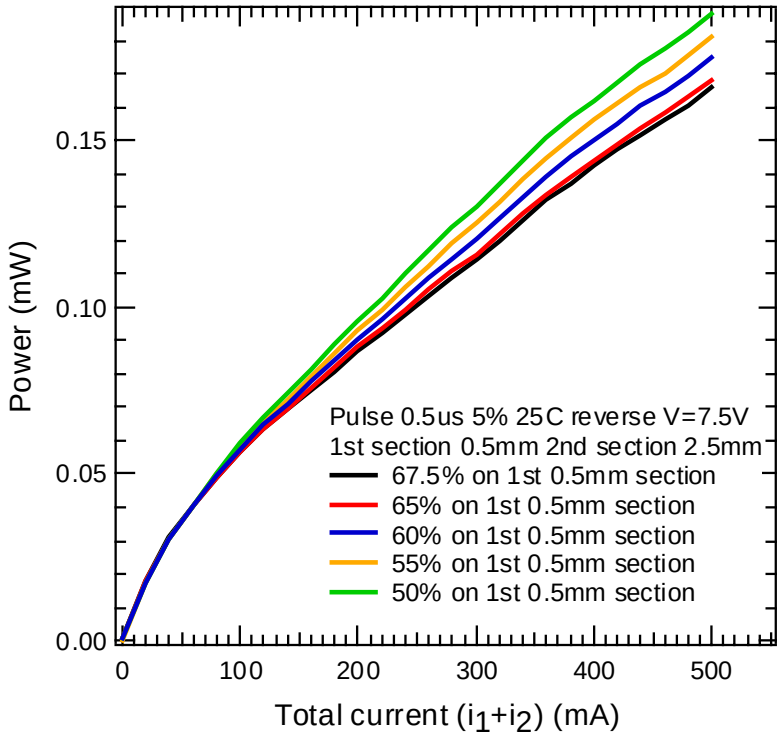

Figure 4-7. Light-current (LI) curves of multi-section un-doped SLED (Zia393) under pulsed conditions. The first section is 0.5 mm and the second section is 2.5 mm.

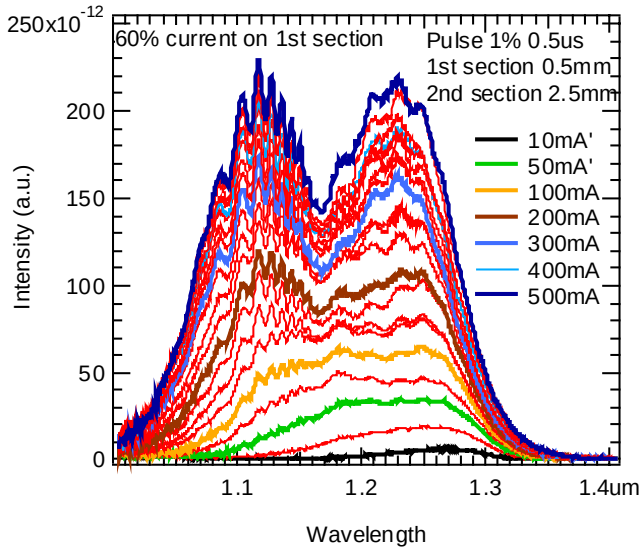

(a)

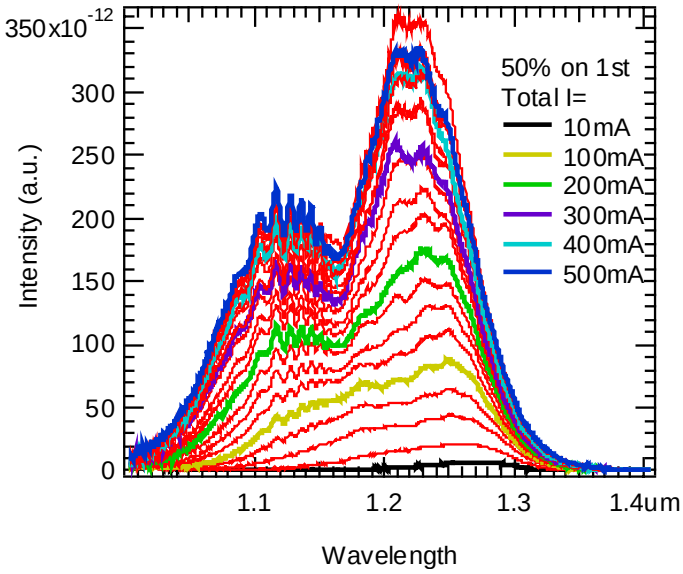

(b)

Figure 4-8 Spectra of a 3-section un-doped SLED (Zia393) under pulsed pumping. The first section is 0.5 mm, and the second section is 2.5 mm. (a) 60% of the total current applied on the 0.5-mm section. (b) 50% of the total current applied on the 0.5-mm section.

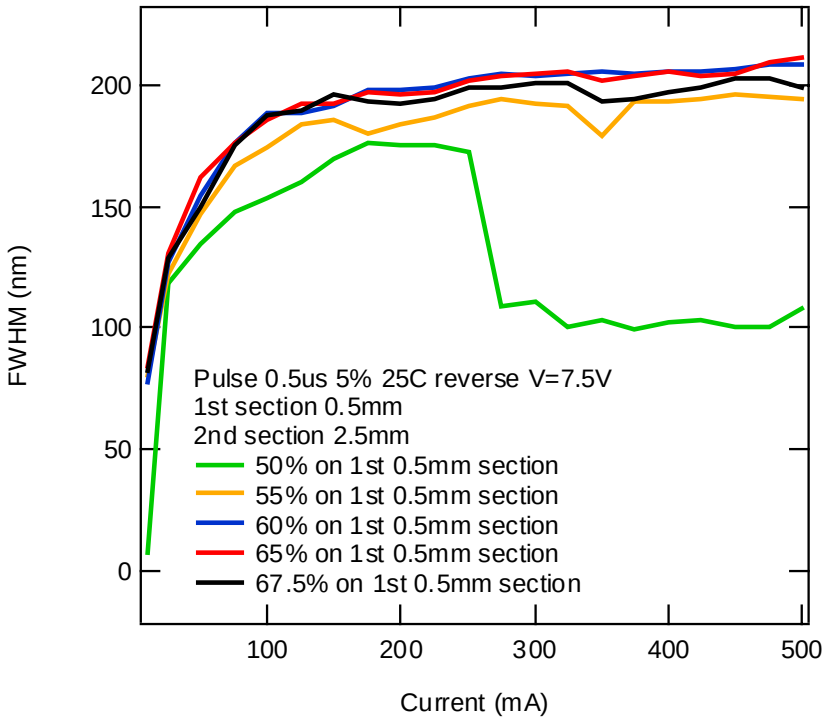

Figure 4-9 The FWHM of the 3-section undoped QD SLED (Zia393) versus total pump current in pulsed mode at 25°C. The first section is 0.5 mm and the second section is 2.5 mm. The inset shows the spectrum when the current applied on section A_1 is 300 mA.

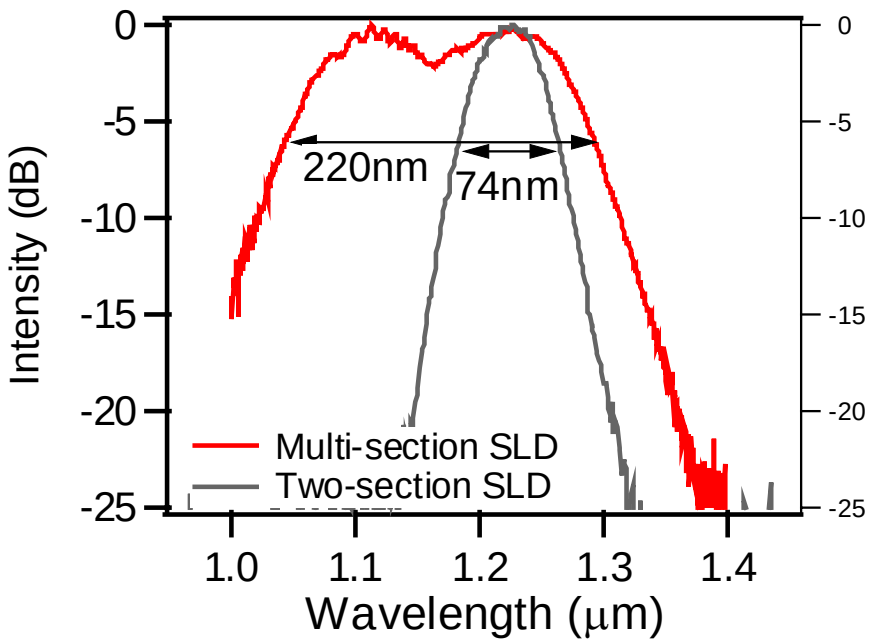

Figure 4-10 Spectra demonstrating the maximum bandwidth of a 3-section undoped SLED (L_1=0.5 mm and L_2=2.5 mm) and a reference 2-section SLED (L=3 mm). Total pump current was 500 mA for both SLEDs

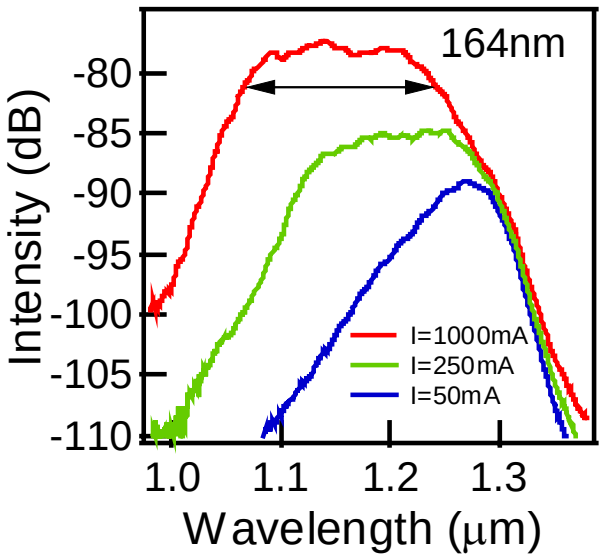

Figure 4-11. The spectra of 3-section SLEDs under pulse pump of 5% duty cycle and 0.5μs. The 1st section is 2 mm and the 2nd section is 4 mm. The current was divided as 61.5% on the 1st section and 38.5% on the 2nd section.

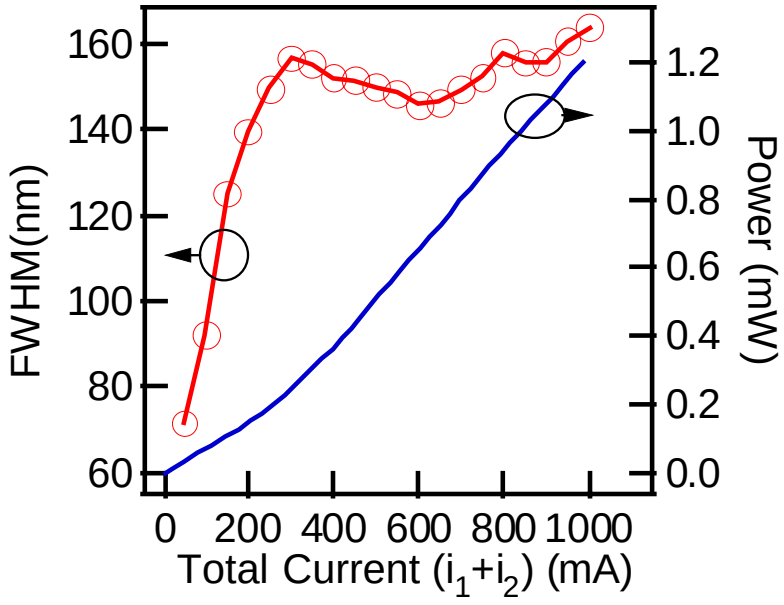

Figure 4-12. L-I curve and FWHM of an undoped QD SLED versus i_1+ i_2 in pulsed mode at 15°C. L_1=2 mm and L_2=4 mm.

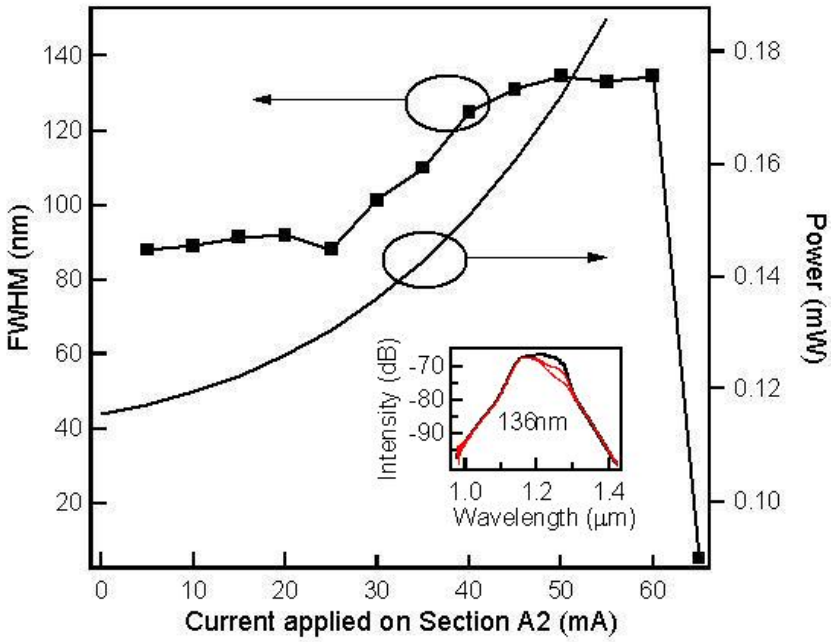

Figure 4-13. L-I curve and FWHM of the undoped QD SLED versus current i_2 in CW mode at 5°C. L_1=2 mm and i_1=400 mA, L_2=4 mm. The inset shows the spectra for i_2=57 mA.

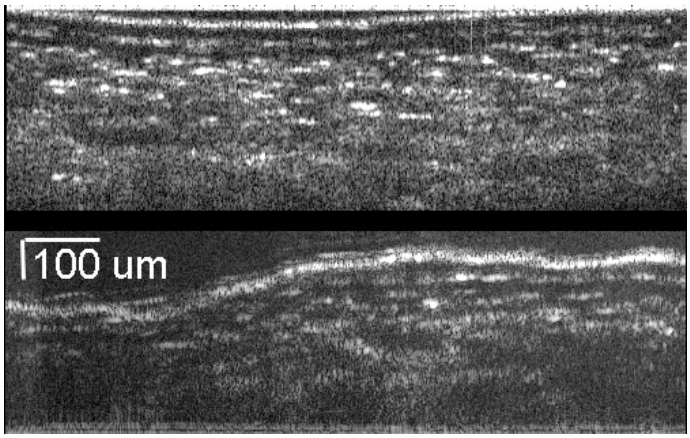

Figure 4-14. OCT image of onion skin with the multi-section SLED as the optical source

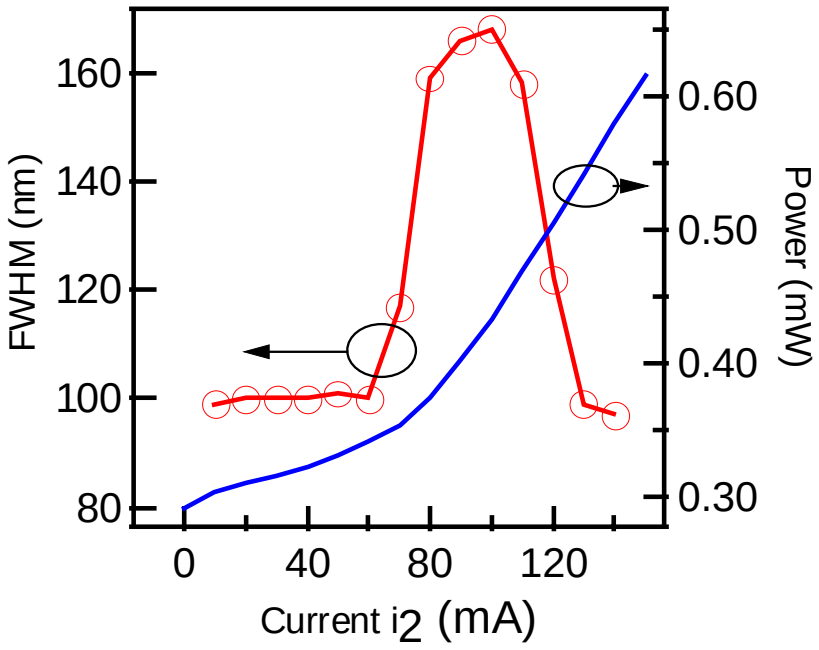

Figure 4-15. L-I curve and FWHM of the p-doped QD SLED versus current i_2 in CW mode at 10°C. L_1=1.5 mm and i_1=700 mA, L_2=5 mm.

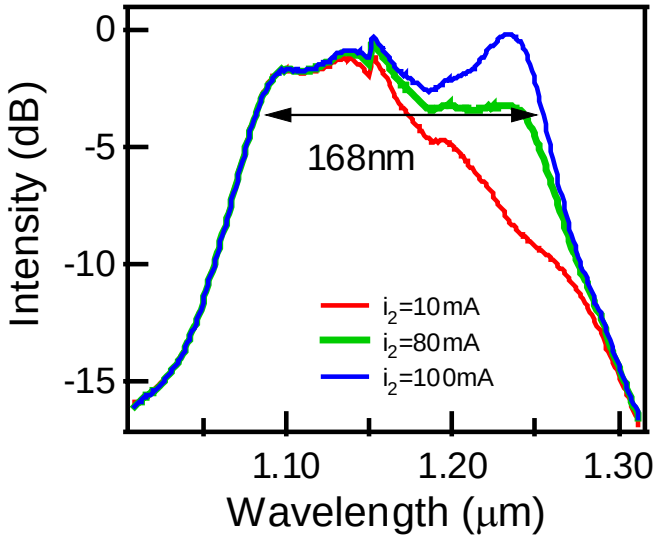

Figure 4-16. Spectra of the p-doped QD SLED under CW pumping at 10°C. L_1=1.5 mm, i_1=700 mA, L_2=5 mm and i_2=10, 80, 100 mA.

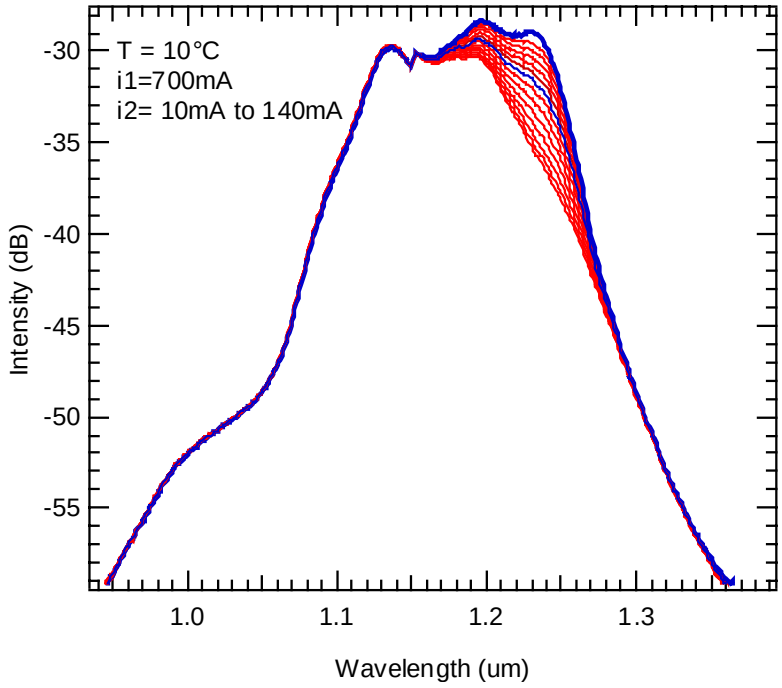

Figure 4-17 Spectra of a p-doped SLED optimized for high output power. L_1 is 2 mm and L_2 is 5 mm. i_1 = 700 mA and i_2 is scanned from 10 mA to140 mA.

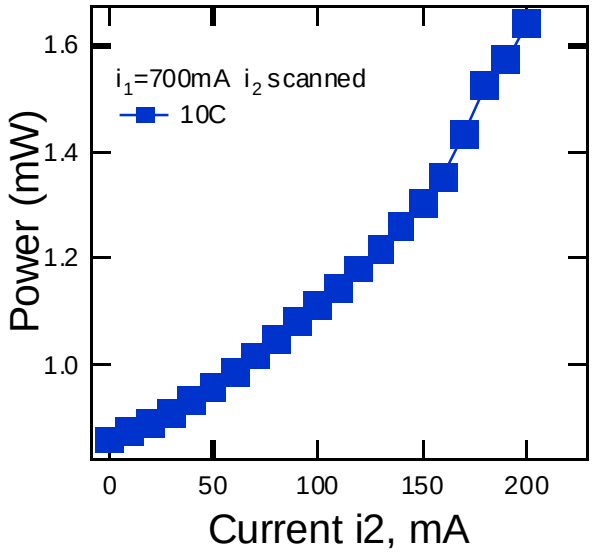

Figure 4-18. LI curve of p-doped SLED optimized for high output power. L_1 is 2 mm and L_2 is 5 mm. i_1 = 700 mA and i_2 is scanned.

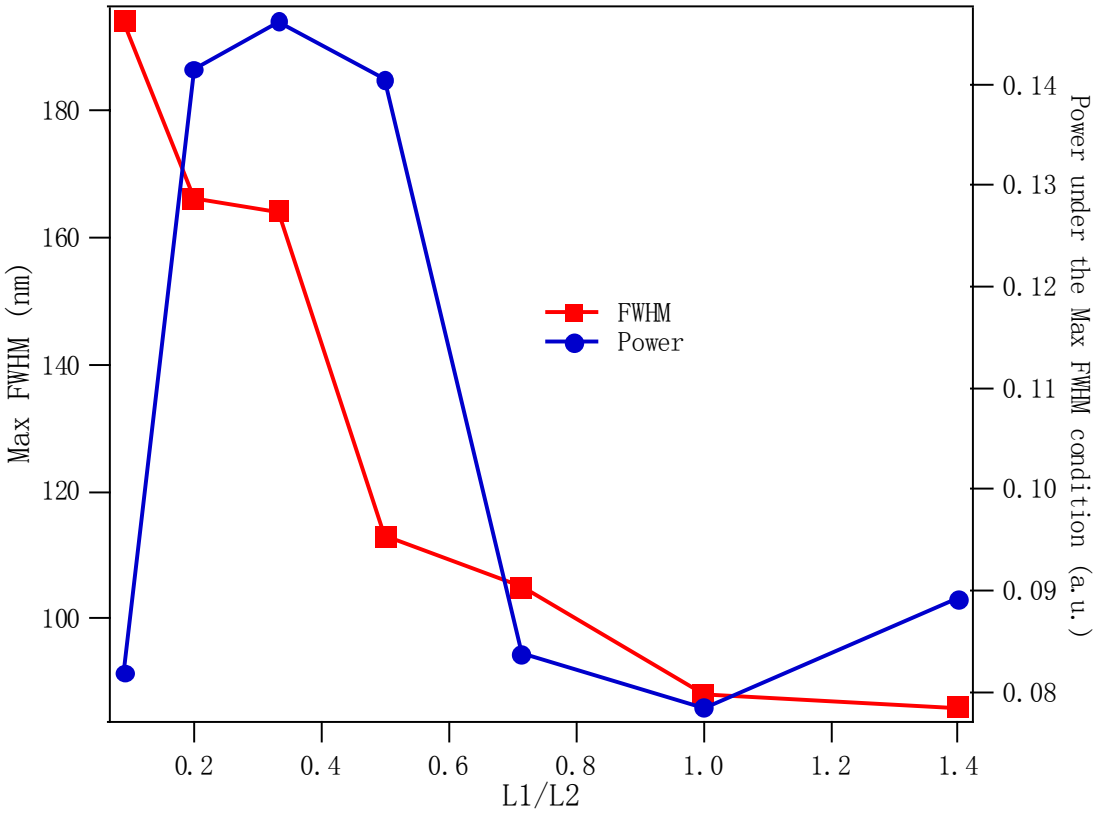

Figure 4-19. The evolution of the bandwidth (FWHM) and corresponding output power versus the ratio of the lengths of the gain sections, L1/L2.

4.5 References For Chapter 4

1 Huang, D., Swanson, E. A., Lin, C. P., Schuman, J. S., Stinson, W. G., Chang, W., Hee, M. R., Flotte, T., Gregory, K., Puliafito, C. A., And Fujimoto, J. G., "Optical Coherence Tomography," *Science*, Vol. 254, No. 5035, Pp. 1178-1181, 1991.

2 Boppart, S. A., "Optical coherence tomography - Principles applications and advances," *Minerva Biotecnologica*, vol. 16, no. 4, pp. 211-237, 2004.

3 Wolfgang Drexler, "Ultrahigh-resolution optical coherence tomography", Journal of Biomedical Optics 9(1), 47–74 (January/February 2004)

4 Koozekanani, D., Boyer, K. L., and Roberts, C., "Tracking the optic nervehead in OCT video using dual eigenspaces and an adaptive vascular distribution model," *IEEE Transactions On Medical Imaging*, vol. 22, no. 12, pp. 1519-1536, 2003.

5 Zuccaro, G., Gladkova, N., Vargo, J., Feldchtein, F., Zagaynova, E., Conwell, D., Falk, G., Goldblum, J., Dumot, J., Ponsky, J., Gelikonov, G., Davros, B., Donchenko, E., and Richter, J., "Optical coherence tomography of the esophagus and proximal stomach in health and disease," *American Journal of Gastroenterology*, vol. 96, no. 9, pp. 2633-2639, 2001.

6 Adler, D. S., Ko, T. H., Konorev, A. K., Mamedov, D. S., Prokhorov, V. V., Fujimoto, J. J., and Yakubovich, S. D., "Broadband light source based on quantum-well superluminescent diodes for high-resolution optical coherence tomography," Quantum Electronics, vol. 34, no. 10, pp. 915-918, 2004.

7 Drexler, W., Sattmarin, H., Hermann, B., Ko, T. H., Stur, M., Unterhuber, A., Scholda, C., Findl, O., Wirtitsch, M., Fujimoto, J. G., and Fercher, A. F., "Enhanced visualization of macular pathology with the use of ultrahigh-resolution optical coherence tomography," *Archives of Ophthalmology*, vol. 121, no. 5, pp. 695-706, 2003.

8 Bizheva, K., Povazay, B., Hermann, B., Sattmann, H., Drexler, W., Mei, M., Holzwarth, R., Hoelzenbein, T., Wacheck, V., and Pehamberger, H., "Compact, broad-bandwidth fiber laser for sub-2-μm axial resolution optical coherence tomography in the 1300-nm wavelength region," *Optics Letters*, vol. 28, no. 9, pp. 707-709, 2003.

9 Ko, T. H., Adler, D. C., Fujimoto, J. G., Mamedov, D., Prokhorov, V., Shidlovski, V., and Yakubovich, S., "Ultrahigh resolution optical coherence tomography imaging with a broadband superluminescent diode light source," *Optics Express*, vol. 12, no. 10, pp. 2112-2119, 2004.

10 Ong, T. K., Yin, M., Yu, Z., Chan, Y. C., and Lam, Y. L., "High performance quantum well intermixed superluminescent diodes," Measurement Science & Technology, vol. 15, no. 8, pp. 1591-1595, 2004.

11 Du, G. T., Xu, C. D., Liu, Y., Zhao, Y. S., and Wang, H. S., "High-power integrated superluminescent light source," IEEE Journal of Quantum Electronics, vol. 39, no. 1, pp. 149-153, 2003.

12 Lin, C. F. and Lee, B. L., "Extremely broadband AlGaAs/GaAs superluminescent diodes," Applied Physics Letters, vol. 71, no. 12, pp. 1598-1600, 1997.

13 H. S. Gingrich, D. R. Chumney, S. Z. Sun, S. D. Hersee, L. F. Lester, and S. R. J. Brueck, "Broadly tunable external cavity laser diodes with staggered thickness multiple quantum wells," *IEEE Photonics Technology Letters*, vol. 9, no. 2, pp. 155-157, 1997.

14 Zhang, Z. Y., Wang, Z. G., Xu, B., Jin, P., Sun, Z. Z., and Liu, F. Q., "High-performance quantum-dot superluminescent diodes," IEEE Photonics Technology Letters, vol. 16, no. 1, pp. 27-29, 2004.

15 Heo, D. C., Song, J. D., Choi, W. J., Lee, J. I., Jung, J. C., and Han, I. K., "High power broadband InGaAs/GaAs quantum dot superluminescent diodes," Electronics Letters, vol. 39, no. 11, pp. 863-865, 2003.

16 Heo, D. C., Dong, S. J., Choi, W. J., Lee, J. I., Jeong, J. C., and Han, I. K., "Characteristics of superluminescent diodes utilizing In0.5Ga0.5As quantum dots," *Japanese Journal of Applied Physics Part 1-Regular Papers Short Notes & Review Papers*, vol. 42, no. 8, pp. 5133-5134, 2003.

17 Han, I. K., Bae, H. C., Cho, W. J., Lee, J. I., Park, H. L., Kim, T. G., and Lee, J. I., "Study of chirped quantum dot superluminescent diodes," *Japanese Journal of Applied Physics Part 1-Regular Papers Brief Communications & Review Papers*, vol. 44, no. 7B, pp. 5692-5695, 2005.

18 Li, L. H., Rossetti, M., Fiore, A., Occhi, L., and Velez, C., "Wide emission spectrum from superluminescent diodes with chirped quantum dot multilayers," Electronics Letters, vol. 41, no. 1, pp. 41-43, 2005.

19 Rossetti, M., Markus, A., Fiore, A., Occhi, L., and Velez, C., "Quantum dot superluminescent diodes emitting at 1.3 mu m," *IEEE Photonics Technology Letters*, vol. 17, no. 3, pp. 540-542, 2005.

20 S. K. Ray, K. M. Groom, H. Y. Liu, M. Hopkinson, and R. A. Hogg, "Broad-band superluminescent light emitting diodes incorporating quantum dots in compositionally modulated quantum wells," *Japanese Journal of Applied Physics Part 1-Regular Papers Brief Communications & Review Papers*, vol. 45, no. 4A, pp. 2542-2545, 2006.

21 S. K. Ray, K. M. Groom, M. D. Beattie, H. Y. Liu, M. Hopkinson, and R. A. Hogg, "Broad-band superluminescent light-emitting diodes incorporating quantum dots in compositionally modulated quantum wells," *IEEE Photonics Technology Letters*, vol. 18, no. 1-4, pp. 58-60, 2006.

22 Stintz, A., Liu, G. T., Li, H., Lester, L. F., and Malloy, K. J., "Low-threshold current density 1.3-mu m InAs quantum-dot lasers with the dots-in-a-well (DWELL) structure," IEEE Photonics Technology Letters, vol. 12, no. 6, pp. 591-593, 2000.

23 Joseph T.Verdeyen, Laser Electronics 1995.

Chapter 5 Summary and Future Work.

With the highly flexible, reconfigurable multi-section approach, we studied QD devices from both operation characterizations and device structure designs.

We improved the multi-section gain and absorption measurement method by subtracting the background signals and for the first time, obtained low noise, accurate gain and absorption spectra under real CW working conditions. With the improved multi-section method and MLL testing, all the MLL characteristics and quantum dot parameters were measured with a same device. The relationship between quantum dot MLL performance and quantum dot parameters is studied. We demonstrate novel designs of QD MLLs and SLEDs with multi-section devices. The AGP multi-section MLL significantly increases the peak pulsed power (> 45%) and improves the pulse width (>35%) of the device. With the ability to change absorber position in the optical cavity at will, harmonic mode-locking from 7.2 GHz to 51 GHz is achieved. The ridge-waveguide multi-section QD SLED allows independent adjustment of the power and the spectral bandwidth relative to the ground state (GS) and the excited state (ES) of the QD and demonstrates simultaneous ultra-wide 3-dB bandwidth (> 150 nm) and an output power greater than 1 mW with a uniform multi-stack QD structure.

The future works of the QD MLLs mainly focus on the peak power improving and repetition rate increasing. With optimized AGP or GAG multi-section structures, an output peak power over 2W is expected with 1^{st} or high order harmonic mode-locking. An idea of the high frequency MLL is a GAGAGAG asymmetric multi-section configuration as shown in the Figure 5-1. The waveguide length is 8mm. The 4 gain section lengths will be 2^{nd}, 3^{rd}, 5^{th} and 7^{th} harmonic mode-locking section lengths

individually. Hence, there will be only the 210^{th} harmonic mode-locking mode has CPM effect in the cavity corresponding to a repetition rate of 1 THz.

For improving QD SLED, the multi-section QD SLEDs based on the chirped QD materials is studied for simultaneous ultra-wide bandwidth (>150nm) and high power (>3mW).

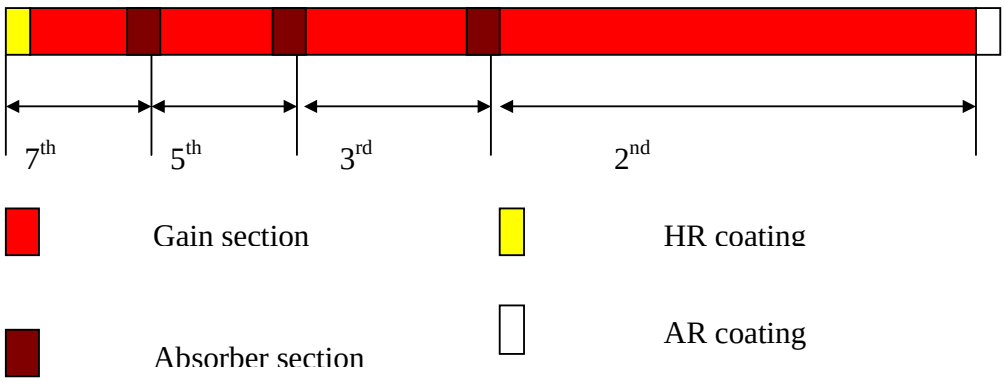

Figure 5-1 The GAGAGAG asymmetric multi-section 1THz configuration MLL design.

Appendix: FR-103XL Autocorrelator Instruction

The model FR-103XL rapid scanning autocorrelator is a high resolution instrument for continuous monitoring and display of femtosecond and picosecond laser pulses. While its unprecedented resolution makes it ideal for fsec pulses from modelocked lasers with high peak power, the instrument's high sensitivity renders it perfectly suited also for long pulses with low power. [1]

The FR-103XL utilizes the SHG method of the 1st kind in the conventional Michelson Interferometer setup of pulse width measurement [2]. In the standard configuration, noncollinear beams lead to the background-free autocorrelation measurement. Repetitive linear delay generation in one arm of the Michelson arrangement is introduced by a pair of parallel (//) mirrors centered about a rotating axis. In the geometry of Figure A-1, the rotation of the // mirror assembly leads to an increase (or decrease) of path length for a traversing beam. Thus, the transmitted pulse train is delayed (or advanced) about the reference (zero delay) position. This delay varies with time as a function of the shaft's rotation. For small angular changes, the delay as a function of time is linear and given by [3]

$$T = \left(\frac{4\pi f D}{c} \right) t$$

where D is the distance between the // mirrors, f is the frequency of rotation, and c is the speed of light.

Rotation of the // mirror assembly leads to a repetitive generation of linear delay which, used in the described SHG configuration, provides a continuous display of the autocorrelation function of the pulses on a conventional high impedance oscilloscope synchronized to this rotation. The total scan range is given by [2]

$$T_t = \frac{\sqrt{2}d}{c}$$

where d is the length of the scanning mirror.

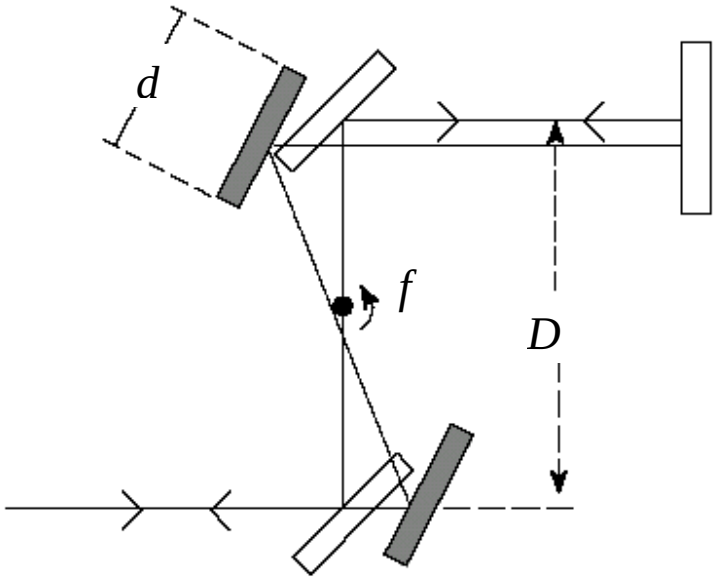

Figure A-1 Rotating Parallel (//) Mirrors in the autocorrelator

A figure of nonlinearity over the full scan range is [3]

$$NL = \frac{d}{4D}$$

In the standard configuration of the FR-103XL, the scan mirror has a size of d = 1.70" and the mirrors are separated by a distance of D = 3". The rotation frequency is f = 10 Hz. (f = 5Hz and 2.5 Hz is also selectable by a slide switch near the // mirrors.) Hence, the following numerical values follow

T/t = 31 psec/msec [15.5ps/ms for 5Hz, and 7.75ps/ms for 2.5Hz]

T_t = 200 psec

NL = 7%/100 psec

The specifications of the model FR-103XL rapid scanning autocorrelator is shown in the Figure A-2.

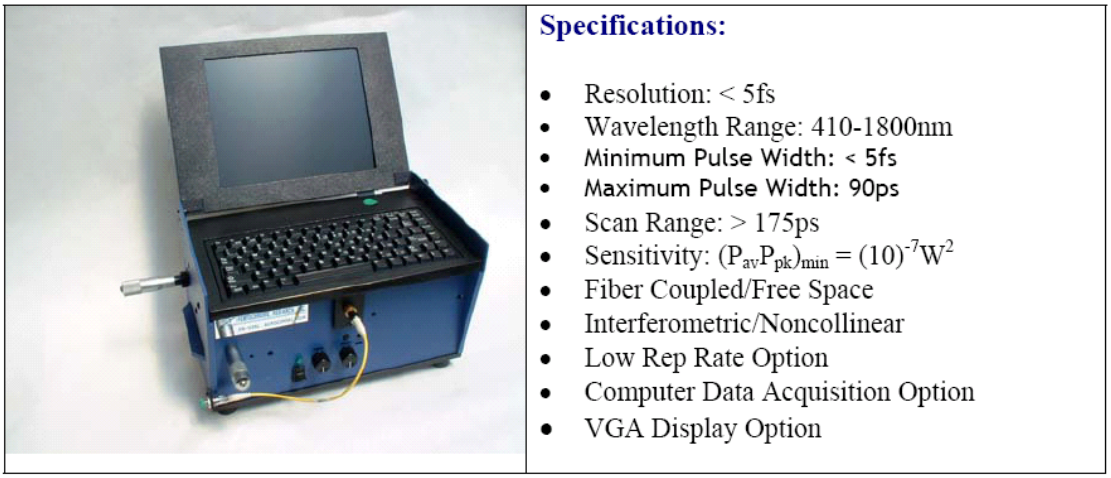

Figure A-2 specifications of the model FR-103XL rapid scanning autocorrelator

Reference for Appendex

1 FR-103XL Autocorrelator Instruction Manual, Femtochrome Research, Inc.

2 E.P. Ippen and C.V. Shank, "Ultrashort Light Pulses," S.L. Shapiro ed., New York: Springer-Verlag, 1977

3 Z.A. Yasa and N.M. Amer, *Optics Commun*., V36, pp 406, 1981